DYNAMIC FREQUENCY CONTROL IN DIESEL-HYBRID AUTONOMOUS POWER SYSTEMS USING VIRTUAL SYNCHRONOUS MACHINES

Miguel A. Torres L.

A Thesis

in The Department

of

Electrical and Computer Engineering

Presented in Partial Fulfillment of the Requirements
for the Degree of Doctor of Philosophy at
Concordia University
Montréal, Québec, Canada.

May, 2013.

CONCORDIA UNIVERSITY

SCHOOL OF GRADUATE STUDIES

This is to certify that the thesis prepared

By: **Miguel Torres-Lepez**

Entitled: **Dynamic Frequency Control in Diesel-Hybrid Autonomous Power Systems Using Virtual Synchronous Machines**

and submitted in partial fulfillment of the requirements for the degree of

DOCTOR OF PHILOSOPHY (Electrical and Computer Engineering)

complies with the regulations of the University and meets the accepted standards with respect to originality and quality.

Signed by the final examining committee:

_____ Chair
Dr. R. Sedaghati

_____ External Examiner
Dr. E. F. El-Saadany

_____ External to Program
Dr. M. Elektorowicz

_____ Examiner
Dr. A.G. Aghdam

_____ Examiner
Dr. S. Williamson

_____ Thesis Supervisor
Dr. L.A.C. Lopes

Approved by _____
Dr. J.X. Zhang, Graduate Program Director

May 27, 2013

_____
Dr. Robin Drew, Dean
Faculty of Engineering & Computer Science

Abstract

Dynamic Frequency Control in Diesel-Hybrid Autonomous Power Systems using Virtual Synchronous Machines

Miguel A. Torres L., Ph.D.
Concordia University, 2013.

In diesel-hybrid autonomous power systems, a reduced number of diesel generators supply the power to the load and control the frequency of the system in isolation from the utility grid. In these type of systems, frequency variations of consequence are more likely to occur than in large interconnected power grids, since they feature a relatively small generation capacity and rapid changes in power demand. If generators are not able to maintain frequency within prescribed operational limits during a transient, the assistance of other components is required in order to avoid major disruptions in the power system. In this thesis the use of a virtual synchronous machine (VSM) to support dynamic frequency control in a diesel-hybrid autonomous power system was investigated. The proposed VSM consisted in the control of the grid-interface converter of an energy storage system in order to emulate the inertial response and the damping power of a synchronous generator. Furthermore, the damping function of the proposed VSM used an estimated value of the stabilization frequency of the grid, which allowed it to provide proper damping power when the system operated in frequency droop mode. Theoretical and experimental results showed a satisfactory performance of the proposed VSM, which effectively reduced the frequency nadir in 34 %, on average, for different values of the droop factor of the grid-forming genset. Finally,

self-tuning algorithms were designed to find optimal parameters for the VSM in order to minimize the amplitude and rate of change of the frequency variations, and the power flow through the energy storage. Simulations results showed that the self-tuning VSM achieved a performance similar to the constant parameters VSM, while reducing the power flow through the energy storage in up to 58 %.

ACKNOWLEDGEMENTS

TABLE OF CONTENTS

TABLE OF CONTENTS

TABLE OF CONTENTS

TABLE OF CONTENTS

LIST OF FIGURES

LIST OF TABLES

LIST OF ACRONYMS

ac   :   alternating current.

APS   :   autonomous power system.

AVR   :   automatic voltage regulator.

CP-VSM   :   constant parameters VSM.

dc   :   direct current.

DG   :   diesel generator.

DSP   :   digital signal processor.

ES   :   energy storage.

ESS   :   energy storage system.

Genset   :   diesel generator set.

GUI   :   graphic user-interface.

IG   :   induction generator.

ISO   :   international organization for standardization.

JTAG   :   joint test action group (communication interface).

LAN   :   local area network.

NA   :   not applicable.

PC   :   personal computer.

PEI   :   power electronics interface.

PI   :   proportional-integral.

PLL   :   phase-locked loop.

PV   :   photovoltaic.

PWM	:	pulse-width modulation.
RE	:	renewable energy.
rms	:	root mean square.
roc	:	rate of change.
SC	:	supercapacitor.
SG	:	synchronous generator.
SM	:	synchronous machine.
SPWM	:	sinusoidal pulse-width modulation.
ST-VSM	:	self-tuning VSM.
VSC	:	voltage source converter.
VSG	:	virtual synchronous generator.
VSM	:	virtual synchronous machine.
WG	:	wind generator.
WT	:	wind turbine.
ZC	:	zero crossing.

LIST OF MAIN SYMBOLS

GENERAL

SCALARS

t :   continuous time.

kT :   discrete time, with T the sampling time and $k = 0, 1, 2\ldots$.

s :   Laplace variable.

$x(t), x$:   variable that represent the instantaneous value of a quantity.

x_o :   value of x at the operating point.

$x(k)$:   discrete time representation of x.

$x(s)$:   Laplace representation of x.

$h(s)$:   transfer function.

ζ :   damping ratio of a second order linear system.

ω_n :   natural frequency of oscillation of a second order linear system.

$\|\mathbf{x}\|$:   Euclidean norm of vector $\mathbf{x}$.

VECTORS

$\mathbf{x}^\mathrm{abc}$:   column vector $\left[x^\mathrm{a}\, x^\mathrm{b}\, x^\mathrm{c}\right]^\mathrm{T}$ of three-phase variables in abc reference frame.

$\mathbf{x}^\mathrm{dq}$:   column vector $\left[x^\mathrm{d}\, x^\mathrm{q}\right]^\mathrm{T}$ of three-phase variables in dq reference frame.

$\mathbf{x}$:   column vector of state variables $[x_1\, x_2 \ldots x_n]^\mathrm{T}$.

$\mathbf{u}$:   column vector of input variables $[u_1\, u_2 \ldots u_m]^\mathrm{T}$.

$\mathbf{y}$:   column vector of output variables $\left[y_1\, y_2 \ldots y_p\right]^\mathrm{T}$..

ψ :   column vector of flux linkages.

$\mathbf{i}$:   column vector of currents.

MATRICES

$\mathbf{T}_{\text{abc/dq}}$: transformation matrix from abc to dq reference frame.

$\mathbf{T}_{\text{dq/abc}}$: transformation matrix from dq to abc reference frame.

$\mathbf{I}_n$: identity matrix, dimension n.

$\mathbf{A}$: matrix of parameters.

$\mathbf{B}$: matrix of parameters.

$\mathbf{C}$: matrix of parameters.

$\mathbf{D}$: matrix of parameters.

$\mathbf{L}$: matrix of inductances.

$\mathbf{R}$: matrix of resistances.

$\mathbf{W}$: matrix of coupling between state variables.

$\mathbf{N}$: matrix of coupling between input variables.

$\mathbf{H}(s)$: matrix of transfer functions.

AUTONOMOUS POWER SYSTEM

$\mathbf{v}_{\text{g}}^{\text{abc}}$: ac bus phase voltages.

f : frequency of ac bus phase voltages.

f_{p} : peak frequency after power disturbance.

t_{p} : time of peak frequency.

roc_f : initial rate of change of frequency after power disturbance.

f^* : stabilization frequency.

p_{Load} : active power consumed by the load.

DIESEL GENERATOR

p_{DG} : output active power.

J_{eq} : moment of inertia of equivalent single-mass model.

k_{feq} : rotational losses coefficient of equivalent single-mass model.

ω_{eq} : rotational speed of equivalent single-mass model.

J_a : additional inertia for analysis of transient response.

D_a : additional damping for analysis of transient response.

DIESEL ENGINE

τ_m : output torque.

τ_{max} : maximum output torque.

p_m : output power.

ω_{en} : rotational speed.

Ω_{en} : nominal rotational speed.

J_{en} : moment of inertia (engine plus flywheel).

k_{fen} : rotational losses coefficient.

k_e : engine gain.

t_d : internal combustion delay.

t_e : fuel injection time constant.

SYNCHRONOUS GENERATOR

τ_e : electromagnetic torque.

ω_{ge} : rotational speed.

θ_{ge} :   electrical phase of the rotor.

J_{ge} :   moment of inertia.

k_{fge} :   rotational losses coefficient.

n_p :   number of magnetic poles.

n_{pp} :   number of pairs of magnetic poles.

$v_s^{d,q}$:   stator phase voltages.

v_t :   rms value of terminal voltage.

v_f :   field voltage (AVR rectifier output voltage).

$\psi_s^{d,q}$:   stator windings flux linkages.

ψ_f :   field winding flux linkage.

$\psi_k^{d,q}$:   damper windings flux linkages.

$i_s^{d,q}$:   stator currents.

i_f :   field current.

$i_k^{d,q}$:   damper circuits currents.

$L_{sl}^{d,q}$:   stator windings leakage inductances.

L_{fl} :   field leakage inductance.

$L_{kl}^{d,q}$:   damper windings leakage inductances.

$L_m^{d,q}$:   mutual inductances.

R_s :   stator resistance.

R_f :   field resistance.

$R_k^{d,q}$:   damper circuits resistances.

LIST OF MAIN SYMBOLS

COUPLING SHAFT

τ_s :   transmitted torque, $\tau_s = \tau_{ss} + \tau_{fs}$.

τ_{fs} :   transmitted torque through damper element.

τ_{ss} :   transmitted torque through spring element.

k_{fs} :   torsional damping coefficient.

k_{ss} :   torsional stiffness coefficient.

ω_{res} :   resonance frequency.

AUTOMATIC VOLTAGE REGULATOR

k_{pv} :   proportional gain.

k_{iv} :   integral gain.

z_v :   integrator state.

y_v :   non-saturated output.

u_v :   saturated output.

v_{tref} :   reference value for the rms output voltage, v_t.

t_{rec} :   rectifier time constant.

k_{rec} :   rectifier gain.

SPEED GOVERNOR

$k_{p\omega}$:   proportional gain.

$k_{i\omega}$:   integral gain.

k_{dr} :   droop gain.

z_ω :   integrator state.

y_ω : non-saturated output.

u_ω : saturated output.

$\omega_{\text{en ref}}$: reference value for the engine speed, ω_{en}.

m_{dr} : speed droop factor.

ENERGY STORAGE SYSTEM

p_{ESS} : output active power.

q_{ESS} : output reactive power.

$p_{\text{ESS ref}}$: active power reference.

$q_{\text{ESS ref}}$: reactive power reference.

$i_{\text{ESS}}^{\text{d,q}}$: output currents.

$i_{\text{ESS ref}}^{\text{d,q}}$: current references.

VOLTAGE SOURCE CONVERTER

v_{dc} : dc bus voltage.

$\mathbf{v}_{\text{c}}^{\text{abc}}$: PWM phase voltages.

R : ac filter resistance.

L : ac filter inductance.

C : ac filter capacitance.

R_{dc} : dc filter resistance.

C_{dc} : dc filter capacitance.

$m^{\text{d,q}}$: modulation indexes.

$u^{\text{d,q}}$: new inputs for current loops after linearization.

$g^{d,q}$: new inputs for voltage loops after linearization.

$k_{pi}^{d,q}$: proportional gain of dq current controllers.

$k_{ii}^{d,q}$: integral gain of dq current controllers.

$k_{pv}^{d,q}$: proportional gain of dq voltage controllers.

$k_{iv}^{d,q}$: integral gain of dq voltage controllers.

f_c : SPWM carrier frequency.

VIRTUAL SYNCHRONOUS MACHINE

p_{VSM} : calculated output power.

k_r : conversion factor between frequency and rotational speed.

T_{sync} : synchronization and frequency calculation sampling time.

T_{ctr} : control sampling time.

INERTIAL RESPONSE

k_{vi} : virtual inertia.

T_f : filtered derivative time constant.

DAMPING POWER

k_{vd} : damping power coefficient.

$\tilde{e}$: estimated control error.

$\tilde{f}^*$: estimated stabilization frequency.

ϵ : frequency stabilization tolerance band.

$\tilde{k}_p$: governor proportional gain with uncertainty.

$\tilde{k}_{\mathrm{i}}$: governor integral gain with uncertainty.

$\widetilde{m}$: governor droop gain with uncertainty.

$\widetilde{\omega}_{\mathrm{ref}}$: governor reference speed with uncertainty.

Self-Tuning VSM

$K_{\mathrm{vi}}^{\min}$: minimum value of virtual inertia.

$K_{\mathrm{vi}}^{\max}$: maximum value of virtual inertia.

$K_{\mathrm{vd}}^{\min}$: minimum value of damping power coefficient.

$K_{\mathrm{vd}}^{\max}$: maximum value of damping power coefficient.

N_{vi} : number of elements of virtual inertia search vector.

N_{vd} : number of elements of damping coefficient search vector.

T_{p} : prediction algorithms sampling time.

c : cost function of the optimization problem.

γ_i : weight factors of the cost function.

$\mathcal{A}$: search area of the optimization problem.

Wind Generator

p_{WG} : output active power.

Wind Model

v_{w} : actual wind speed.

v_{wb} : base wind speed.

v_{wr} : ramp component.

v_{wg} : gust component.

v_{wt} : turbulence component.

WIND TURBINE

p_{wt} : output power.

τ_{wt} : output torque.

ω_{wt} : rotational speed (low speed shaft).

Ω_{ig} : nominal rotational speed.

J_{wt} : moment of inertia.

k_{fwt} : rotational losses coefficient.

R_{wt} : rotor radius.

η_{wt} : overall efficiency.

c_{p} : performance coefficient.

t_{wt} : blades filtering time constant.

v_{wf} : filtered wind speed.

COUPLING SHAFT

N_{gb} : gear box ratio.

τ_{swg} : transmitted torque.

k_{fs} : specific damping.

k_{ss} : torsional stiffness.

INDUCTION GENERATOR

τ_{ig} :   electromagnetic torque.

ω_{ig} :   rotational speed (high speed shaft).

Ω_{wt} :   nominal rotational speed.

J_{ig} :   moment of inertia.

k_{fig} :   rotational losses coefficient.

n_{ip} :   number of magnetic poles.

n_{ipp} :   number of pairs of magnetic poles.

$v_{is}^{d,q}$:   stator phase voltages.

$\psi_{is}^{d,q}$:   stator windings flux linkages.

$\psi_{ir}^{d,q}$:   rotor windings flux linkages.

$i_{is}^{d,q}$:   stator currents.

$i_{ir}^{d,q}$:   rotor currents.

L_{isl} :   stator windings leakage inductance.

L_{irl} :   rotor windings leakage inductance.

L_{im} :   mutual inductance.

R_{is} :   stator resistance.

R_{ir} :   rotor resistance.

CHAPTER 1

INTRODUCTION

1.1 GENERAL INTRODUCTION

In conventional power systems electrical energy is primarily generated by means of rotating machinery and supplied in the form of ac voltage, where the frequency of the ac voltage is associated to the rotational speed of generators. Any imbalance between load and generation originates a change in the kinetic energy of rotating generators and therefore a change in frequency. The characteristics of such frequency variations will depend mainly on the type of disturbance affecting the power system, the performance of the frequency control system, and physical properties of generators [1, 2]. For instance, large interconnected power grids can be considered as stiff systems where a large power disturbance must occur before the frequency will deviate to any significant level. This is not necessarily the case for small power systems that are isolated from the utility grid. In these autonomous power systems (APS), frequency variations of consequence are more likely to occur since they feature a relatively small generation capacity, rapid changes in power demand, and low inertia [3]. If generators are not able to maintain frequency within prescribed operational limits during a transient, the assistance of other components is required in order to avoid major disruptions in the power system. In this thesis the use of an energy storage system (ESS) to support dynamic frequency control is investigated.

1.2   BACKGROUND

A review of topics related to the frequency control in a diesel-hybrid autonomous power systems is presented in this section. The following aspects are covered:

i)   The basic structure of a diesel-hybrid APS.

ii)   Frequency control and stability in a diesel-hybrid APS.

iii)   The basic structure of the energy storage system.

1.2.1   Basic Structure of a Diesel-Hybrid APS

A diesel-hybrid autonomous power system can be simply defined as a small power system that generates electric power from diesel fuel and renewable energies (REs) in remote places where the utility grid is not feasible, with diesel generators being the primary source of energy due to its reliability and controllability. The characteristic of isolation from the utility, implies that the energy produced is confined to its structure, i.e., it is distributed, dissipated, transformed and stored within the system and there is no exchange of energy with other electrical systems. Regarding the size of the system, since no standard definition of a small APS has been found in the literature, the following will be used in the framework of this thesis: "...[A system] in the size range from $10\,\text{kW}$ to about $200\,\text{kW}$ of diesel power. Such a system will probably have only 1 or 2 diesel electric sets and...1 or 2 [wind generators]" [4]. From this definition, the reduced number of diesel generators implies that each unit supplies a substantial part of the total demand.
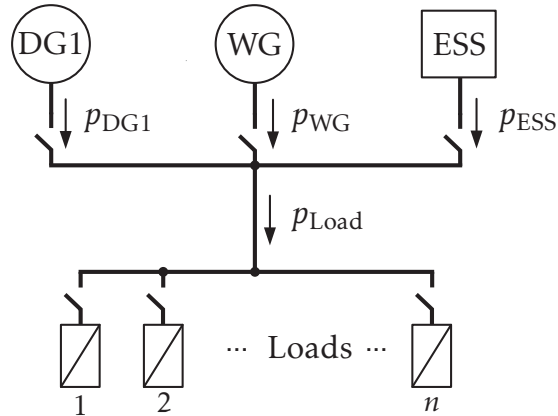
Figure 1.1: Block diagram of the autonomous power system.

Figure 1.1 depicts the block diagram of an APS that contains typical components of interest: a diesel generators (DG1), a wind generator (WG), an energy storage system (ESS), and several loads (Load1,2...n). A general description of each component is provided.

i)   **Load:**

a)   It is an abstraction of the electrical energy consumed by the end-users and/or processes.

b)   The total active power consumed by the load, p_{Load}, should be satisfied at all time.

ii)   **Diesel Generator (DG):**

a)   It is a rotating electrical generator, usually a synchronous generator, driven by a diesel engine.

b)   The use of the synchronous generator results in a strong coupling between the frequency of the output ac voltage and the rotating speed of the diesel engine [5].

c)   Its main function is to supply power to the loads, p_{DG1}, and

to maintain its output voltage at a constant amplitude and frequency.

iii)   **Wind Generator (WG):**

a)   It is a rotating electrical generator driven by a wind turbine.

b)   Depending on the topology, the electrical generator can be directly connected to the ac bus or indirectly connected by means of a static power converter.

c)   Depending on the topology, there is a certain degree of control over its output active power, p_{WG}.

iv)   **Energy Storage System (ESS):**

a)   It is a storage medium connected to the ac bus by means of static power converters.

b)   It can absorb (charging mode) or supply (discharging mode) active power.

c)   Its output active power, p_{ESS}, is considered a controlled variable.

1.2.2   Frequency Control and Stability

Frequency control schemes can be regarded as continuous and discontinuous controls as indicated in [2]. Discontinuous controls are not active all the time and they operate to support generators and protect the power system from a possible condition of instability. On the other hand, continuous controls, such as the ones describe next, are active all the time operating directly over the generator to control the frequency. An example of continuous control is primary frequency

control, which is defined in [6] as: "...an automatic adjustment of power by the local control and inertial response of the generators and loads within 30 seconds [after a disturbance]". A secondary control, if needed, would be in charge of adjusting the references on each generator to bring the system frequency to a desired value [1]. While primary control can be independently achieved by each generator, the secondary control would require a communication channel to coordinate the new references for each unit.

In a small APS primary frequency control is performed by the speed governors of diesel generators. Fig. 1.2 depicts the block diagram of a basic speed control which, in general terms, works as follows: an increase in the electrical load disturbs the equilibrium between the generated and consumed power and the diesel engine starts to decelerate while supplying electric energy, the change in the speed of the diesel engine is sensed by the governor, then the control error is processed and the corresponding control signal is sent to the fuel injection system, which modifies the fuel flow to the engine in order to increase the speed and reduce the error. The governor usually operates in two modes, isochronous and droop, which are described next.
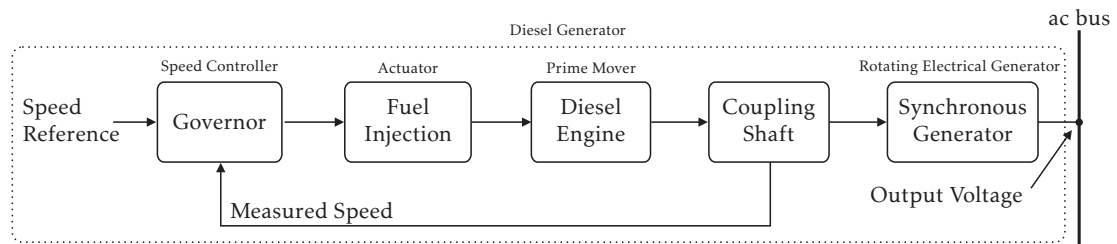
Figure 1.2: Diesel generator speed control.

A.   *Isochronous Control*

Isochronous control refers to the ability of the prime mover to return to the original reference speed after a load change (Fig. 1.3(b)). Therefore, an APS with at least one generator in isochronous control will operate at fixed steady-state frequency as long as the isochronous generator is capable of supplying the power demanded by the load. Fig. 1.3(a) shows the static relationship between power and frequency for a single generator in isochronous control mode.

One disadvantage of this strategy is that two or more parallel generators in isochronous mode require auxiliary control loops to coordinate load sharing, otherwise they tend to a condition of instability [7].

B.   *Permanent Droop Control*

Permanent droop control refers to the ability of the prime mover to return to a different speed after a load change. When the load increases, the generator will stabilize to a speed lower than the original as shown in Fig. 1.3(d). Conversely, when the load decreases, the generator will stabilize to a higher speed. Therefore, an APS with a single generator in permanent droop control will experience different operating frequencies as the load varies. Fig. 1.3(c) shows the static relationship between power and frequency for a single generator in droop mode.

In a system of multiple generators, permanent droop control allows stable operation by naturally sharing the load among them. Each generator supplies power according to its own droop function and the resulting frequency will be such that the combined load of all generators matches the total demand. Fig. 1.3(e)
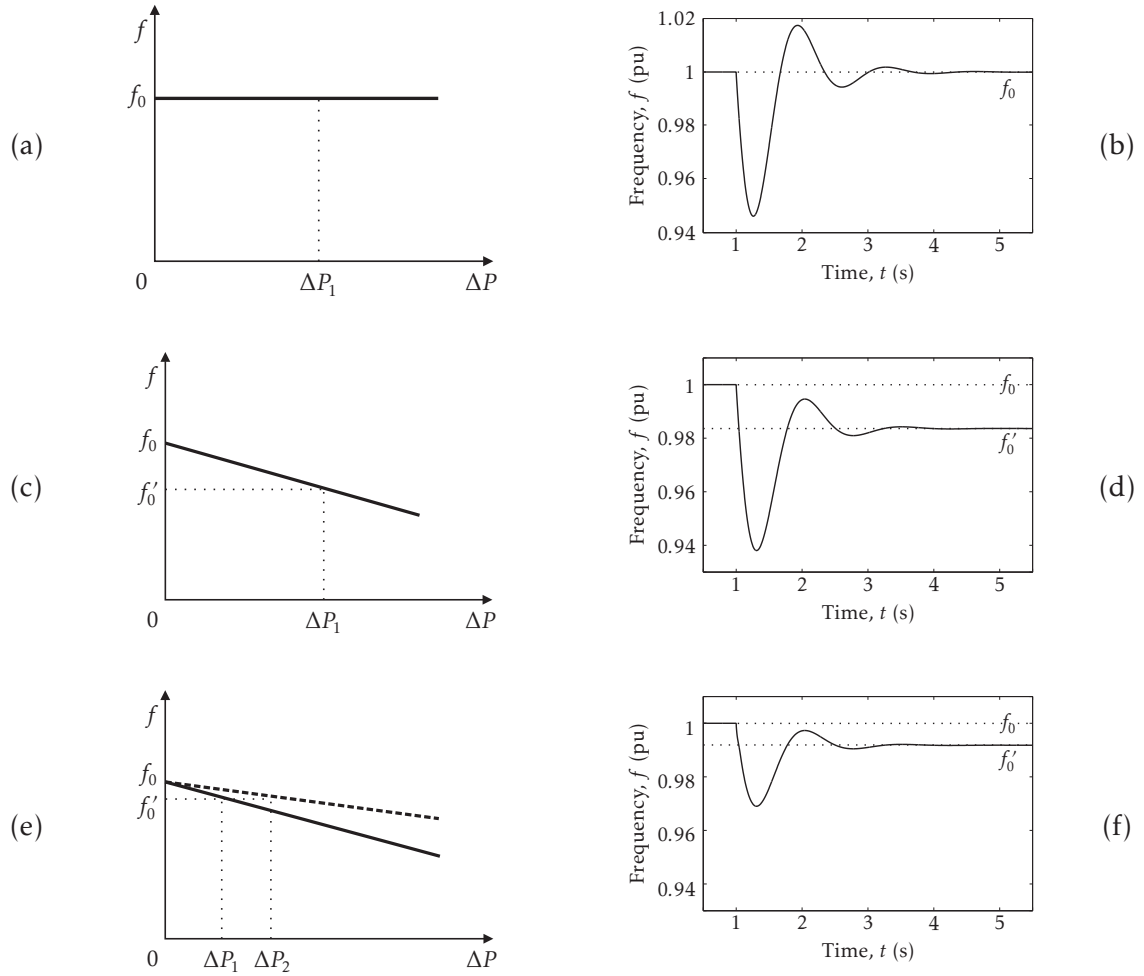
Figure 1.3: Frequency control strategies for prime movers in APSs.

This figure shows, for each case, the ΔP-f static curve (on the left) and a simulated waveform (on the right) to illustrate the frequency variation after a step-like load increase at $t = 1$ s. (a)-(b) Isochronous control. (c)-(d) Droop control. (e)-(f) Droop control for parallel generators.

shows the static relationships between power and frequency for two generators in droop control mode, with $\Delta P_1 + \Delta P_2$ being the total power demand and f_0' the resulting system frequency.

C.   *Frequency Stability*

In an APS that operates with primary frequency control, the frequency in steady-state is mainly determined by the mode in which the governor operates, i.e.

isochronous or droop control. Given a condition of steady frequency, the concept of frequency stability can be defined as "the ability of a power system to maintain steady frequency following a severe system upset resulting in a significant imbalance between generation and load" [8]. Besides, it can be noted that, in order to keep the system stable, the frequency variations during the transient condition should be maintained within prescribed operational limits, otherwise they might trigger protection/emergency relays that typically disconnect (unscheduled) portions of the load or generators, resulting in a worse power imbalance [9, 10]. Frequency stability is a problem of more concern in small APSs due to structural differences with large interconnected power systems and it usually represents an obstacle to integrate or increase the penetration of REs.

The transient behavior of the APS is determined by the characteristics of the system. For instance, assuming that the response of the speed control of Fig. 1.2 is not instantaneous, the speed deviation right after the power disturbance will be dominated by the inertial response of the genset. To illustrate this effect consider Fig. 1.4(a) where, starting from steady-state, the generated power equals the electrical load and the generator rotates at constant speed. Then, a sudden increase in the electrical load disturbs the power balance of the genset by demanding more power that what is being generated. Due to the delay Δt in the control loop the rotating masses of the genset naturally respond to this lack of generation by releasing kinetic energy, resulting in a decrease in the genset speed, where the initial rate of change is limited only by the inertia. It can be noted that a higher inertia $(J' > J)$ helps to reduce the rate of change of frequency, however, the overall re-
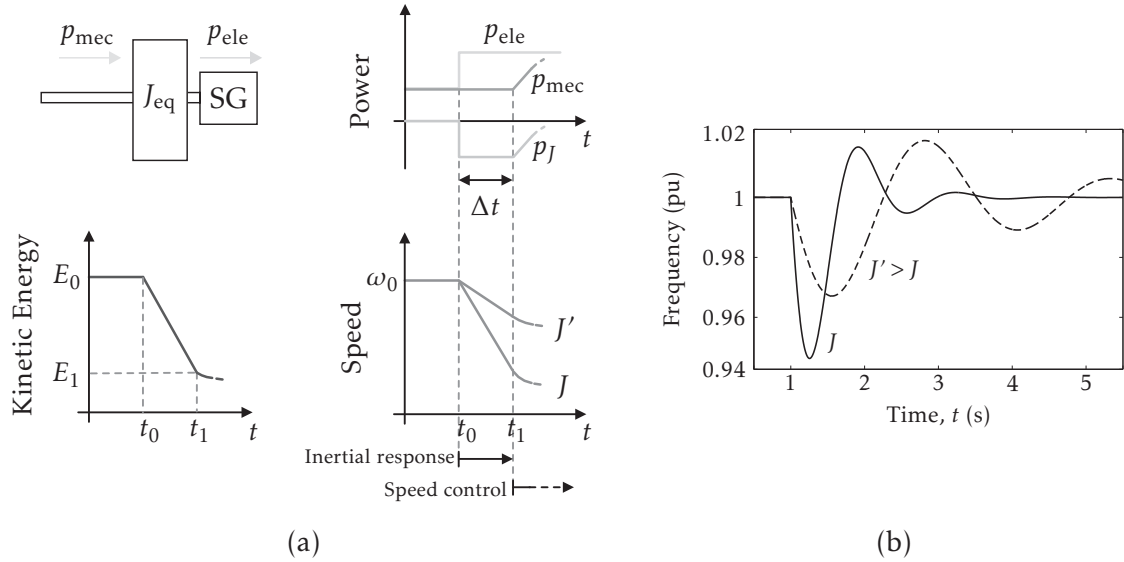
Figure 1.4: Frequency variation in a diesel generator.

(a) Inertial response. (b) Frequency transient.

sponse of the genset might be affected if only the inertia is changed and the rest of the system characteristics (e.g. controller parameters) remain the same. Fig. 1.4(b) shows that the frequency transient due to a step-like load increase becomes more oscillatory when only the inertia is increased.

If diesel generators are not able to maintain frequency within prescribed operational limits during the transient, the assistance of other components is required in order to avoid major disruptions in the power system. In this regard, load management strategies can be used to add or remove load from the system [11–14], helping to maintain the balance between power consumption and production at the cost of decreasing the power quality and reliability for system users. Also wind generators can be used (controlled) to support primary frequency control in the short and/or long-term [6, 15–17]. For instance, in the case of variable speed wind generators, short-term power compensation is typically performed by using

the rotating parts of the generator as energy storage. This approach is naturally limited by the amount of kinetic energy that can be stored or released from the rotating parts of the generator [18], however, additional capacity can be achieved by adding other type of energy storage to the system [19]. On the other hand, long-term compensation strategies are typically performed by operating the wind generator in a suboptimal condition (relative to the actual wind speed) that produces the necessary reserve for power compensation [20]. In this thesis only the use of an ESS to support dynamic frequency control is investigated.

1.2.3   The Energy Storage System

The ESS of interest consists of a dc storage medium—the energy storage—connected to the grid by means of a static power converter—the grid side converter. A block diagram of the topology is shown in Fig. 1.5.

A.   Energy Storage

The energy storage represents the appropriate medium to store and supply dc electrical energy according to the requirements of the application. Electrochemical batteries are one of the most common storage medium used in grid applications, with high energy density being its most notable characteristic [21]. Supercapacitors (SC), on the other hand, exhibit lower energy density than batteries, but present fast dynamics in supplying and absorbing large and frequent bursts of power [22, 23]. Since both technologies have complementary features in terms of energy and power capacities, hybrid energy storage has been proposed as
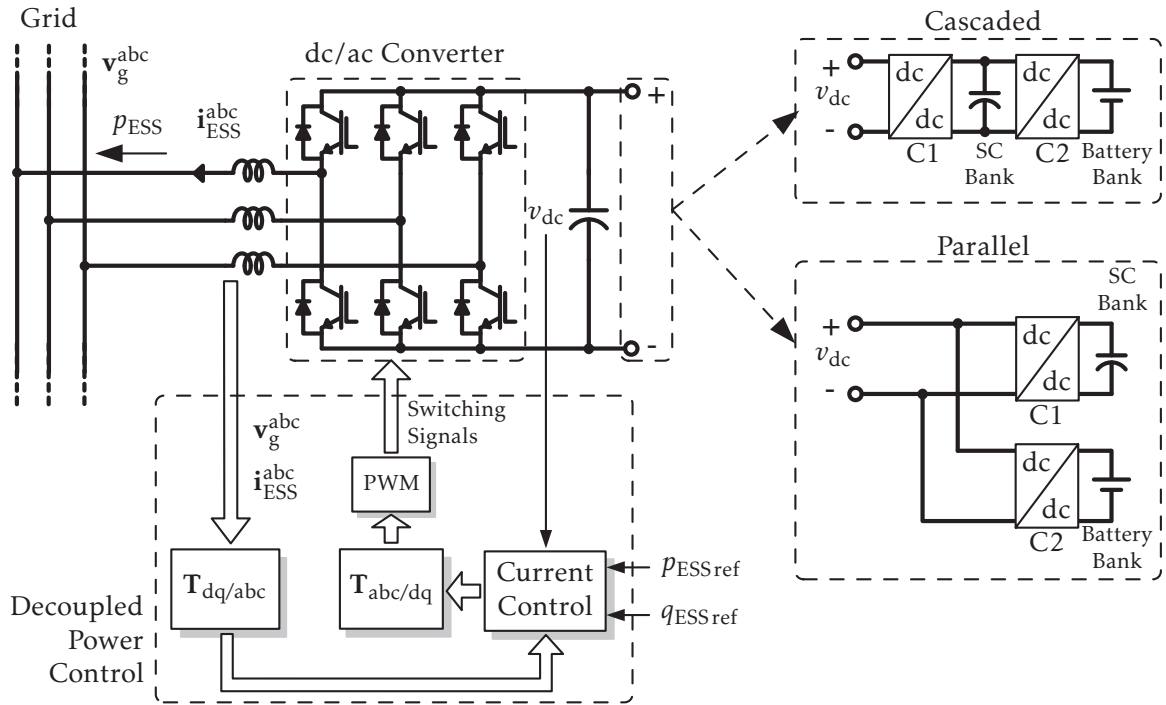
Figure 1.5: Energy storage system with hybrid storage.

a better solution for grid applications [24–29]. Fig. 1.5 shows two different configurations of hybrid storage: cascaded and parallel. The cascaded connection implies that the dc bus voltage must be controlled by the converter C1, while C2 is controlled to supply the low frequency components of the current demanded by the dc-ac converter, lowering the stress on the batteries. A disadvantage is that converter C1 has to support all the current flow and, if it fails, then C2 cannot be used. On the other hand, in the parallel connection both converters can work independently and their state-of-charge can be used to adjust their compensation efforts accordingly.

B.   *Grid Side Converter*

Voltage source converters (VSC) are one of the most widely used topologies in applications that require an interface to the grid such as adjustable speed drives, uninterruptible power supplies and flexible ac transmission systems [30–32]. The basic three-phase topology, shown in Fig. 1.5, consists of an array of six force-commutated switches, with a first order inductive filter on the ac side to minimize line current harmonics. On the dc side, it requires constant dc voltage and the mean value of the dc current determines if the converter operates as an inverter, where the active power flows from dc to ac side, or as a rectifier, where the active power flows from ac to dc side.

Voltage source converters present two characteristics which are suitable for the ESS: first, a VSC needs a dc voltage source type element, which is naturally provided by a battery, SC or battery-SC storage as well; second, a VSC can provide fast and accurate bidirectional line current control [33], which is needed for short-term active power compensation in dynamic frequency control support. It is important to note that the amplitude of the ac voltages of the VSC depends on the voltage level of the dc bus. Therefore, if the dc voltage is not adequate, the VSC might need a step-up transformer at the ac side to match the grid voltage level [34, 35].

1.3   LITERATURE REVIEW

The literature review is divided in two parts. First, a review of common techniques that use the ESS to support frequency control is presented, then the recent literature related to the virtual synchronous machine strategy is reviewed.

1.3.1   Frequency Control Using the ESS

A strategy that indirectly deals with dynamic frequency control is the smoothing of the output power of intermittent sources [36]. This technique entails generating a suitable reference for the ESS so that its output power cancels the high frequency components contained in the output power of the intermittent source. As a result, the fast variations of the grid frequency induced by the intermittent source are attenuated. One disadvantage of this technique is that it requires the measuring of the output power of the intermittent source, which restricts the location of the ESS or establishes the need for a communication link to transmit the measurements.

An approach that allows the autonomous control of distributed ESSs is the frequency droop control [37]. This strategy, inherited from the operation of conventional generators, relies on local measurements to control the output power of the ESS with no need for a communication link. However, for a proper application to ESSs, the "original" droop function needs to be modified to account for the charging of the storage (reverse power flow) and its limited energy capacity [38]. In its simplest form (permanent frequency droop) this technique is intended to support only frequency regulation, thus it does not cope with the problem of

dynamic frequency control. To address the latter a more sophisticated frequency droop control is needed, as the one presented in [39] which has an additional droop term that exists only during the transient (temporary frequency droop).

1.3.2 Virtual Synchronous Machine

A virtual synchronous machine (VSM) is a control strategy that was proposed to cope with stability issues in power systems with large fraction of distributed generators connected to the grid through power converters [40–46]. The main idea behind a VSM is to control the grid side converter of a distributed generator or ESS to emulate a synchronous generator (SG) or a desired characteristic of it. The complexity of the mathematical model used for the emulation will depend on the application [47]. Of particular interest in this thesis is the emulation of characteristics of the synchronous generator that affect the frequency of the system only during the transient, these are the inertial response and the damping power.

The emulation of inertial response typically entails the control of power that is inversely proportional to the first time-derivative of the grid frequency [17, 48]. Therefore, when the frequency of the grid starts to decrease (a negative derivative), the power converter which is in charge of emulating the inertial response starts to inject power to the grid until the frequency reaches its minimum (when the first derivative is zero), then the frequency starts to increase (a positive derivative) and the converter starts to absorb power. This process will continue until steady-state is achieved. The gain that multiplies the derivative term is known

as the virtual inertia. It is a parameter of the VSM and it is usually considered to be constant. The main effect of adding virtual inertia to the system is that the rate of change of the frequency decreases. However, assuming that all the system parameters remain unchanged, a side effect of adding constant virtual inertia is that the frequency will oscillate for a longer time before settling.

Considering that the first oscillation of the frequency is the most critical one in terms of keeping the system stable, it might be a better approach to have a variable virtual inertia that acts only during the first oscillations following a power disturbance. In this regard, alternative approaches to emulate inertial response that partially solve this problem have been presented in [6, 49], where a power converter injects a predefined amount of constant power during a short period of time to decrease the first frequency drop and its initial rate of change. Despite the effectiveness of these techniques, they do not explore the use of a variable virtual inertia that can change its value during operation, which is one of the main advantages of VSMs over conventional generators [47].

Another function that helps to stabilize frequency is the injection of damping power, which is typically calculated from the difference between a reference frequency and the actual frequency of the system. Any deviation from the reference frequency produces a power that attempts to bring back the grid frequency to the reference, attenuating the amplitude of the oscillations [17, 50]. The gain that multiplies the difference is known as the damping coefficient. In the case of VSMs, the damping coefficient is considered to be constant. Also, one of the main assumptions in the calculation of the damping power is that the refer-

ence frequency, which should be the nominal frequency of the grid, is known. This assumption usually holds true in the case of stiff power systems or APSs that operate in isochronous mode, where a fixed value of frequency can be expected (e.g. 60 Hz). However, this might not be the case of APSs that operate in droop mode, where the frequency of the grid changes with the load level.

In summary, as far as this literature review is concerned, no studies were found on VSMs with the ability of changing parameters during operation, nor on VSMs operating in small power systems that operate with variable frequency. This thesis aims to fill in these gaps in the research related to VSMs.

1.4 SCOPE OF THE THESIS

The main objective of this thesis is to develop a control strategy based on a virtual synchronous machine to support dynamic frequency control in a diesel-hybrid autonomous power system. In particular, this thesis makes the following contributions:

Definition of operating regions: Studies on adding virtual inertia and damping power to a diesel-hybrid APS [51, 52] suggested that, to limit the rate of change and the maximum deviation of the frequency, a combination of virtual inertia and damping power might be a better approach than only emulation of inertia. However, it was not clear how to determine the values for these parameters in order to modify the genset frequency transient response in a certain way. As a solution, graphical representations (called the operating regions) that relate the values of additional inertia and damping power with key parameters of the genset

transient response were proposed.

Development of a diesel generator emulator: An inverter-based diesel generator emulator suitable for fast dynamic transient studies has been implemented [53, 54]. The main purpose of this emulator is the study of frequency variations in a laboratory setting where the operation of a real genset is unfeasible. Experimental results showed that the emulator achieves a satisfactory performance in the transient response as well as in the steady-state response.

Development of a frequency estimator: An estimator for the stabilization frequency of the grid was designed in order to perform the damping function of the VSM when the diesel-hybrid APS operates in frequency droop mode. Simulation and experimental results showed a good performance of the estimator [55].

Development of a self-tuning VSM: The self-tuning VSM (ST-VSM) modifies its parameters according to a real-time optimization that aims to minimize the power flow through the ESS. The effects of the inertial response of the ST-VSM on the frequency transient in a diesel-hybrid APS were investigated in [56, 57]. Then this result was also extended to the damping power function.

1.5   OUTLINE

The thesis is organized as follows. In Chapter 2 the mathematical models of the main components of the diesel generator are developed and simulations are conducted to verify the performance of the model according to the standard ISO 8528-5:2005.

Then, in Chapter 3, the model of the elastic coupling shaft is simplified

to a first order system, which represents the dominant dynamic of the shaft, and a study to investigate the effects of the addition of inertia and damping coefficient on the transient response is performed. From this analysis, a graphical representation of the relation between the additional inertia and damping coefficient and key parameters of the transient response (peak deviation, peak time and initial rate of change) is obtained. This graphical representation is called the operating region.

In **Chapter 4**, an inverter-based genset emulator is implemented. A discrete-time representation of the dynamic model developed in **Chapter 2** is programmed in a DSP and its output voltages are used as references to control the magnitude and frequency of the output voltages of an inverter. Simulations and experimental results are presented to verify the transient and static response of the emulator.

Chapter 5 presents the virtual synchronous machine strategy. A decoupled power control of the grid side converter is developed with a special design for the d-axis current control loop, which has to follow the rapid changes of the reference provided by the VSM. Issues regarding the synchronization of the converter with the grid, the frequency measurement and the implementation of the VSM are discussed. Simulation and experimental results are presented.

The self-tuning VSM is presented in **Chapter 6**. The proposed strategy continuously performs the on-line minimization of a cost function that provides optimal values for the virtual inertia and damping coefficient of the VSM. The cost functions were defined using a predictive model strategy and the search spaces of

the optimization problems were defined using the concept of the operating regions

defined in Chapter 3. The performance of the ST-VSM was evaluated by simula-

tions for step-like load changes and wind power generation.

CHAPTER 2

MODEL OF THE DIESEL GENERATOR

2.1   INTRODUCTION

In a diesel-hybrid APS, the diesel generator is one of the main components because it represents the primary source of energy and establishes the ac voltage in the system. As discussed before in the introductory Chapter, a diesel generator typically consists of a diesel engine coupled by a mechanical shaft to a synchronous generator, the speed governor and the automatic voltage regulator (Fig. 2.1). Under normal operation, the frequency of the output voltage mainly depends on the dynamics associated to the rotational speed of the mechanical shaft, which are much slower compared to the dynamics associated to the voltage control loop. In this Chapter, a model for the diesel generator is developed. Details of the mathematical model and parameters used in simulations can be found in Appendix A.
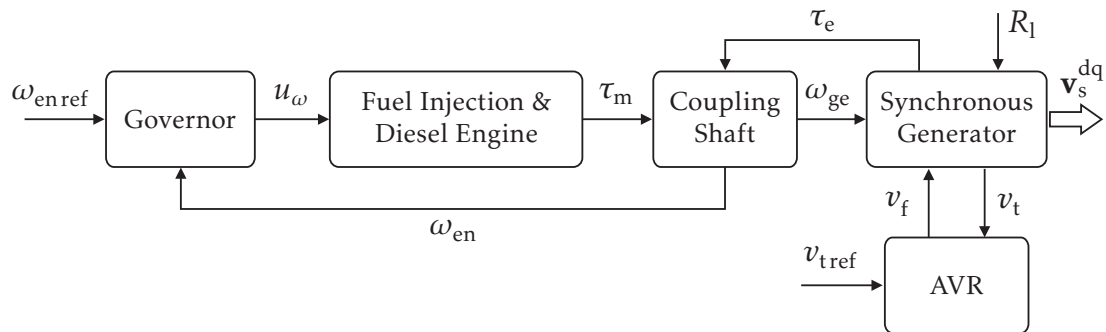
Figure 2.1: Diesel generator model.

2.2   THE MODEL

2.2.1   Diesel Engine and Fuel Injection System

Several models for the diesel engine can be found in the literature [5, 58–62] and the majority of them have in common three main elements: the fuel injection system, a delay time representing the elapsed time from the fuel injection until torque is developed at the engine shaft [59], and the inertia of the internal rotating parts of the engine and flywheel. The effects of the inertia will be included in the model of the coupling shaft, therefore, the differential equation of the model and its corresponding transfer function are:

$$t_e \frac{\mathrm{d}\tau_m}{\mathrm{d}t} = -\tau_m + k_e u_\omega(t - t_d) \tag{2.1}$$

$$h_e(s) = \frac{\tau_m(s)}{u_\omega(s)} = \frac{k_e e^{-t_d s}}{t_e s + 1} \tag{2.2}$$

where u_ω is the control signal from the speed governor and τ_m is the mechanical torque developed by the engine. The parameters are t_e the time constant of the fuel injection system, k_e the gain of the engine, and t_d is the delay time. If the control signal, u_ω, varies within the range $[0,1]$, then the engine gain, k_e, will be the maximum torque developed by the engine. The values of the parameters, summarized in Table A.1, were obtained from the datasheet [63] of a commercially available 33 kW diesel engine and from a 10 kW diesel engine used in the experimental setup in [64].

2.2.2 Coupling Shaft

The coupling shaft of the genset is modeled as two rotational masses coupled by a linear flexible shaft. The diagram of the model is depicted in Fig. 2.2 and the equations are:

$$J_{en}\frac{d\omega_{en}}{dt} = -k_{fens}\omega_{en} + k_{fs}\omega_{ge} - \tau_{ss} + \tau_{m} \tag{2.3a}$$

$$J_{ge}\frac{d\omega_{ge}}{dt} = k_{fs}\omega_{en} - k_{fges}\omega_{ge} + \tau_{ss} - \tau_{e} \tag{2.3b}$$

$$\frac{d\tau_{ss}}{dt} = k_{ss}\omega_{en} - k_{ss}\omega_{ge} \tag{2.3c}$$

where the state variables are ω_{en}, the rotational speed of the prime mover, ω_{ge}, rotational speed of the electrical generator, and τ_{ss}, the torque transmitted through the spring element. The inputs are τ_{m}, the mechanical torque supplied by the engine, and τ_{e}, the electromagnetic torque due to electric load. The parameters are J_{en}, J_{ge} the moments of inertia; k_{fen}, k_{fge} the frictional losses coefficients of the engine and electrical generator; k_{fs} and k_{ss} the torsional damping and stiff-
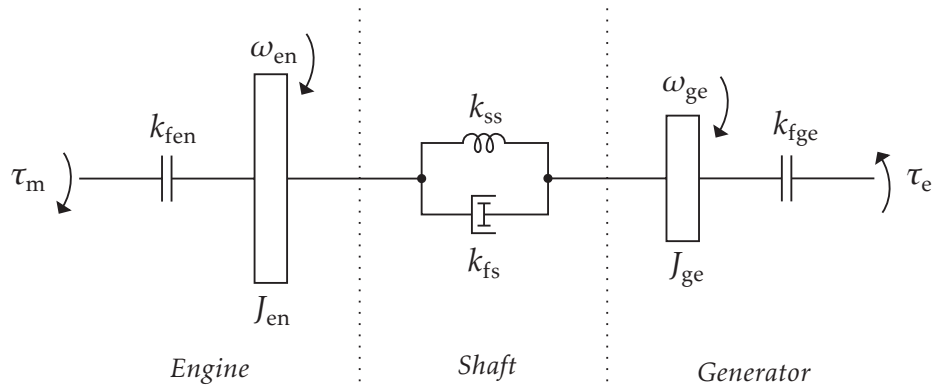
Figure 2.2: Diagram of the coupling shaft.

ness coefficients of the shaft. To simplify the notation, the following parameters were defined $k_{\mathrm{fens}} = k_{\mathrm{fen}} + k_{\mathrm{fs}}$ and $k_{\mathrm{fges}} = k_{\mathrm{fge}} + k_{\mathrm{fs}}$. The parameters of model (2.3) were obtained from datasheets [63, 65, 66] and they are summarized in Table A.1, Table A.2 and Table A.3. For a later analysis of the transient response, system (2.3) is written in the state-space form (A.2) and the transfer function $\omega_{\mathrm{en}}(s)/\tau_{\mathrm{m}}(s)$ (A.4) is obtained.

2.2.3 Electrical Generator

The synchronous generator (SG) is represented by model 2.1 of the IEEE Std. 1110-2002 for the modeling of synchronous generators [67]. This model was chosen because of two reasons: first, as mentioned in [67], data supplied by manufacturers is usually based on its structure and, second, it is the model used by the simulation software used in this thesis. Since this is a well-documented model, only the most important equations are presented. For a detailed derivation of equations and analysis refer to [5, 67]. Fig. 2.3 shows the electrical circuits associated to model 2.1, which consist of two windings in the rotor d-axis—the field and damper windings—and a single damper winding in the rotor q-axis. The corresponding dynamic equations are typically formulated in terms of the flux linkages on each winding as follows:

$$\frac{\mathrm{d}\psi_{\mathrm{s}}^{\mathrm{d}}}{\mathrm{d}t} = n_{\mathrm{pp}}\omega_{\mathrm{ge}}\psi_{\mathrm{s}}^{\mathrm{q}} - (R_{\mathrm{s}} + R_{\mathrm{l}})\,i_{\mathrm{s}}^{\mathrm{d}} \tag{2.4a}$$

$$\frac{\mathrm{d}\psi_{\mathrm{s}}^{\mathrm{q}}}{\mathrm{d}t} = -n_{\mathrm{pp}}\omega_{\mathrm{ge}}\psi_{\mathrm{s}}^{\mathrm{d}} - (R_{\mathrm{s}} + R_{\mathrm{l}})\,i_{\mathrm{s}}^{\mathrm{q}} \tag{2.4b}$$
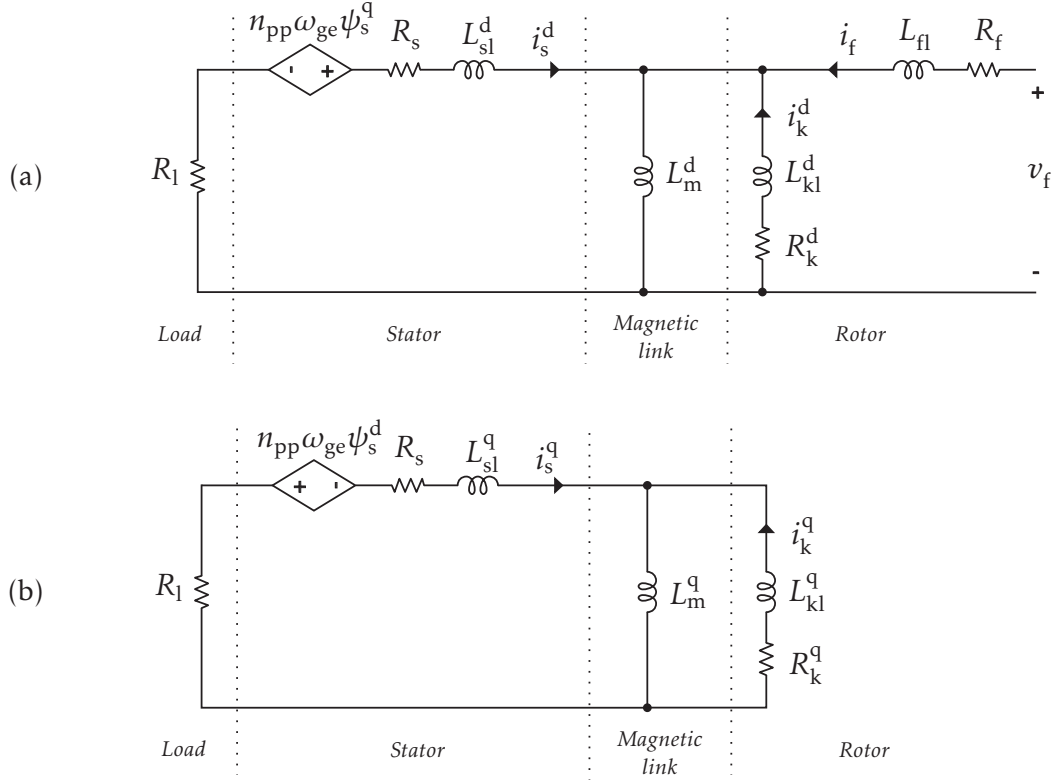
Figure 2.3: Electrical circuits of the dq model of the synchronous machine.

(a) d-axis circuit. (b) q-axis circuit.

$$\frac{\mathrm{d}\psi_f}{\mathrm{d}t} = -R_f i_f + v_f \tag{2.4c}$$

$$\frac{\mathrm{d}\psi_k^d}{\mathrm{d}t} = -R_k^d i_k^d \tag{2.4d}$$

$$\frac{\mathrm{d}\psi_k^q}{\mathrm{d}t} = -R_k^q i_k^q \tag{2.4e}$$

where ψ_s^d and ψ_s^q represent the flux linkages in the stator windings, ψ_k^d and ψ_k^q the flux linkages in the rotor damper windings, and ψ_f the flux linkages in the rotor field winding. On the other hand, i_s^d and i_s^q represent the stator currents, i_k^d and i_k^q the damper currents, and i_f the field current. The relations between the currents and the flux linkages are given in (A.5). The inputs of the model are the generator

speed ω_{ge}, which is given by the model of the coupling shaft; and the field voltage v_f, which is given by the AVR. The outputs of the model are defined as:

$$\tau_e = \frac{3}{2} n_{pp} \left(\psi_s^d i_s^q - \psi_s^q i_s^d \right) \tag{2.5a}$$

$$v_t = \sqrt{\frac{3}{2}} R_l \sqrt{i_s^{d2} + i_s^{q2}} \tag{2.5b}$$

where τ_e is the the electromechanical torque, which is an input for the model of the coupling shaft; and v_t is the rms value of the terminal voltage of the SG, which is controlled by the AVR.

The parameters of the model are n_{pp}, the number of pole pairs of the rotor, R_s, the stator resistance, R_f, the field resistance, R_k^d and R_k^q, the damper resistances, L_m^d and L_m^q, the mutual inductances, L_{sl}^d and L_{sl}^q, the stator leakage inductances, L_{kl}^d and L_{kl}^q, the damper leakage inductances, L_{fl}, the field leakage inductance, and R_l, the load resistance. The values for the parameters, presented in Table A.3, were obtained from the datasheet [65] of a commercially available 38 kVA synchronous generator. The linear model of the SG, which will be used later, was derived from the nonlinear model (2.4) with outputs (2.5) and is presented in Section A.3.

2.2.4 Automatic Voltage Regulator (AVR)

The model for the AVR is built based on information from the IEEE Std. 421.5 [68] and the datasheet [65] of the SG modeled in the previous section. The model consists of a single-phase thyristor rectifier—modeled as a first order system [69]—controlled by a proportional-integral (PI) controller. A block

diagram of the AVR is shown in Fig. 2.4, and the corresponding equations are:

$$\frac{dz_v}{dt} = k_{iv}\left(v_{tref} - v_t + u_v - y_v\right) \tag{2.6a}$$

$$y_v = z_v + k_{pv}\left(v_{tref} - v_t\right) \tag{2.6b}$$

$$t_{rec}\frac{dv_f}{dt} = -v_f + k_{rec}u_v \tag{2.6c}$$

where the variables are v_t the measured terminal voltage from the SG model, v_{tref} the terminal voltage reference, z_v the integrator state, y_v the non-saturated output of the controller, u_v the saturated output of the controller, and v_f the output voltage of the rectifier which is the input voltage for the SG field winding. The parameters are k_{pv} the proportional control gain, k_{iv} the integral control gain, t_{rec} and k_{rec} the time constant and gain of the rectifier. The anti-windup function is accomplished by compensating the input to the integrator with the difference between the saturated and the non-saturated outputs of the PI controller [70].
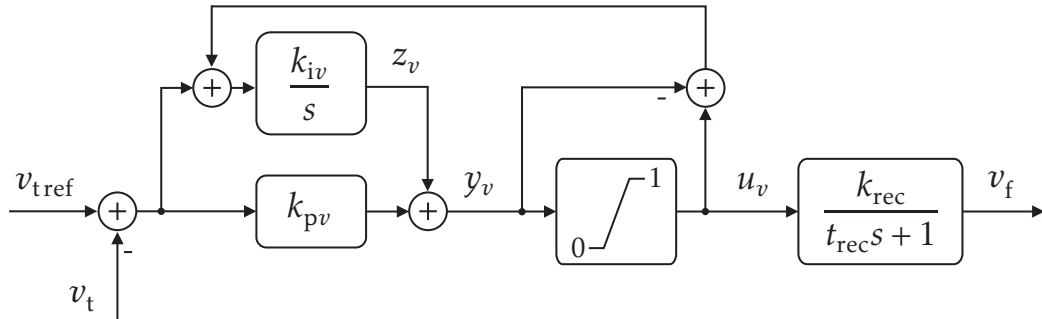
Figure 2.4: Block diagram of the automatic voltage regulator.

2.2.5 Speed Governor

The speed governor [71] has the structure of a PI controller with the droop function implemented by the feedback of the controller output. A block diagram of the governor is shown in Fig. 2.5, and the corresponding equations are:

$$\frac{dz_\omega}{dt} = k_{i\omega} \left(\omega_{enref} - \omega_{en} - k_{dr} u_\omega + u_\omega - y_\omega \right) \tag{2.7a}$$

$$y_\omega = z_\omega + k_{p\omega} \left(\omega_{enref} - \omega_{en} - k_{dr} u_\omega \right) \tag{2.7b}$$

where the variables are ω_{enref} the speed reference, z_ω the integrator state, y_ω the non-saturated output of the controller, and u_ω the saturated output of the controller. The parameters are $k_{p\omega}$ the proportional control gain, $k_{i\omega}$ the integral control gain, and k_{dr} the speed droop gain. The speed droop gain is defined as $k_{dr} = m_{dr} \Omega_{en}$, where m_{dr} is the static droop slope, and Ω_{en} is the prime mover nominal speed. The output saturation range $[0, 1]$ is necessary to account for the operating stroke of the actuator [72]. As in the case of the AVR, the speed governor is also provided with the anti-windup function.
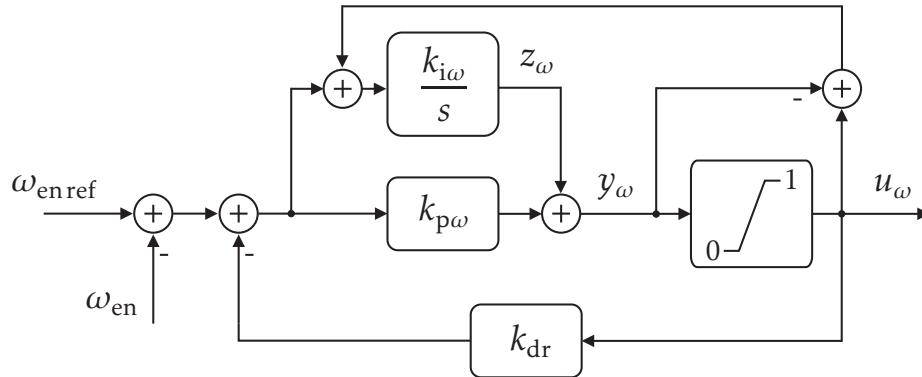
Figure 2.5: Block diagram of the speed governor.

2.3 SIMULATIONS

The AVR and speed governor were tuned by trial-and-error, with the genset operating in isochronous mode, to comply with the transient performance of the class G3 of the standard ISO 8528-5:2005 [73]. Controller parameters used in the simulation are presented in Table A.4 and Table A.5. Two tests of the standard were simulated to verify the transient performance of the genset. The first simulation was a 100% load rejection test. The genset was operated in isochronous mode and it started in a full-load condition of 33 kW, which is the genset continuous output power (P_{cp}). Fig. 2.6 shows the simulation results, where Fig. 2.6(a) shows the rms value of the terminal voltage and Fig. 2.6(b) the rotational speeds of the shaft model.

The second simulation was a load acceptance test that entailed a sudden load increase. The datasheet [63] of the diesel engine specifies that it can accept a load increase of up to 100% of its continuous output power in a single stage, then the value of 90% was selected for this simulation. The genset was operated in isochronous mode and it started in a no-load condition. Fig. 2.7 shows the simulation results, where Fig. 2.7(a) shows the rms value of the terminal voltage and Fig. 2.7(b) the rotational speeds of the shaft model.

Table 2.1 presents the transient parameters obtained from the two previous simulations and the corresponding specifications of the standard. The maximum deviations are measured with respect to the initial value of the variable, and the recovery time corresponds to the elapsed time from the moment the dis-

(a)

(b)
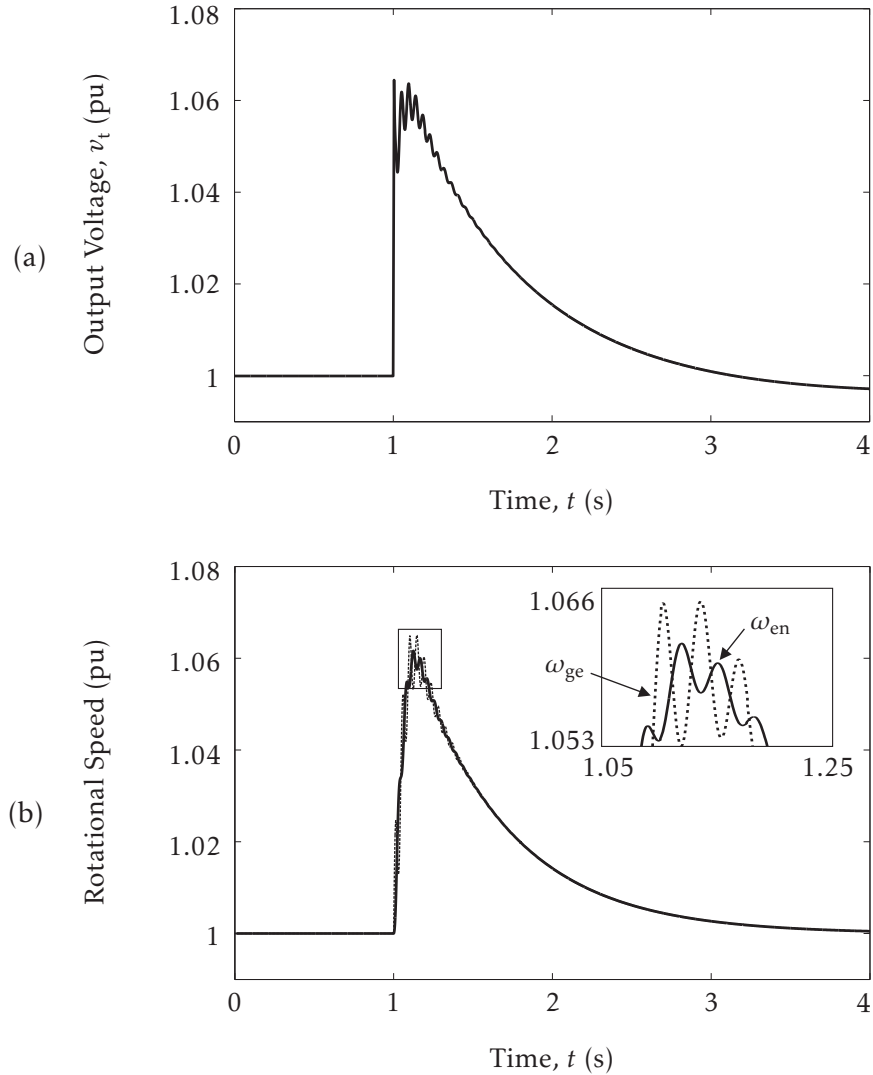
Figure 2.6: Load rejection test under isochronous operation.

Waveforms for a 100 % load decrease at $t = 1$ s. (a) rms value of the output terminal voltage. (b) Shaft rotational speeds, with a detailed view of the prime mover speed, ω_{en}, and generator speed, ω_{ge}.

turbance occurs until the variable enters and remains in the settling band (± 1 %

for the voltage and ± 0.25 % for the frequency). The results show that, under the

conditions of the simulated tests, the model performs according to the standard.

However, it must be noted that the standard consists of a large number of specifi-

cations, from which the ones presented in Table 2.1 were chosen according to the
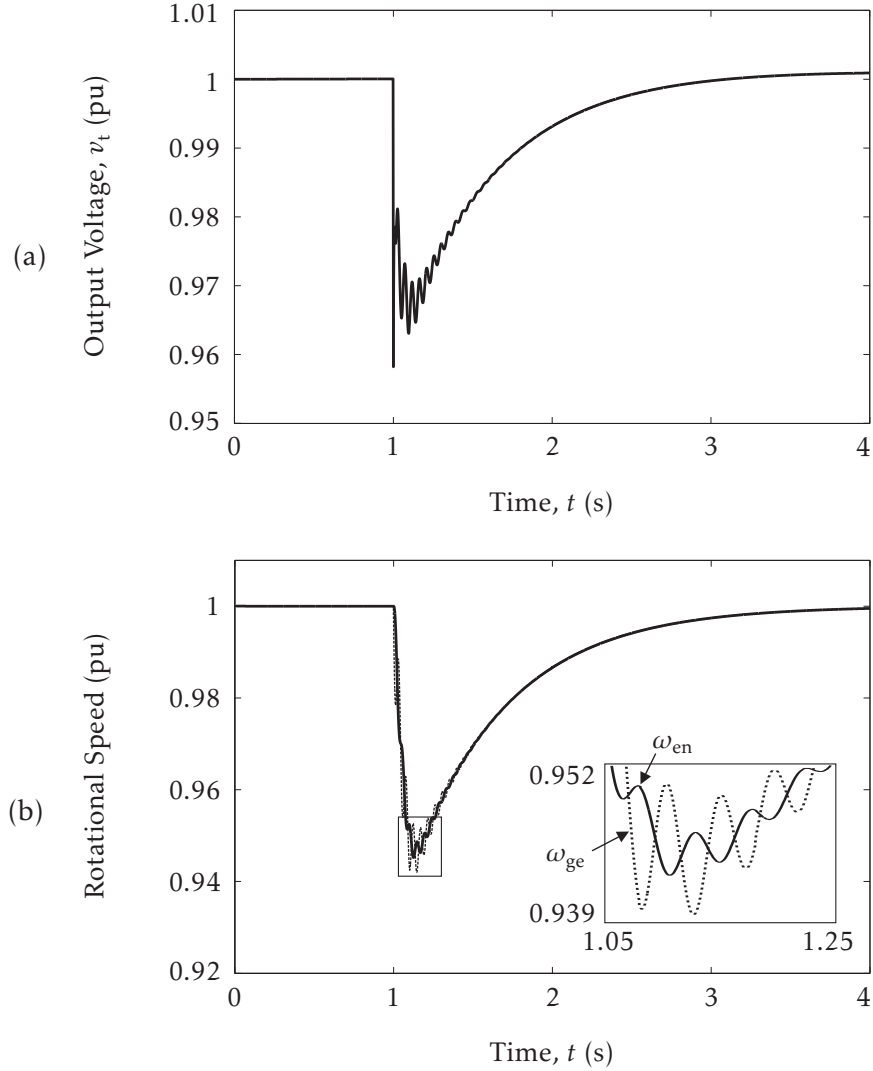
Figure 2.7: Load acceptance test under isochronous operation.

Waveforms for a 90 % load increase at $t = 1$ s. (a) rms value of the output terminal voltage. (b) Shaft rotational speeds, with a detailed view of the prime mover speed, ω_{en}, and generator speed, ω_{ge}.

purpose of the model, which is to investigate frequency stability in diesel-hybrid APSs.

Finally, a third simulation is performed to verify the transient performance of the model for three different values of speed droop: 0 %, 3 % and 5 %. The simulation consists of a load increase of 50 % of the P_{cp}, starting from a no-

Table 2.1: Comparison between simulation results and class G3 ISO 8528-5:2005.

Specification	Frequency*		Voltage†	
	ISO Std.	Simulation	ISO Std.	Simulation
Maximum deviations due to 100 % load decrease	$\leq 10\%$	6.5 %	$\leq 20\%$	6.5 %
Recovery time after 100 % load decrease	$\leq 3\,\mathrm{s}$	2.2 s	$\leq 4\,\mathrm{s}$	1.3 s
Maximum deviations due to sudden load increase	$\leq 7\%$	5.6 %	$\leq 15\%$	3.6 %
Recovery time after sudden load increase	$\leq 3\,\mathrm{s}$	1.9 s	$\leq 4\,\mathrm{s}$	0.8 s

*Steady state tolerance band $\leq \pm0.25\%$
†Steady state tolerance band $\leq \pm1\%$

load condition. Fig. 2.8 shows the simulation results.

Fig. 2.8(a) shows the waveforms of the rms value of the terminal voltage, where it is observed that the performance of the AVR changes as the droop increases. The maximum deviation is not significantly affected, but the recovery time is almost doubled for a droop of 5 % in comparison to the isochronous mode. However, it remains lower than the limit of the standard, because the original recovery time—for isochronous mode—was designed with a relatively low value.

Fig. 2.8(b) shows the waveforms of the rotational speed of the diesel engine, where it is observed that the maximum deviations increase as the value of the droop increases. Nevertheless, they still comply with class G3 specifications, because the standard relaxes the limit according to the value of the droop factor. On the other hand, the recovery time is not significantly affected.

(a)

(b)
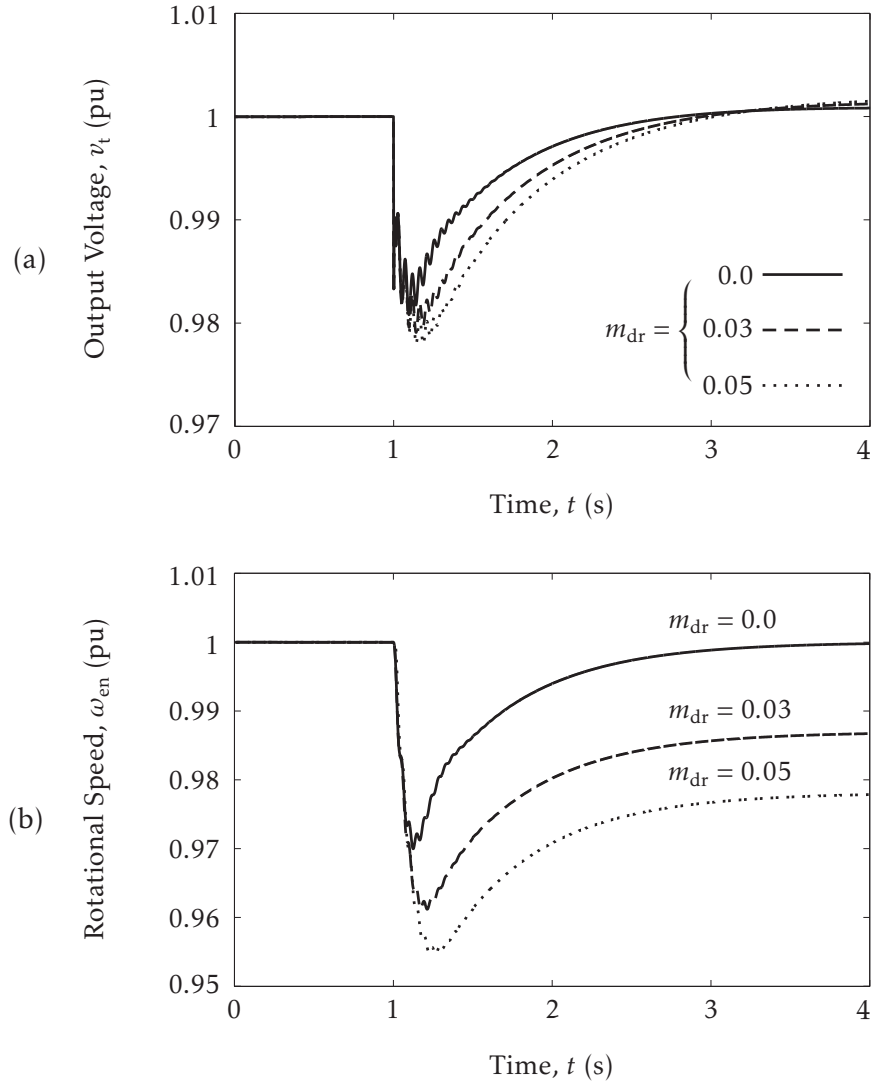
Figure 2.8: Load acceptance test under droop operation.

Waveforms for a 50 % load increase at $t = 1$ s and three different values of speed droop m_{dr}. (a) rms value of the output terminal voltage. (b) Prime mover rotational speed.

2.4 DISCUSSION AND CONCLUSIONS

The modelling and simulation of a diesel generator have been presented in this Chapter. The model consists of five subsystems representing: the fuel injection and diesel engine, the coupling shaft, the electrical generator, the speed governor, and the automatic voltage regulator. The parameters of the model were obtained from datasheets of commercially available components, and the parameters of the speed governor and AVR were selected by trial and error so the transient performance of the model complies with class G3 of the standard ISO 8528-5:2005 for isochronous operation.

Simulations were conducted to evaluate the transient performance of the model for speed droop operation. Considering a step-like load increase from no-load to 50 % of the continuous output power of the genset and speed droops of 3 % and 5 %, results showed that the overall transient response is deteriorated as the droop increases, however the maximum deviations and recovery times remain within the limits of the standard, for which the controllers were tuned.

Chapter 3

Analysis of the Genset Frequency Transient Response

3.1 Introduction

As it was mentioned in the introductory Chapter, the main objective of this thesis is to develop a control strategy that uses an energy storage system to emulate inertial response and inject damping power to support dynamic frequency control in a diesel-hybrid APS. Ideally, such a control strategy—a virtual synchronous machine—would produce the same results as if the inertia and damping torque of the diesel generator were changed [51]. Therefore, before designing such a control strategy, it might be useful to have a better understanding of how these parameters affect the frequency transient response of a diesel generator. The latter is investigated in this Chapter.

In order to characterize the frequency transient response due to a step-like power disturbance, as shown in Fig. 3.1, the following quantities are defined:

i)   Peak frequency deviation, Δf_p: the maximum frequency deviation, relative to its initial value, following a power disturbance. When referred as the peak frequency (measured in absolute terms) is represented by f_p.

ii)   Peak time, t_p: the elapsed time from the moment the disturbance is applied until the peak frequency occurs.

iii)   Initial rate of change, roc_f: a measure of how fast the system reacts to the
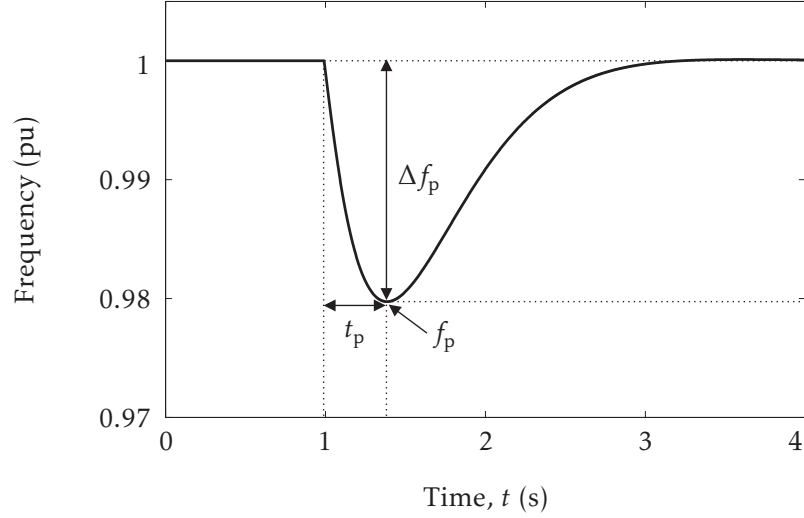
Figure 3.1: Transient response characterization.

disturbance and is calculated as $\text{roc}_f = \Delta f_\text{p}/t_\text{p}$.

3.2   REDUCED-ORDER MODEL OF THE COUPLING SHAFT

The third-order model of the coupling shaft (2.3) is a good representation of the phenomena associated to the elasticity of the shaft, however it produces high frequency oscillations in the speed variables that complicate the task of finding f_p, t_p and roc_f. Therefore, for purpose of finding these parameters of the transient response, a reduced-order model is employed. The two-mass model of Fig. 2.2 can be simplified to an equivalent single-mass model by assuming a perfectly rigid coupling shaft where there is no dynamic interaction between the engine and the generator ($\omega_\text{en} = \omega_\text{ge}$, $\forall t$). Then, model (2.3) is reduced to the following first-order model:

$$J_\text{eq}\frac{\text{d}\omega_\text{eq}}{\text{d}t} = -k_\text{feq}\omega_\text{eq} + \tau_\text{m} - \tau_\text{e} \tag{3.1}$$

and its corresponding transfer function:

$$h_{eq}(s) = \frac{\omega_{eq}(s)}{\tau_m(s)} = \frac{1}{J_{eq}s + k_{feq}} \tag{3.2}$$

where ω_{eq} is the equivalent rotational speed of the diesel engine-electrical generator set, $J_{eq} = J_{en} + J_{ge}$ is the equivalent moment of inertia and $k_{feq} = k_{fen} + k_{fge}$ the equivalent frictional losses coefficient.

3.2.1 Comparison of Single-Mass and Two-Mass Models

From Table 3.1 it can be observed that the real part of the complex poles of transfer function $h_{sh11} = \omega_{en}(s)/\tau_m(s)$ (defined in (A.4)) is 65 times greater than its real pole ($\mathcal{Re}(p_2)/\mathcal{Re}(p_1) \approx 65$). Therefore, we can consider h_{sh11} as a first-order dominant system which behaves similar to h_{eq} at low frequencies, with both models having the same gain in steady-state ($1/k_{feq}$). From Fig. 3.2 can be noted that for frequencies over 50 rad/s both transfer functions differ in magnitude and phase, however in that range of frequencies the attenuation is greater than -40 dB. In conclusion, transfer function h_{eq} might be considered as a reduced-order repre-

Table 3.1: Poles and zeros of coupling shaft models.

Description	Symbol	Real Part ($\mathcal{Re}$)	Imaginary Part ($\mathcal{Im}$)
h_{eq} real pole	p_{eq}	-0.1154	0
h_{sh11} real pole	p_1	-0.12	0
h_{sh11} complex poles	$p_{2,3}$	-7.85	± 139.6
h_{sh11} complex zeros	$z_{1,2}$	-5.76	± 119.38
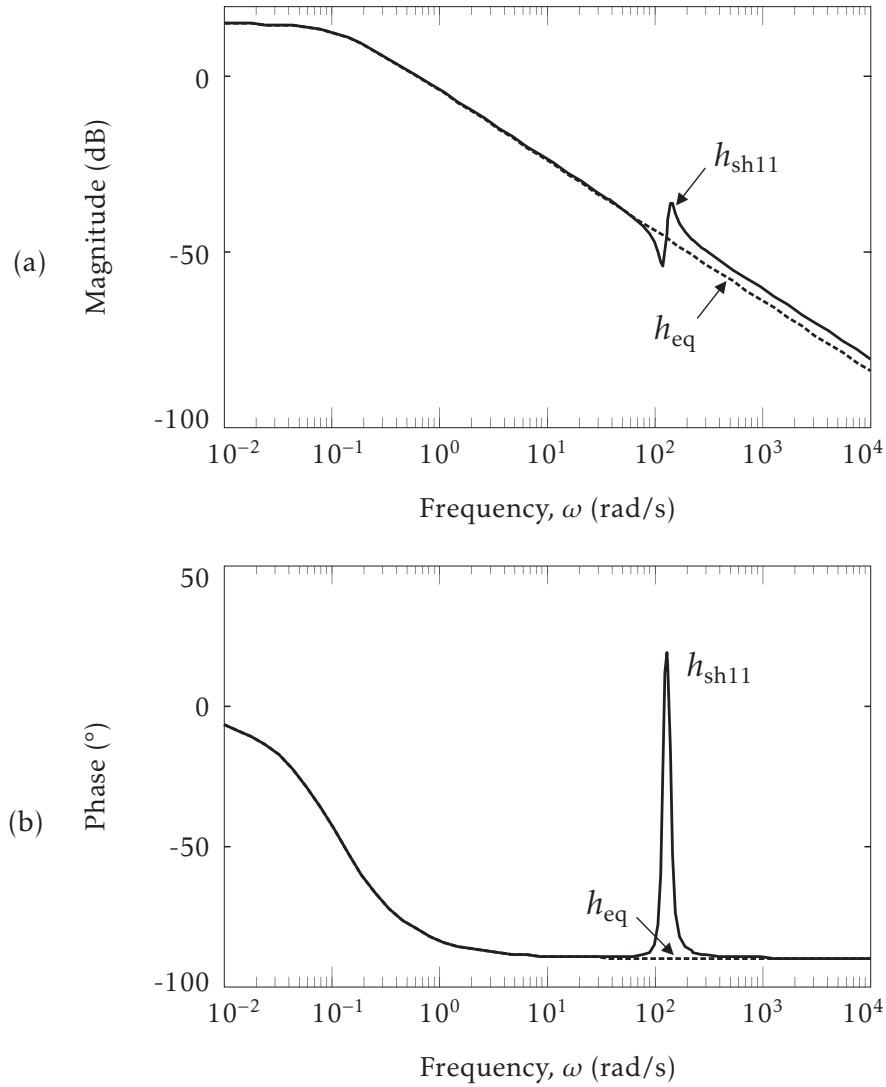
Figure 3.2: Bode plots of coupling shaft models.

Comparison between transfer functions of the two-mass model, h_{sh11}, and the equivalent single-mass model, h_{eq}. (a) Magnitude plot. (b) Phase plot.

sentation of h_{sh11}.

A simulation is performed to compare the genset transient response for both models of the coupling shaft. From the results shown in Fig. 3.3, it is observed that, as it was anticipated from the analysis in the frequency domain, the reduced-order model is a good representation of the dominant dynamic of the elastic coupling shaft. Also, the equivalent frequency waveform, ω_{eq} in Fig. 3.3(b), looks
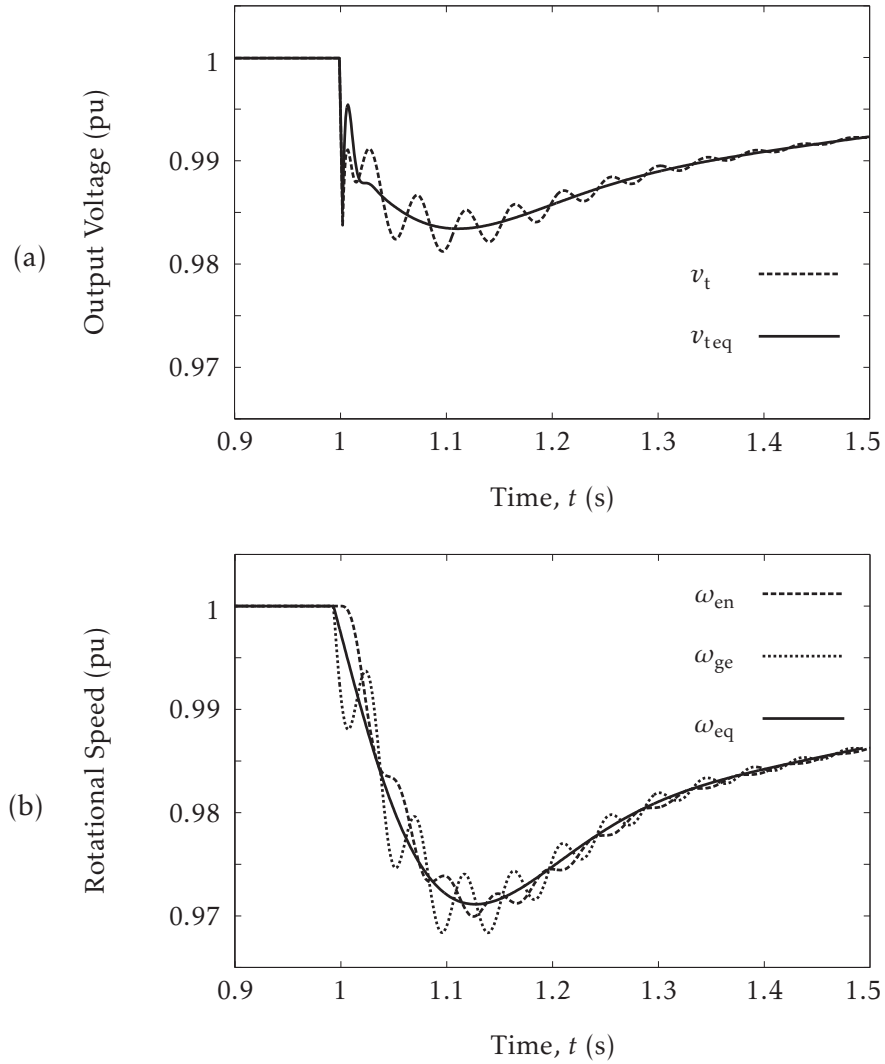
Figure 3.3: Genset transient response for two different coupling shaft models.

Waveforms for a 50 % load increase at $t = 1\,\text{s}$, and considering coupling shaft models (2.3) and (3.1). (a) rms value of the output terminal voltage. (b) Coupling shaft rotational speeds.

more suitable for the calculation of the frequency peak. As a form of comparison between the waveforms depicted in Fig. 3.3(b), consider that the peak frequency calculated from ω_{ge} is $0.9685\,\text{pu}$, from ω_{en} is $0.9704\,\text{pu}$ and from ω_{eq} is $0.9713\,\text{pu}$. Then, taking the average of the first two ($\bar{\omega} = 0.9695$) as an hypothetical but plausible value of actual frequency, the error in the peak frequency calculated from ω_{ge} and ω_{en} would be $\sim 0.1\,\%$ and from ω_{eq} it would be $\sim 0.2\,\%$. This shows that the

error in the peak frequency calculated from ω_{eq} is relatively low and in the same order of magnitude than the errors obtained with the higher-order model.

3.3 EFFECTS OF ADDITIONAL INERTIA AND DAMPING

The model used for the study of the effects of additional inertia and damping is the one presented in **Chapter 2**, but replacing the model of the coupling shaft by its first-order equivalent model (3.1). The transient frequency response of this model, shown in Fig. 3.4, is obtained for different values of additional inertia, J_a, and damping, D_a. The additional inertia is added to the equivalent inertia of the model, J_{eq}, and the additional damping is added in the form of damping torque to the sum block at the input of the coupling shaft. Fig. 3.5 show the simulation results of the genset response to a 50 % step-like load increase from no-load initial condition, when it operates in isochronous mode ($m_{dr} = 0$).

Fig. 3.5(a) depicts the output frequency for different values of additional inertia J_a, while the rest of the parameters remain constant. It is observed that the higher the inertia the lower the initial rate of change of frequency is, which can be
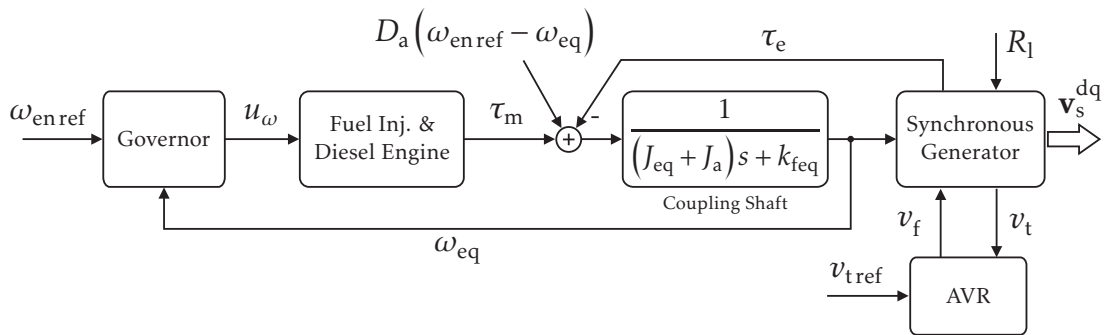
Figure 3.4: Genset model with first-order coupling shaft and additional inertia and damping.
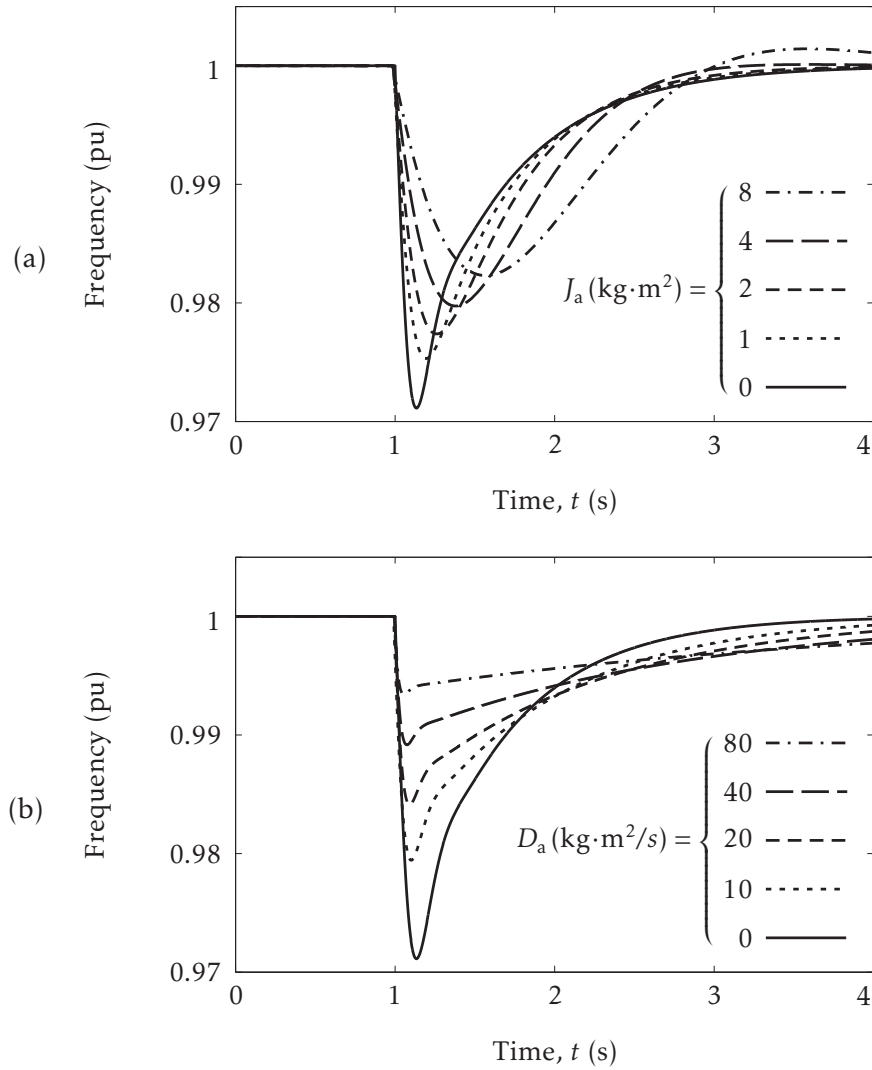
Figure 3.5: Effects of the inertia and damping on a frequency transient.
(a) Frequency transient for different values of additional inertia and zero additional damping. (b) Frequency transient for different values of additional damping and zero additional inertia.

seen right after the load change takes place ($t = 1$ s). Also the peak frequency deviation is reduced by increasing the inertia, however, the system response becomes more oscillatory. On the other hand, Fig. 3.5(b) depicts the output frequency for different values of additional damping coefficient D_a, while the rest of the parameters remain constant. It is observed that increasing the additional damping produces a reduction in the peak frequency deviation, but the system reaches the

peak value more rapidly.

3.3.1 Operating Region

So far, the effects of additional inertia and damping on the frequency transient response have been explored separately. The proposed concept of operating region would provide a single graphical representation where it is possible to appreciate the combined effect of varying both parameters on the frequency transient response. In order to obtain the operating region, the previously defined quantities: f_p, t_p and roc_f are plotted as functions of the additional inertia, J_a, and damping coefficient, D_a. Furthermore, to account for the effect of the speed droop control, the resulting surfaces are parametrized upon the droop factor, m_{dr}. The surfaces related to the peak frequency are defined as:

$$\sigma_f = \left\{ \left(J_a, D_a, f_p \left(J_a, D_a \right) \big|_{m_{dr}=c} \right) \subset \mathbb{R}^3 : \left(J_a, D_a \right) \in U \right\} \tag{3.3}$$

the surfaces related to the peak time as:

$$\sigma_t = \left\{ \left(J_a, D_a, t_p \left(J_a, D_a \right) \big|_{m_{dr}=c} \right) \subset \mathbb{R}^3 : \left(J_a, D_a \right) \in U \right\} \tag{3.4}$$

and the surfaces related to the rate of change as:

$$\sigma_r = \left\{ \left(J_a, D_a, \text{roc}_f \left(J_a, D_a \right) \big|_{m_{dr}=c} \right) \subset \mathbb{R}^3 : \left(J_a, D_a \right) \in U \right\} \tag{3.5}$$

where U is the subspace that defines all the possible combinations for parameters (J_a, D_a), and c is a constant that represents the value of the speed droop factor that parametrizes the surfaces.

Fig. 3.6 presents the results for the peak frequency considering the subspace $U = [0,5] \times [0,50]$. Fig. 3.6(a) shows three parametrizations of surface σ_f, namely: σ_{f1} defined for $m_{dr} = 0$, σ_{f2} defined for $m_{dr} = 0.03$, and σ_{f3} defined for
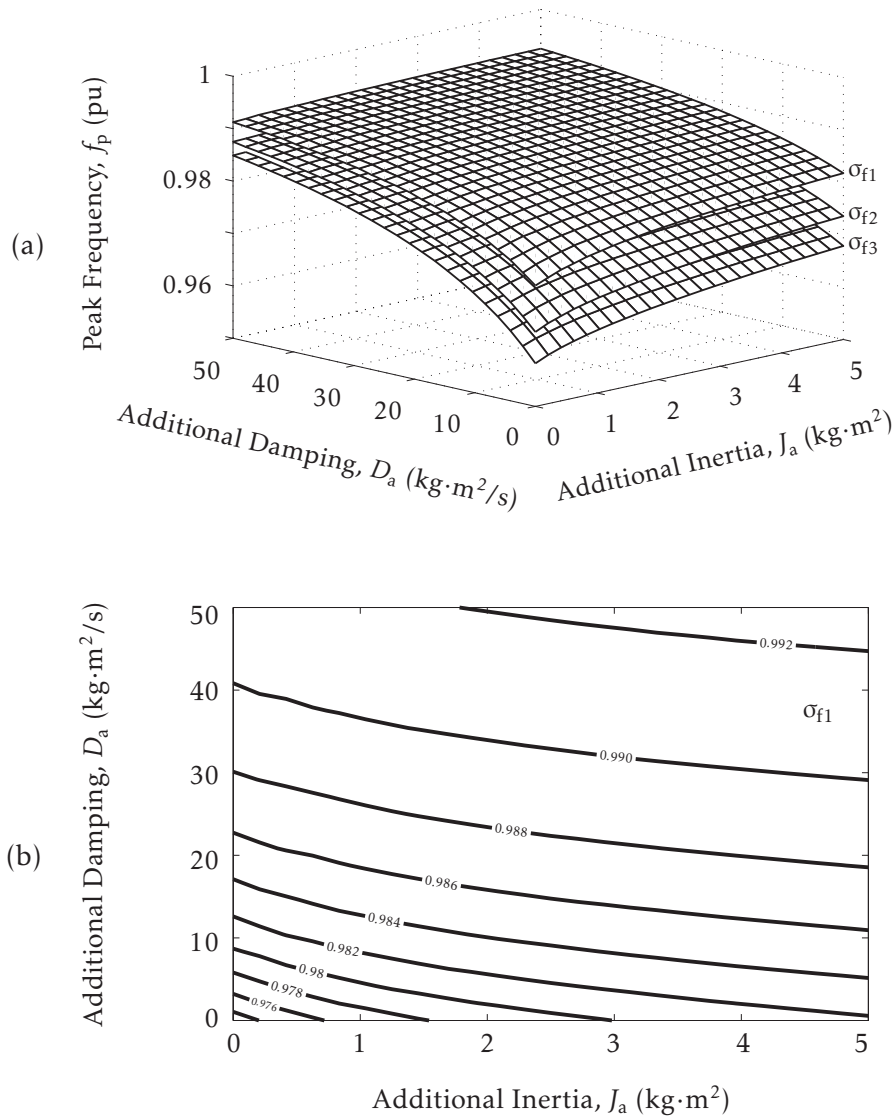
Figure 3.6: Characterization of the peak frequency.

(a) Three parametrizations of surface σ_f. (b) Contour map for σ_{f1} ($m_{dr} = 0$).

$m_{dr} = 0.05$. Fig. 3.6(b) shows the contour map of σ_{f1}. The same results are presented for the peak time in Fig. 3.7 and for the rate of change in Fig. 3.8.

Now, the contour maps of Fig. 3.6(b), Fig. 3.7(b) and Fig. 3.8(b) are superimposed and presented in one graph shown in Fig. 3.9. Here it is possible to define an operating region as a set of points in U where the frequency transient response satisfies certain specifications in terms of peak value, peak time and initial rate of
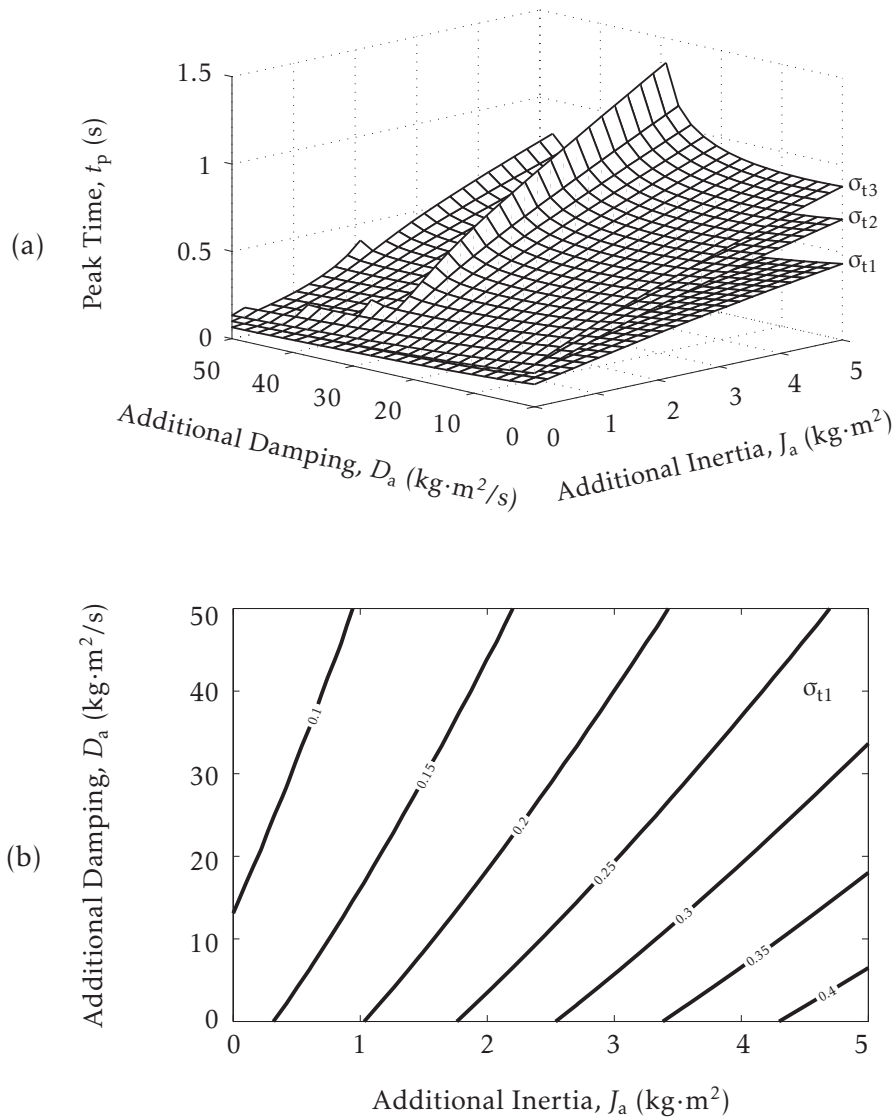
Figure 3.7: Characterization of the peak time.

(a) Three parametrizations of surface σ_t. (b) Contour map for σ_{t1} ($m_{dr} = 0$).

change. Fig. 3.9 presents an example of an operating region $\mathcal{A}$ that shows what are the range of values of additional inertia and damping that modify the transient response of Fig. 3.3(b), so it is bounded to $f_p \in [0.98, 0.99]$, $t_p \in [0.15, 0.3]$, and $\text{roc}_f \in [-0.06, -0.1]$. As it will be shown later in **Chapter 6**, these operating regions can be used to design a control strategy that support frequency control during the transient.
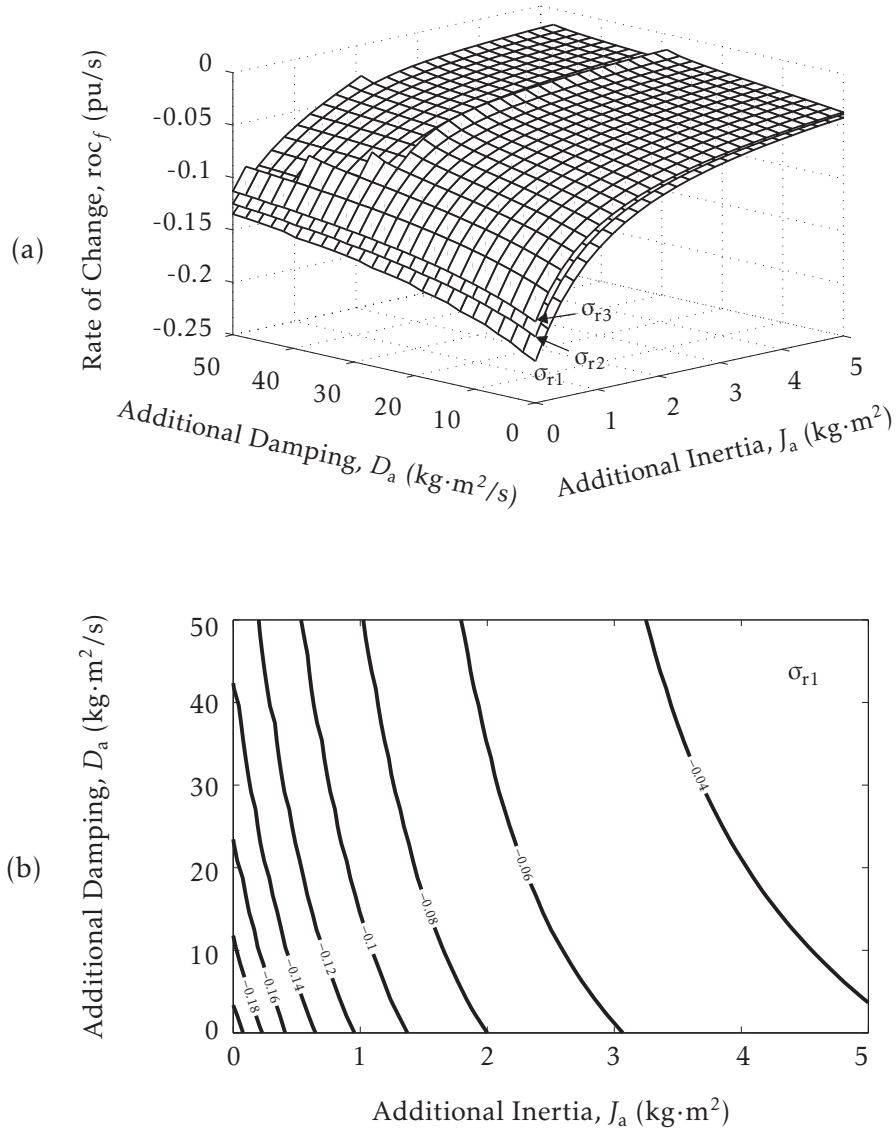
Figure 3.8: Characterization of the frequency rate of change.

(a) Three parametrizations of surface σ_r. (b) Contour map for σ_{r1} ($m_{dr} = 0$).
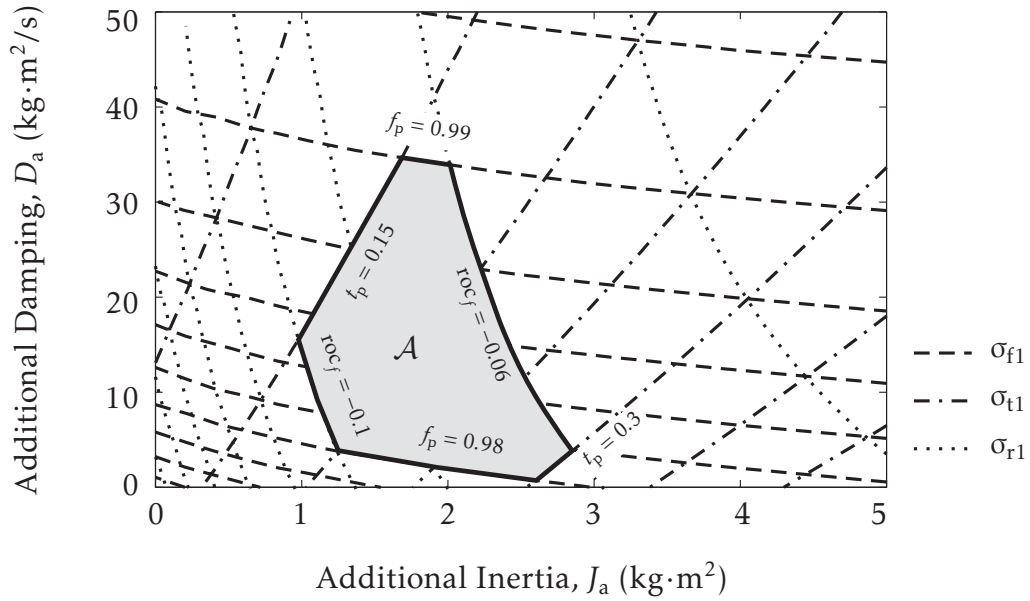
Figure 3.9: Definition of an operating region.

3.4 DISCUSSION AND CONCLUSIONS

The frequency transient response of the genset was characterized in terms of its peak frequency deviation, peak time and rate of change. Then, using a reduced-order model for the coupling shaft, the effects of additional inertia and damping on the frequency transient were investigated. Finally, the concept of operating region was proposed as a way to identify a set of values (J_a, D_a) for which the frequency transient satisfies certain specifications in terms of peak frequency deviation, peak time and rate of change.

During the studies conducted in this Chapter, it was observed that most of the benefits of adding inertia are obtained during the initial part of the frequency deviation. After that happens, the additional inertia seems to deteriorate the transient response. In a similar way, it was observed that the additional damping helps

to attenuate the frequency oscillations, but it increases the initial rate of change.

Since the above problem originates because the governor has been tuned considering only the values of the original parameters, a solution could be the re-tuning of the speed governor each time the additional inertia and damping are changed. However, this approach would create dependence between the tuning of the governor and the values of the additional inertia and damping. Another solution could be the design of a robust control strategy for the governor capable to handle variations in the parameters of the system. Although these are plausible solutions to compensate for the addition of inertia and/or damping to the system, they have to be implemented in the genset side. On the contrary, the operating regions allow knowing a priori how the additional inertia and damping will affect the transient response, and therefore it is possible to find a solution without modifying the governor. The application of the operating regions in the design of a VSM will be shown in Chapter 6.

CHAPTER 4

INVERTER-BASED DIESEL GENERATOR EMULATOR

4.1 INTRODUCTION

The main motivation for developing the emulator is that most laboratory facilities are not suitable for the operation of a real diesel generator because of the noise and combustion gases, among other factors. In addition, the advantage of an inverter-based emulator over a machine-based one is that the emulated machine can have, to some extent, desired characteristics for a particular test and it can also include characteristics of the mechanical load or prime mover [74]. In this case the emulator represents a diesel generator, which basically consists of a synchronous generator with voltage control driven by a diesel engine with speed control.

Previous research on the emulation of electrical machines with power converters has been conducted in [74, 75] and more recently in [76, 77]. The main purpose of these emulators was the testing of machine drive systems, where the inverter currents are controlled using the output currents of the emulated machine as references. It is implicit here that the stator voltage is measured from the grid and supplied to the machine model when solving the equations to obtain the output currents. However, in this case, it is the diesel generator that provides the voltage, and therefore, it is the stator voltage that has to be controlled instead of the currents. For this reason, as it will be shown later, capacitors are included

in the output of the inverter and the control strategy for the inverter is voltage control with inner current control loops.

4.2 SYSTEM OVERVIEW

A block diagram of the emulator system is shown in Fig. 4.1. The voltage source inverter (VSI) is a three-phase two-level topology with an *LC* output filter. The dc power for the inverter is supplied by a three-phase full wave diode rectifier and the load is a variable resistor bank. The digital control system is based on the Spectrum Digital development kit eZdsp-F2812 (DSP), where all the programming is developed in C language. A local personal computer (PC) connected to the DSP via a JTAG interface is needed for programming and local operation. The main tasks of the DSP, in order of execution, are: measure the voltage and currents from the power circuit, run the model of the genset, and use the output
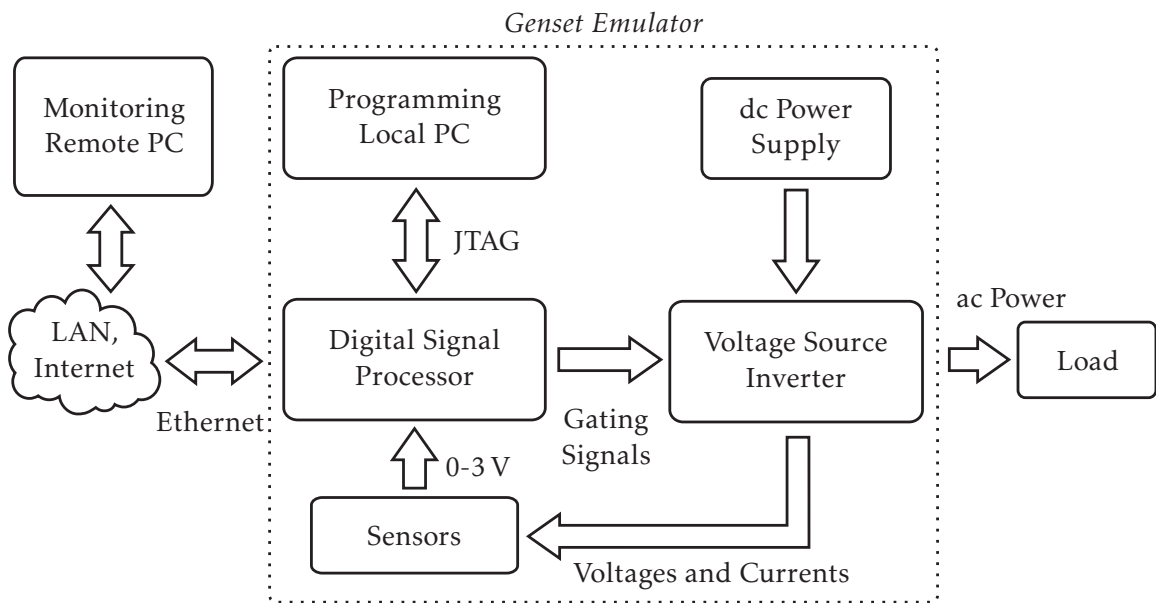
Figure 4.1: Block diagram of the genset emulator.

voltage of the model to control the output voltage of the inverter. The DSP controls the inverter through the gating signal, which are a set of six pulse-width modulated signals in the range of [0,3] V. Since the inverter requires signals of 15 V, a voltage step-up circuit is required. The voltage and current sensors have both the same structure: a Hall-effect transducer at the input and a gain and offset conditioning stage at the output. The signal conditioning stage is necessary to adapt the bipolar electrical variables (measured ac currents and voltages) to the unipolar [0,3] V range of the analog inputs of the DSP.

As an additional feature, a communication routine has been programmed in the DSP allowing the emulator to communicate with a remote monitoring PC through an Ethernet interface. A MATLAB graphic user interface (GUI) is implemented in the monitoring PC, which can be used to display measured variables such as voltages and currents, and to set parameters, such as the droop factor. The reprogramming of the DSP is not possible through the monitoring PC and it has to be done via the local PC connected through the JTAG interface. A schematic of the entire setup and the control strategy is shown in Fig. 4.2. Fig. 4.3 show pictures of the emulator implemented in laboratory. The abc/dq transformations used in the control are presented in Appendix C. The values of the power circuit parameters are presented in Table B.1 and Table B.2; the design of some of its components is also presented in Section B.2.1.
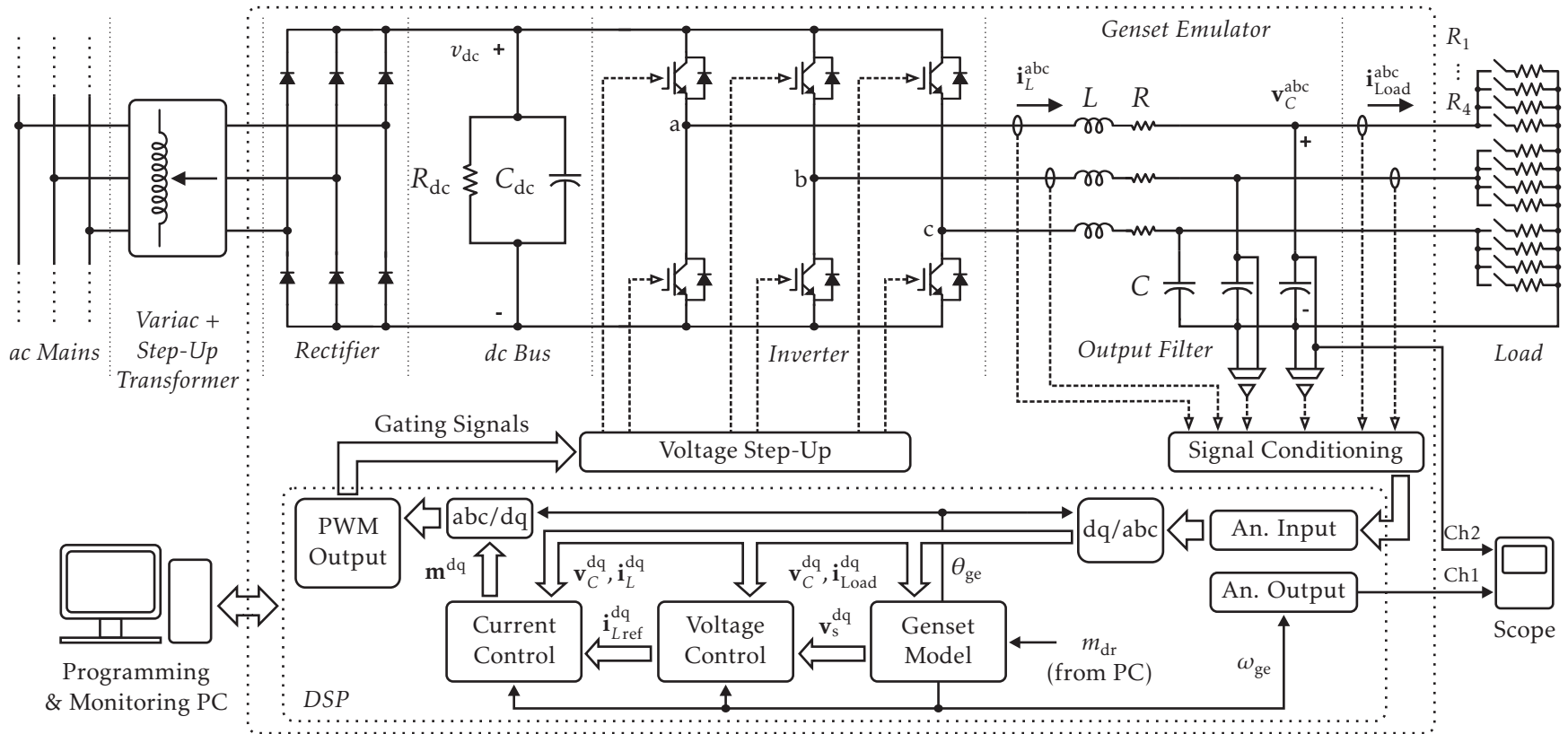
Figure 4.2: Schematic of the genset emulator.
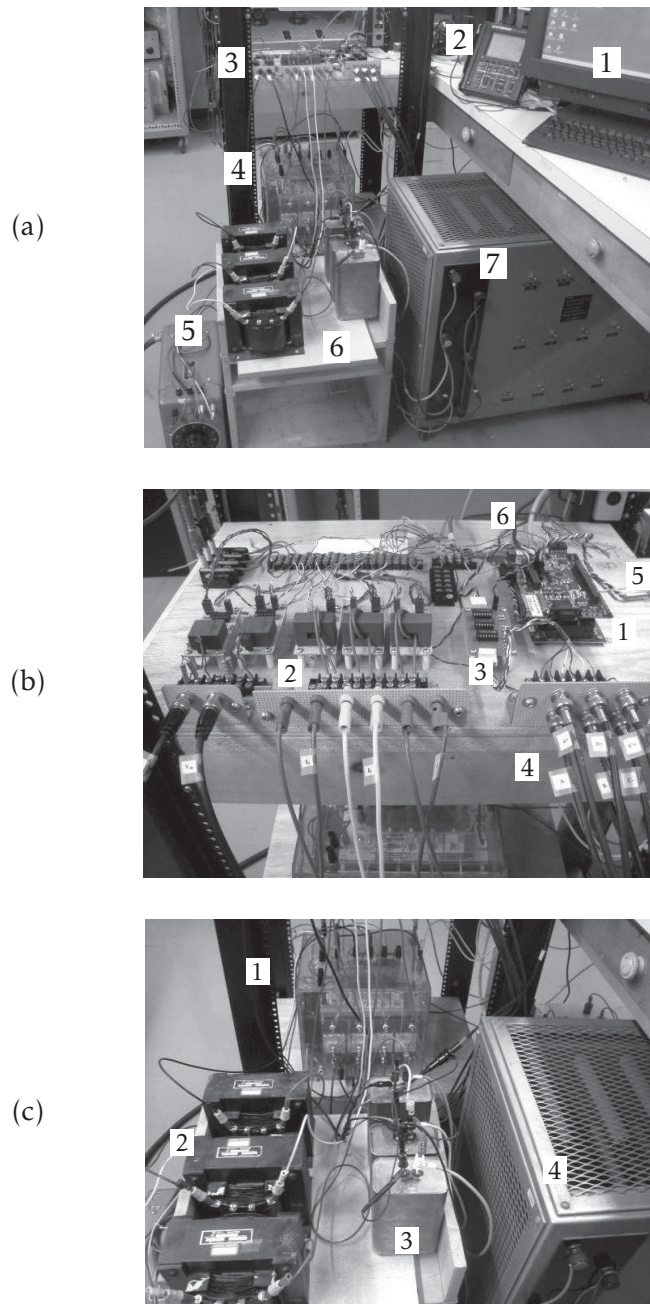
Figure 4.3: Experimental setup of the genset emulator.

(a) System overview, 1: Programming and monitoring PC, 2: Scope, 3: Control system, 4: Inverter, 5: Variac, 6: Output filter, 7: Load. (b) Control system, 1: DSP board, 2: Voltage and current sensors, 3: PWM voltage step up, 4: Gating signals, 5: analog outputs, 6: JTAG and Ethernet interfaces. (c) Power circuit, 1: Inverter, 2: Filter inductors, 3: Filter capacitors, 4: Load resistors bank.

4.3   CONTROL OF THE VOLTAGE SOURCE INVERTER

A control strategy in the dq reference frame is designed for the inverter so that its output voltages follow the references obtained from the genset model. To follow the voltage references with a desired performance, the currents of the inverter must also be controlled. The model of the converter used to design the controllers is the following [78]:

$$\frac{\mathrm{d}i_L^{\mathrm{d}}}{\mathrm{d}t} = -\frac{R}{L}i_L^{\mathrm{d}} + \omega_i i_L^{\mathrm{q}} - \frac{1}{L}v_C^{\mathrm{d}} + \frac{v_{\mathrm{dc}}}{L}m^{\mathrm{d}} \tag{4.1a}$$

$$\frac{\mathrm{d}i_L^{\mathrm{q}}}{\mathrm{d}t} = -\frac{R}{L}i_L^{\mathrm{q}} - \omega_i i_L^{\mathrm{d}} - \frac{1}{L}v_C^{\mathrm{q}} + \frac{v_{\mathrm{dc}}}{L}m^{\mathrm{q}} \tag{4.1b}$$

$$\frac{\mathrm{d}v_C^{\mathrm{d}}}{\mathrm{d}t} = \frac{1}{C}i_L^{\mathrm{d}} - \frac{1}{C}i_{\mathrm{Load}}^{\mathrm{d}} + \omega_i v_C^{\mathrm{q}} \tag{4.1c}$$

$$\frac{\mathrm{d}v_C^{\mathrm{q}}}{\mathrm{d}t} = \frac{1}{C}i_L^{\mathrm{q}} - \frac{1}{C}i_{\mathrm{Load}}^{\mathrm{q}} - \omega_i v_C^{\mathrm{d}} \tag{4.1d}$$

where R, L and C are the parameters of the ac filter, v_{dc} is the dc bus voltage, $i_{\mathrm{Load}}^{\mathrm{d}}$ and $i_{\mathrm{Load}}^{\mathrm{q}}$ are the load currents, i_L^{d} and i_L^{q} are the inductor currents, v_C^{d} and v_C^{q} are the capacitor voltages, and m^{d} and m^{q} are the control inputs. Note that ω_i, the fundamental frequency of the inverter output voltages, is imposed by the genset model generator speed as $\omega_i = n_{\mathrm{pp}}\omega_{\mathrm{ge}}$, where n_{pp} is the number of pole pairs of the electrical generator.

4.3.1 Current Control

The proposed control law is based on the input-output linearization method [79], which basically entails defining the modulation index as:

$$m^{\mathrm{d}} = \frac{1}{v_{\mathrm{dc}}}\left(Ri_L^{\mathrm{d}} - \omega_{\mathrm{i}}Li_L^{\mathrm{q}} + v_C^{\mathrm{d}} + Lu^{\mathrm{d}}\right) \tag{4.2}$$

so when it is replaced in (4.1a) all the non desired terms are eliminated, leading to the following equation:

$$\frac{\mathrm{d}i_L^{\mathrm{d}}}{\mathrm{d}t} = u^{\mathrm{d}} \tag{4.3}$$

where u^{d} becomes the new control input. Then, by defining the new input in the Laplace domain as:

$$u^{\mathrm{d}} = \left(i_{L\mathrm{ref}}^{\mathrm{d}} - i_L^{\mathrm{d}}\right)\frac{k_{1i}^{\mathrm{d}}}{s} - k_{2i}^{\mathrm{d}}i_L^{\mathrm{d}} \tag{4.4}$$

and replacing it in (4.3), the following second-order transfer function is obtained:

$$h_i^{\mathrm{d}}(s) = \frac{i_L^{\mathrm{d}}(s)}{i_{L\mathrm{ref}}^{\mathrm{d}}(s)} = \frac{k_{1i}^{\mathrm{d}}}{s^2 + k_{2i}^{\mathrm{d}}s + k_{1i}^{\mathrm{d}}} \tag{4.5}$$

The same procedure is applied to design the controller for the q axis current (4.1b) and both controllers are tuned with the same parameters.

4.3.2 Voltage Control

Given that the current loop will be designed to be sufficiently faster than the voltage loop, in the design of the voltage controllers it is assumed that the inductor current i_L^d is equal to its reference $i_{L\text{ref}}^d$. Then, applying the same control technique used to design the current controllers, $i_{L\text{ref}}^d$ s is defined as:

$$i_{L\text{ref}}^d = i_{\text{Load}}^d - \omega_i C v_C^q + C g^d \tag{4.6}$$

and then replaced in (4.1c) under the assumption $i_L^d = i_{L\text{ref}}^d$, resulting in the following equation:

$$\frac{dv_C^d}{dt} = g^d \tag{4.7}$$

where g^d becomes the new control input. Then, by defining the new input in the Laplace domain as:

$$g^d = \left(v_s^d - v_C^d\right)\frac{k_{1v}^d}{s} - k_{2v}^d v_C^d \tag{4.8}$$

and replacing it in (4.7), the following second-order transfer function is obtained:

$$h_v^d(s) = \frac{v_C^d(s)}{v_s^d(s)} = \frac{k_{iv}^d}{s^2 + k_{pv}^d s + k_{iv}^d} \tag{4.9}$$

The same procedure is applied to design the controller for the q axis voltage (4.1d) and both controllers are tuned with the same parameters.

The design of the four controllers (dq currents and voltages) is done by assigning values to the second-order standard parameters: damping ratio (ζ) and natural frequency (ω_n). The relations between the controller gains and the standard parameters ω_n and ζ are given by (B.2) and (B.3). First, a damping ratio of $\zeta = 0.8$ is set for all the controllers. Then, the natural frequency for the current loops is chosen to have a fast current response that is achievable by the setup. Finally, the natural frequency for the voltage loops is chosen to have a response five times slower than the current loops. The parameters of the control system are summarized in Table B.3.

4.4   DIGITAL IMPLEMENTATION

The linear models of the genset components (A.1), (A.2), (A.6), (A.7), and (A.8) are combined into a single model in the following state-space form:

$$\frac{\mathrm{d}\mathbf{x}_g}{\mathrm{d}t} = \mathbf{A}_g\mathbf{x}_g + \mathbf{b}_g u_g \tag{4.10a}$$

$$\mathbf{y}_g = \mathbf{C}_g\mathbf{x}_g + \mathbf{d}_g u_g \tag{4.10b}$$

where the state vector is defined as $\mathbf{x}_g = [i_s^d\ i_s^q\ i_f\ i_k^d\ i_k^q\ \omega_{en}\ \omega_{ge}\ \tau_{ss}\ \tau_m\ z_\omega\ v_f\ z_v]^T$, the input as $u_g = R_l$ and the outputs as $\mathbf{y}_g = [v_s^d\ v_s^q\ \omega_{ge}]^T$. The matrices of the system are defined in Section B.1. To solve system (4.10) in the DSP, the matrices and vectors $\mathbf{A}_g$, $\mathbf{b}_g$, $\mathbf{C}_g$ and $\mathbf{d}_g$ are converted to their discrete-time equivalent considering a sampling time of $100\,\mu s$, which is the execution time of the DSP control task. The conversion is done in MATLAB with the function "c2d". After the conversion,

system (4.10) can be written in its discrete-time form as:

$$\mathbf{x}_g(k+1) = \mathbf{A}'_g \mathbf{x}_g(k) + \mathbf{b}'_g u_g(k) \tag{4.11a}$$

$$\mathbf{y}_g(k) = \mathbf{C}'_g \mathbf{x}_g(k) + \mathbf{d}'_g u_g(k) \tag{4.11b}$$

where the symbol $'$ denotes the discrete-time converted matrix or vector, and the variable k represents the current sampling time.

Now, the genset model (4.11) can be directly programmed into the control task of the DSP. Note that matrices and vectors of model (4.11) need to be calculated beforehand, which restricts the emulator to accept only predefined variations of its parameters during operation. Therefore, in order to test the emulator for different values of speed droop, the elements of matrix $\mathbf{A}'_g$ that are affected by the droop factor (rows 9 and 10) must be calculated for the desired values of k_{dr} in advance. Then, during the execution of the model, the program uses the appropriate elements according to the actual value of droop. Note that the droop factor can be changed by the user at any time during the operation of the emulator.

The input of model (4.11), which is defined as the resistance of the load, it is not directly measured from the setup then its value is calculated as:

$$R_l = \frac{\|\mathbf{v}_C^{dq}\|}{\|\mathbf{i}_{Load}^{dq}\|} \tag{4.12}$$

where $\mathbf{v}_C^{dq}$ and i_{Load}^d are the load voltages and currents.

4.5   PERFORMANCE EVALUATION

Two types of tests were conducted to evaluate the performance of the emulator at different values of speed droop: one test for the steady-state response and another test for the transient response. In all the tests, channel one (Ch1) of the scope recorded the analog output of the DSP that was assigned to the (internal model) generator speed ω_{ge} and channel two (Ch2) of the scope was used to record the output voltage of phase a, v_C^a.

4.5.1   Steady-State Response

This test was performed to verify the steady-state frequency droop of the emulator for three different values of droop: 0 %, 3 % and 5 %. For each value of droop the equivalent resistance was decreased—or the load was increased—in seven steps from an equivalent resistance per phase of 50 Ω to 22.7 Ω. On each step the variables of interest were recorded once the system reached steady-state. Table B.2 summarizes the equivalent resistance and the corresponding combination of resistors from the bank for each step. The starting load of 50 Ω was chosen to start with a current greater than the minimum for which the output filter of the inverter was designed.

Fig. 4.4(a) shows the data recorded from channel 1 for 0 % droop, where practically no variation in steady-state is observed. On the other hand, Fig. 4.4(b) and Fig. 4.4(c) show the data recorded for 3 % and 5 % droop respectively, where it is observed that a speed variation occurred due to the droop factors. The data recorded from these tests is compared with the theoretical droop curves and the
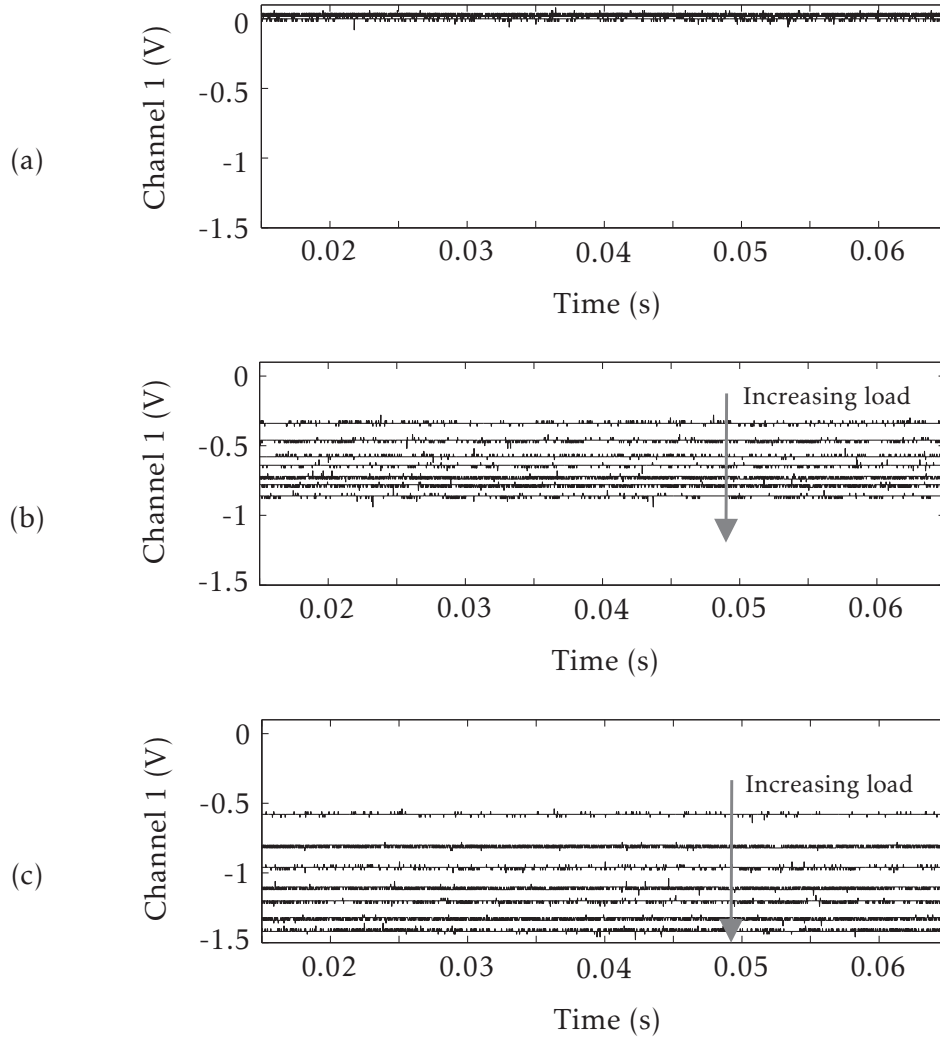
Figure 4.4: Steady-state response of the emulator for different values of droop.
Ch1: Generator speed. (a) 0% speed droop. (b) 3% speed droop. (c) 5% speed droop.

frequency readings from the scope in Fig. 4.5. From this figure it can be seen that

the droop characteristics of the internal model, as well as the frequency readings

from the scope, are very close to the theoretical droop curves. In fact, the average

error between the internal model and the theoretical droop curves is relatively low

and in the same order of magnitude than the error in the actual frequencies indi-

cated by the scope ($\sim 0.1\%$). All the calculated errors are summarized in Table B.4.
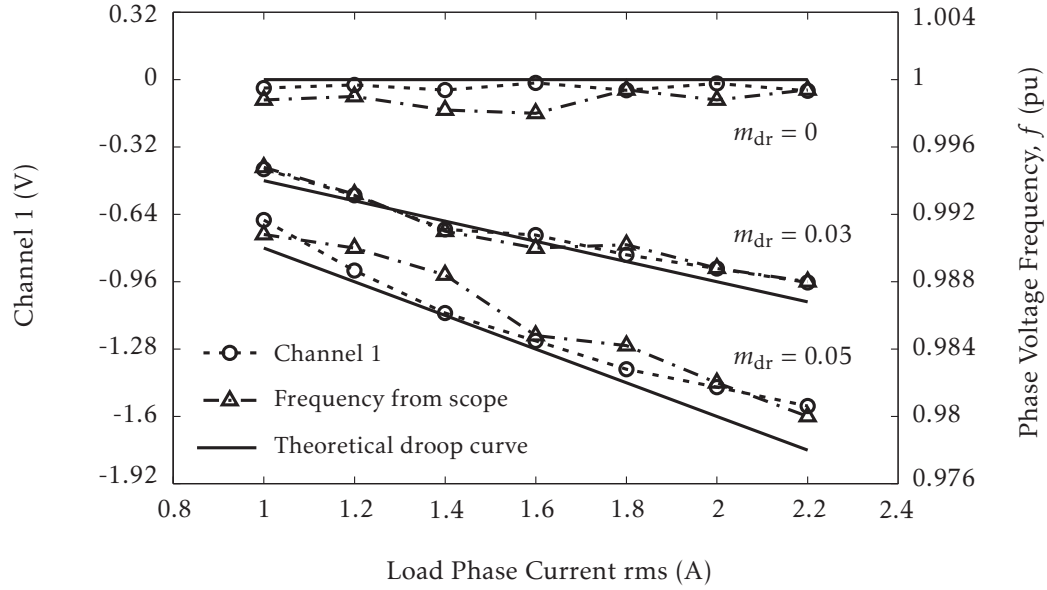
Figure 4.5: Steady-state response of the emulator for different values of droop.
Experimental and theoretical static droop curves.

4.5.2 Transient Response

This test was performed to verify the transient response of the emulator for three different values of droop: 0 %, 3 % and 5 %. For each value of droop the equivalent resistance was decreased—or the load was increased—from step 4 to step 6 by connecting R_4 in the three phases at the same time (see Table B.2). This change in the resistance produced an equivalent 50 % load increase for the internal model. In order to record the transient response, the scope was set to be triggered by a negative slope of channel 1. Fig. 4.6 shows the data recorded from these tests, where it can be seen the difference in the transient responses due to the speed droop. Then, the above test was repeated, but this time a value close to the nadir* was used to trigger the scope. By doing this, it was possible to know the value of the actual frequency at the nadir of the waveforms presented in Fig. 4.6.

---

*Lowest value of the frequency during a transient [80].
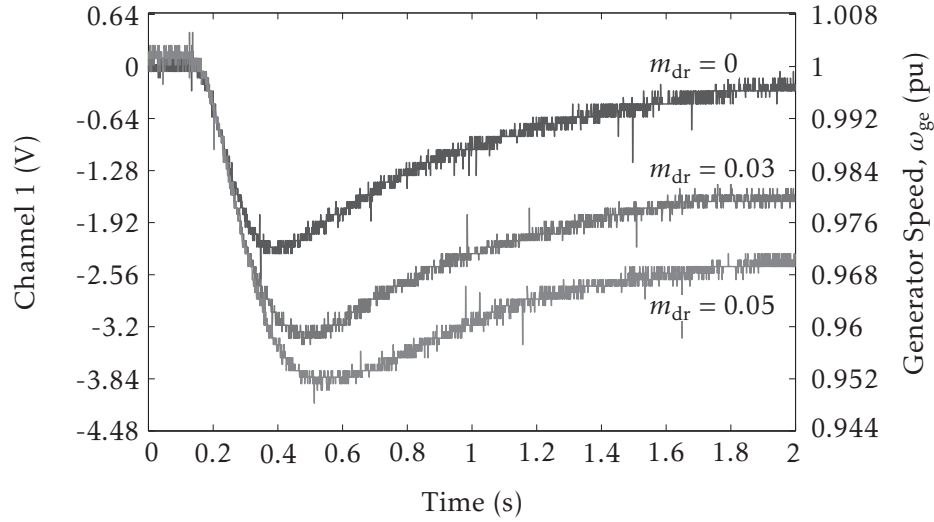
Figure 4.6: Transient response of the emulator for different values of droop.

Fig. 4.7(a) shows a screen capture of the scope for 0 % droop, where the speed nadir has a value of -2.124 V and the scope indicates a minimum frequency of 48.6 Hz. Fig. 4.7(b) shows a screen capture of the scope for 3 % droop, where the speed nadir has a value of -3.244 V and the scope indicates a minimum frequency of 48.12 Hz. Fig. 4.7(c) shows a screen capture of the scope for 5 % droop, where the speed nadir has a value of -3.859 V and the scope indicates a minimum frequency of 47.85 Hz. To compare these results with the simulated ones presented in Chapter 2, the values from channel 1, which are in Volts, were converted to pu using the scale obtained from the steady-state tests (0.0125 pu/V). On the other hand, the values of frequency obtained from the scope, which are in Hertz, were converted dividing by the nominal frequency (50 Hz). From the calculated errors, shown in Table B.5, it can be noted that the errors of the internal model are slightly higher than the errors in the frequencies indicated by the scope. However the average of all the errors is close to 0.17 % which is relatively low and consistent with

the average of the errors calculated in the steady-state tests.
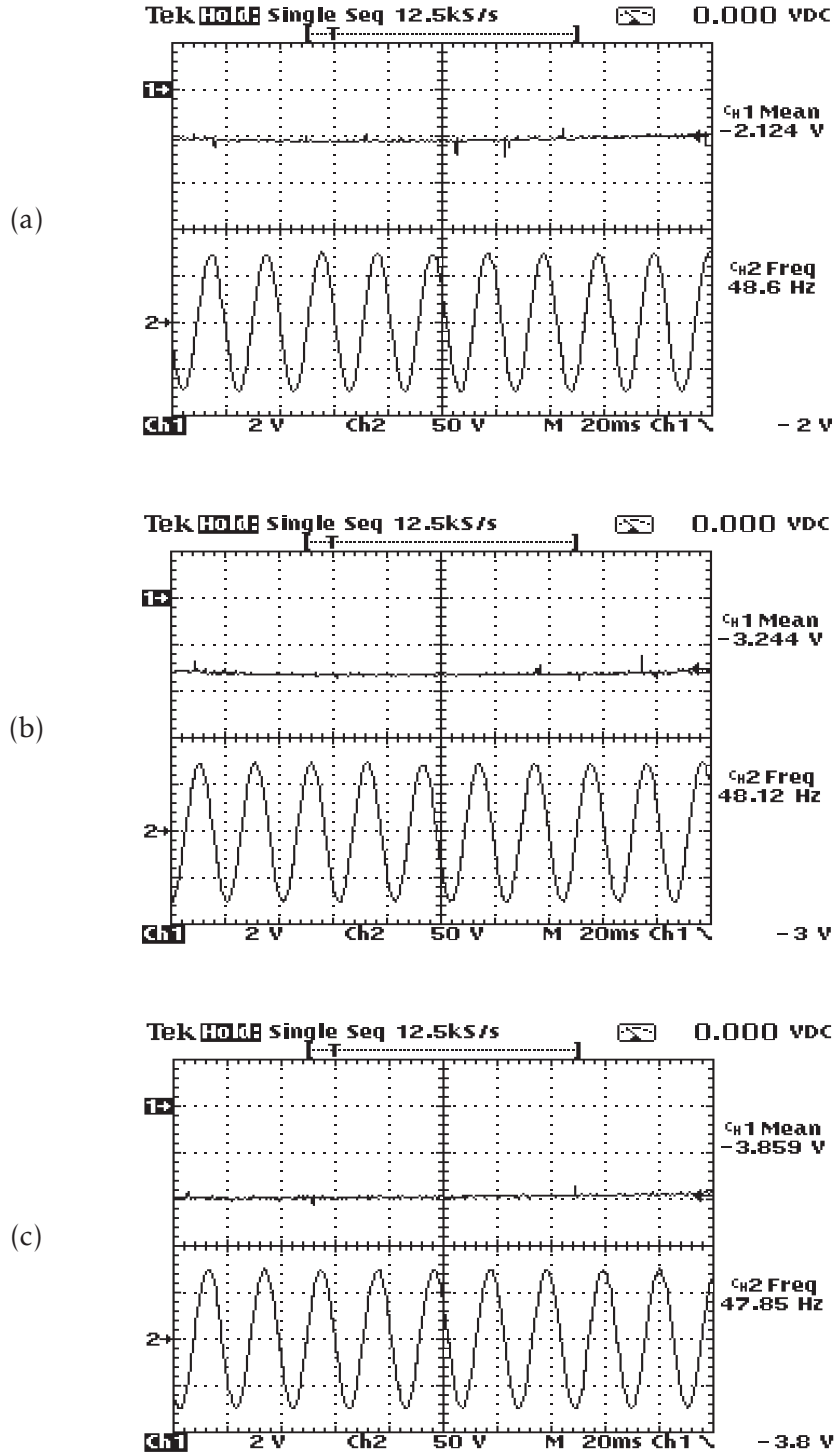
Figure 4.7: Measurement of the frequency nadir for different values of droop.

Ch1: Generator speed, Ch2: Phase voltage. (a) 0% speed droop. (b) 3% speed droop. (c) 5% speed droop.

4.6 DISCUSSION AND CONCLUSIONS

In this Chapter the implementation of an inverter-based diesel generator emulator has been presented. The main purpose of this emulator is the study of frequency variations in diesel-hybrid autonomous power systems in a laboratory setting, where the operation of a real genset is unfeasible. The emulator consists in a voltage-controlled inverter, where the voltage references are calculated from the genset model which is executed in real-time in a DSP.

Experimental tests were performed to verify the steady-state and transient response of the emulator for three different values of speed droop: 0 %, 3 % and 5 %. For the steady-state response, the measured frequencies deviated from theoretical values with an average error of 0.124 %; for the transient response, the measured frequency nadirs deviated from simulations with an average error of 0.139 %. These results showed that the emulator achieved a satisfactory performance in representing the output frequency of a diesel generator.

CHAPTER 5

VIRTUAL SYNCHRONOUS MACHINE

5.1 INTRODUCTION

A VSM entails the control of the grid-interface converter of a distributed generator or ESS in order to emulate a synchronous generator or a desired characteristic of it. Different realizations of the VSM can be developed depending on the application. In this particular case, the VSM is implemented on the ESS and the strategy proposed to support dynamic frequency control involves emulating the inertial response and the damping power of a synchronous generator, which are present only during a transient.

Fig. 5.1 illustrates the concept of the VSM used in this thesis. The grid frequency is locally measured at the point where the ESS is connected and then, based on the measured frequency, the output power of the VSM is calculated, which turns out to be the reference for the output active power of the ESS. In order to control the ESS as a VSM, it is necessary to have a decoupled control over
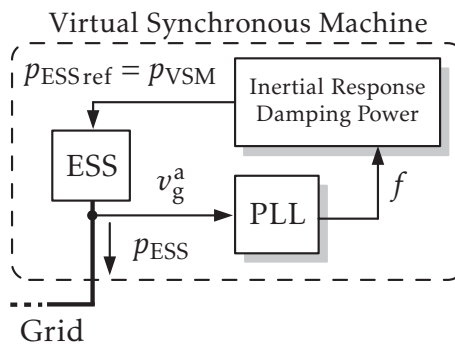
Figure 5.1: Block diagram of the VSM control.

the active and reactive power of the grid side converter. Such a control strategy is presented in the next section.

5.2   CONTROL OF THE GRID SIDE CONVERTER

As mentioned in the introductory Chapter, a voltage source converter (VSC) is considered as the ESS interface to the grid, because it can provide fast and accurate bidirectional power control, which is a desired property regarding short-term active power compensation. Fig. 5.2 shows the schematic of the topology and a block diagram of the control strategy. The dq model of this topology is the following:

$$\frac{\mathrm{d}i_{\mathrm{ESS}}^{\mathrm{d}}}{\mathrm{d}t} = -\frac{R}{L}i_{L}^{\mathrm{d}} + \omega i_{\mathrm{ESS}}^{\mathrm{q}} - \frac{1}{L}v_{\mathrm{g}}^{\mathrm{d}} + \frac{v_{\mathrm{dc}}}{L}m^{\mathrm{d}} \tag{5.1a}$$

$$\frac{\mathrm{d}i_{\mathrm{ESS}}^{\mathrm{q}}}{\mathrm{d}t} = -\frac{R}{L}i_{\mathrm{ESS}}^{\mathrm{q}} - \omega i_{\mathrm{ESS}}^{\mathrm{d}} - \frac{1}{L}v_{\mathrm{g}}^{\mathrm{q}} + \frac{v_{\mathrm{dc}}}{L}m^{\mathrm{q}} \tag{5.1b}$$

where R and L are the parameters of the ac filter, v_{dc} is the dc bus voltage, $i_{\mathrm{ESS}}^{\mathrm{d}}$ and $i_{\mathrm{ESS}}^{\mathrm{q}}$ are the inductor currents, m^{d} and m^{q} are the control inputs, $v_{\mathrm{g}}^{\mathrm{d}}$ and $v_{\mathrm{g}}^{\mathrm{q}}$ are the grid voltages, and ω is the fundamental frequency of the grid. In this model the active and reactive powers calculated at the output of the inverter, p_{ESS} and q_{ESS} respectively, are defined as:

$$p_{\mathrm{ESS}} = \mathbf{v}_{\mathrm{g}}^{\mathrm{dq}} \cdot \mathbf{i}_{\mathrm{ESS}}^{\mathrm{dq}} = v_{\mathrm{g}}^{\mathrm{d}}i_{\mathrm{ESS}}^{\mathrm{d}} + v_{\mathrm{g}}^{\mathrm{q}}i_{\mathrm{ESS}}^{\mathrm{q}} \tag{5.2}$$

$$q_{\mathrm{ESS}} = \mathbf{v}_{\mathrm{g}}^{\mathrm{dq}} \times \mathbf{i}_{\mathrm{ESS}}^{\mathrm{dq}} = v_{\mathrm{g}}^{\mathrm{d}}i_{\mathrm{ESS}}^{\mathrm{q}} - v_{\mathrm{g}}^{\mathrm{q}}i_{\mathrm{ESS}}^{\mathrm{d}} \tag{5.3}$$
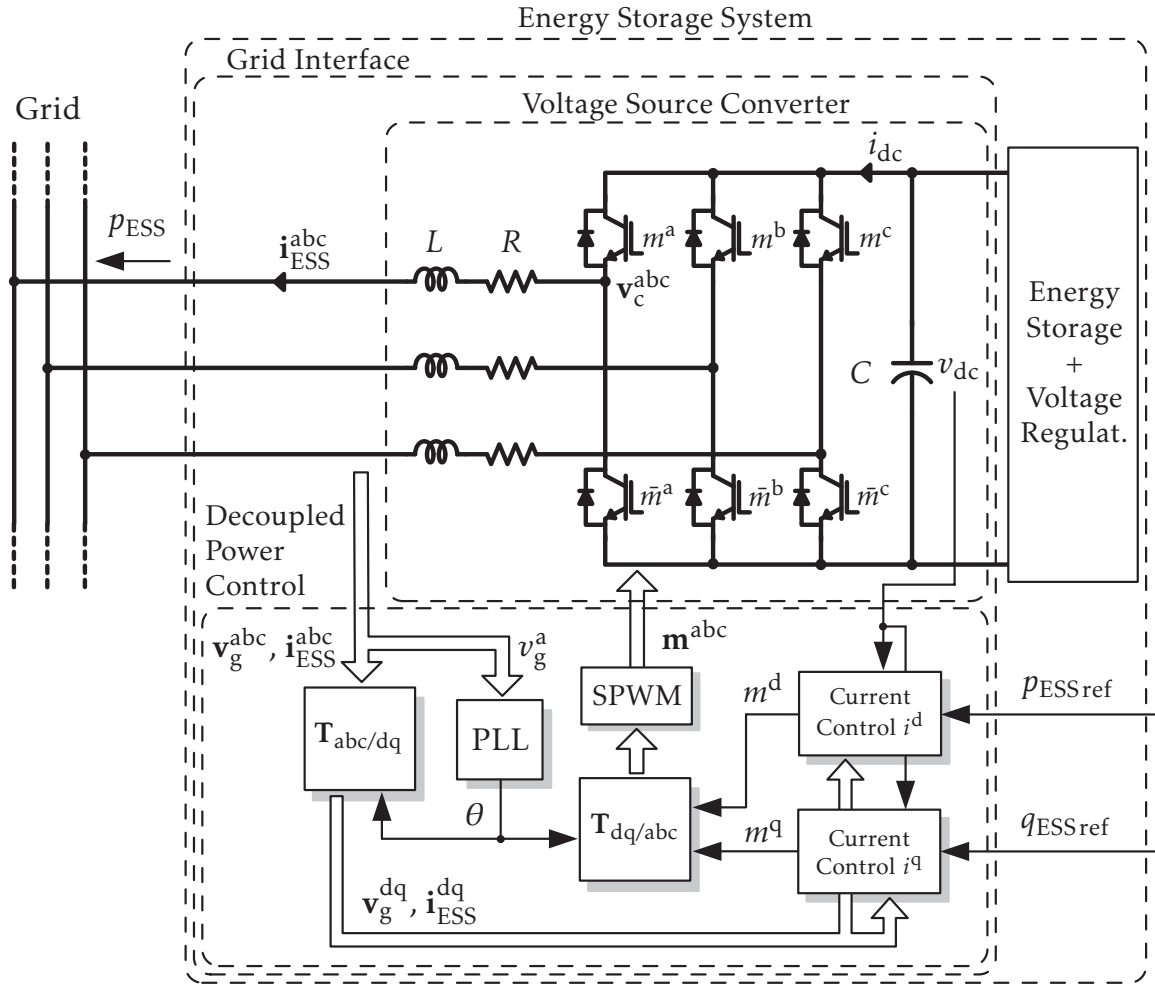
Figure 5.2: Decoupled current control of a VSC.

If the inverter is perfectly synchronized[*] with the grid voltages, and a balanced grid is assumed, then (according to (C.3)) it follows that $v_g^q = 0$ and the above equations are simplified to:

$$p_{ESS} = v_g^d i_{ESS}^d \tag{5.4}$$

---

[*]A converter that is controlled in the dq reference frame it is said to be synchronized with the grid when its dq reference frame rotates with the same frequency and in phase with one of the grid voltages.

$$q_{\text{ESS}} = v_g^d i_{\text{ESS}}^q \tag{5.5}$$

It is observed that the active and reactive powers can be indirectly con-

trolled by the dq currents. Because the dq model of the VSC presents nonlineari-

ties and coupling between the d and q axes, the control of the currents is divided

in two steps. First, the linearization and decoupling of the model is presented,

then, linear controllers are design for each current independently.

5.2.1 Input-Output Linearization

Basically, the input-output linearization method [79] allows the canceling

of the nonlinearities of the VSC model and the decoupling (at least in steady-state)

of the d and q axes. The modulation indexes, m^d and m^q, are defined as:

$$m^d = \frac{1}{v_{\text{dc}}} \left(R i_{\text{ESS}}^d - \omega L i_{\text{ESS}}^q + v_g^d + L u^d \right) \tag{5.6}$$

$$m^q = \frac{1}{v_{\text{dc}}} \left(R i_{\text{ESS}}^q + \omega L i_{\text{ESS}}^d + v_g^q + L u^q \right) \tag{5.7}$$

Then, by replacing the above defined modulation indexes in the VSC model (5.1)

the following linear equations for the dq currents are obtained:

$$\frac{d i_{\text{ESS}}^d}{dt} = u^d \tag{5.8}$$

$$\frac{d i_{\text{ESS}}^q}{dt} = u^q \tag{5.9}$$

where u^d and u^q are the new control inputs.

5.2.2 q-axis Current Control

The purpose of controlling the q-axis current is to control the reactive power flow through the ESS. The requirement is to regulate the reactive power to a certain level, therefore a controller with zero error in steady-state for a step reference is appropriate.

By defining the new control input u^q in the s-domain as:

$$u^q = \frac{k_{ii}^q}{s} \left(i_{ESS\,ref}^q - i_{ESS}^q \right) - k_{pi}^q i_{ESS}^q \tag{5.10}$$

and replacing it in (5.9), the following second order transfer function is obtained:

$$\frac{i_{ESS}^q(s)}{i_{ESS\,ref}^q(s)} = \frac{k_{ii}^q}{s^2 + k_{pi}^q s + k_{ii}^q} \tag{5.11}$$

The parameters of this transfer function are associated to the ones of a standard second order transfer function as $k_{ii}^q = \omega_n^2$ and $k_{pi}^q = 2\zeta\omega_n$, where ω_n is the natural frequency of oscillation and ζ is the damping ratio. Parameters have been selected in order to reach a step reference in less than a half grid cycle with an overshoot of less than 5 %. Controller parameters are shown in Table D.1.

5.2.3 d-axis Current Control

The purpose of controlling the d-axis current is to control the active power flow through the ESS, which in turn is dictated by the VSM control strategy, as shown in Fig. 5.1. Because of the latter, the d-axis current will be required to follow

a reference that might present fast variations during short periods of time. There-

fore, a controller that achieves zero error in steady-state for a ramp and quadratic

reference is proposed as a solution. The controller is defined in the s-domain as:

$$u^d = \left\{ k_{pi}^d + \frac{k_{ii}^d}{s} + \frac{1}{s^2} \right\} \left(i_{ESS\,ref}^d - i_{ESS}^d \right) \tag{5.12}$$

and replacing it in (5.8), the following transfer function is obtained:

$$\frac{i_{ESS}^d(s)}{i_{ESS\,ref}^d(s)} = \frac{k_{pi}^d s^2 + k_{ii}^d s + 1}{s^3 + k_{pi}^d s^2 + k_{ii}^d s + 1} \tag{5.13}$$

Unlike the transfer function previously obtained for the q-axis current,

transfer function (5.13) does not correspond to a standard second order system,

thus its parameters cannot be designed by assigning a damping ratio and a natural

frequency to the system. Therefore, the values for the parameters of (5.13) were

found by manual tuning (starting with the values previously found for the q-axis

controller) until a satisfactory response to a step input was achieved. As it will be

shown in the next section, the d-axis current was able to reach a step reference in

less than a half grid cycle with an overshoot of less than 5 %, and it was also able

to follow a ramp and quadratic references with sufficiently fast convergence rates.

The design of the controllers has been done using the dq model of the

VSC, which allows the use of the classical control theory, but it does not consider

the effects of the commutation of switches and associated harmonics. Therefore,

simulations with the dq model and PWM model of the converter are conducted

to verify the performance of the decoupled power control. The simulation entails different changes in the VSC current references while the VSC is connected to a three-phase voltage source with constant and balanced voltage amplitudes and constant frequency. Parameters of the controllers and power circuit used in simulations can be found in Table D.1 and Table D.2 respectively. Simulated waveforms are presented in Section D.1.2, which show that the desired behavior is achieved.

5.3   INERTIAL RESPONSE

The inertial response emulates the power that is naturally released or absorbed by a conventional rotating generator as the power demand varies and before its governor reacts. The main effects of the inertial response over the system frequency are: limiting the rate of change and the maximum deviation following a power disturbance. The power supplied due to the inertial response of the VSM is defined as:

$$p_{\text{VSM}} = -k_{\text{vi}}\omega_{\text{eq}}\frac{\mathrm{d}\omega_{\text{eq}}}{\mathrm{d}t} \tag{5.14}$$

where k_{vi} represents the virtual inertia. To illustrate how the virtual inertia is added to the system, consider the diagram of Fig. 5.3, where the loads are represented by a net power flow, p_{Load}, and the genset supplies the electrical power $p_{\text{DG1}} = p_{\text{Load}} - p_{\text{ESS}}$. Rewriting the equivalent shaft model of a single genset (3.1)
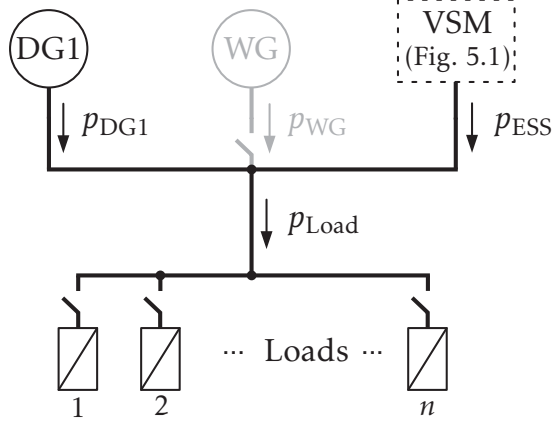
Figure 5.3: Autonomous power system with VSM.

in terms of power variables gives:

$$J_{eq}\frac{d\omega_{eq}}{dt} = -k_{feq}\omega_{eq} + \frac{p_m - p_{Load} + p_{ESS}}{\omega_{eq}} \tag{5.15}$$

Then, assuming that the output power of the ESS is equal to its reference (5.14) and replacing it in (5.15), the following equation is obtained:

$$\left(J_{eq} + k_{vi}\right)\frac{d\omega_{eq}}{dt} = -k_{feq}\omega_{eq} + \frac{p_m - p_{Load}}{\omega_{eq}} \tag{5.16}$$

from where it is clear that the coefficient k_{vi} represents a virtual inertia.

Now, considering that:

i)   Electrical frequency is closely related to the rotational speed of the genset

ii)   Electrical frequency can be measured at the point of connection of the ESS

then, it would be more practical to utilize the grid frequency, which is measured in the synchronization routine presented in Section D.2, to calculate the inertial power (5.14) instead of the rotational speed of the genset ω_{eq}. Therefore, the iner-

tial component can be calculated in terms of the grid frequency as:

$$p_{\text{VSM}} = -k_{\text{vi}}k_{\text{r}}^2 f \frac{\mathrm{d}f}{\mathrm{d}t} \tag{5.17}$$

where $k_{\text{r}} = 4\pi/n_{\text{p}}$ is a constant that relates the electrical frequency with the ro-
tational speed of the genset, and n_{p} is the number of poles of the synchronous
generator.

5.3.1 Calculation of the Derivative

The first derivative of the grid frequency required for (5.17) can be calcu-
lated as the first-order difference:

$$\frac{\mathrm{d}f}{\mathrm{d}t}(k) = \frac{f(k) - f(k-1)}{T_{\text{ctr}}} \tag{5.18}$$

where T_{ctr} is the sampling time (the period of the timer assigned to the control rou-
tine) and k is the integer that represents the current sampling time. However, due
to the presence of noise, it is a common practice to implement a filtered derivative
[81] which can be calculated as:

$$\frac{\mathrm{d}f}{\mathrm{d}t}(k) = \frac{f(k) - f(k-1) + T_{\text{f}}\frac{\mathrm{d}f}{\mathrm{d}t}(k-1)}{T_{\text{ctr}} + T_{\text{f}}} \tag{5.19}$$

where T_{f} is the time constant of the filter. A simulation is conducted to com-
pare both calculation methods. The test consists in a load increase of $5\,\text{kW}$ at
$t = 1\,\text{s}$ while only one genset (DG1) is connected to the system and it operates in

isochronous mode. The system starts in steady state with an initial load of 20 kW.

Fig. 5.4 shows simulation results for the calculated frequency derivatives. It can

be observed that the filtered derivative eliminates the oscillations that are present

in the non-filtered derivative (specially during the initial part of the transient),

however it adds a delay of approximately 50 ms to the calculation of the deriva-

tive, which is close to the time constant used for the filter (T_f = 60 ms). Then,

using the filtered derivative and with the VSM connected to the grid, the simu-

lation test is repeated (The values of k_{vi} = 2 and k_{vd} = 0 come from the analysis

of the transient response presented in Chapter 3). Fig. 5.5 shows the simulation

results, where it can be observed that the inertial response of the VSM reduced

the frequency nadir in approximately 35 % and increased the peak time (reduced

the initial rate of change) in approximately 70 %, in comparison to the original

response of the system (without VSM).
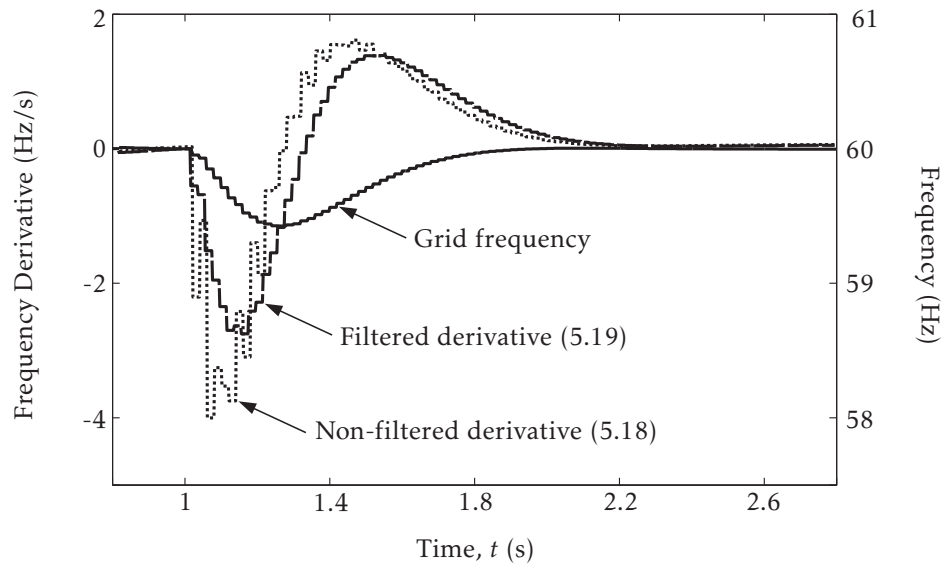
Figure 5.4: Simulated waveforms of the frequency derivative.

Simulated waveforms for a sampling time of T_{ctr} = 20 ms and a filter time constant of
T_f = 60 ms.

(a)

(b)
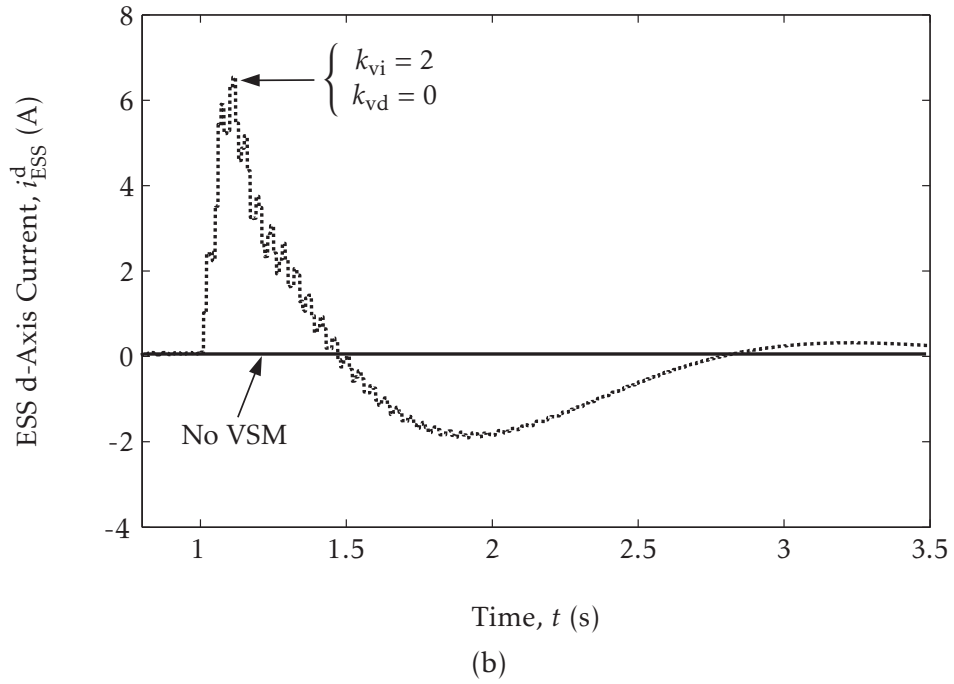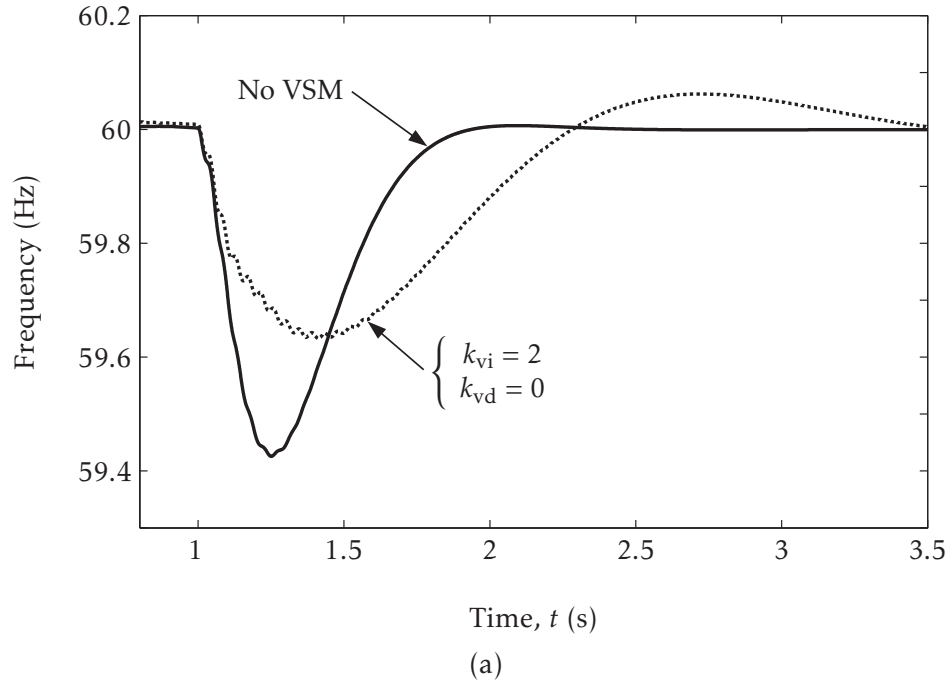
Figure 5.5: Simulation of the inertial response.

(a) Frequency waveforms. (b) ESS d-axis output current waveforms.

5.3.2 Experimental Results

The schematic of the experimental setup is depicted in Fig. D.9. The genset emulator presented in **Chapter 4** is used to represent the diesel generator DG1 of **Fig. 5.3** and the loads are represented by a bank of resistors.

In the first test, the calculation of the filtered derivative is evaluated (the VSM is disconnected from the grid). The genset operates in isochronous mode and a step-like load increased is produced with the bank of resistors, while DSP-2 is used to calculate the filtered derivative (5.19). Fig. 5.6 show the experimental waveforms where it can be observed that the derivative calculated in DSP-2 has a delay of approximately 120 ms with respect to the speed of the generator (which is a signal of the genset model generated in DSP-1). This delay is acceptable considering that the sampling time of the derivative calculation routine is 20 ms and
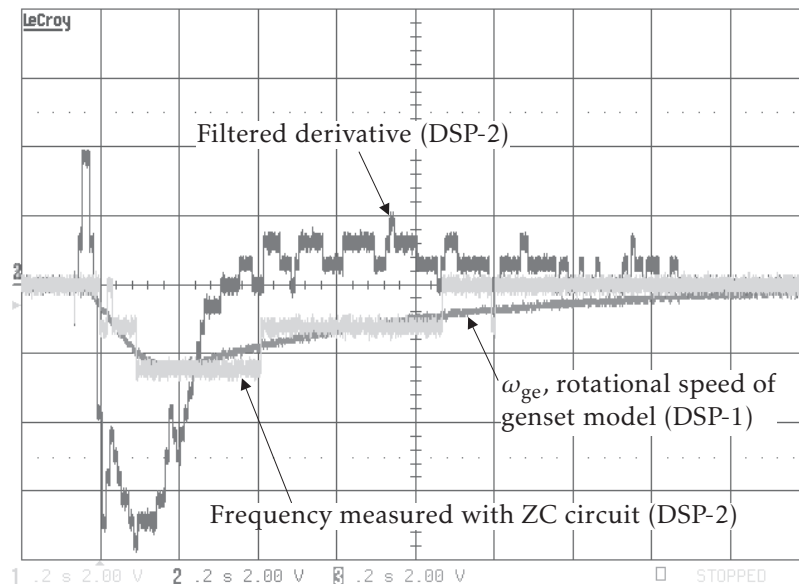
Figure 5.6: Experimental waveforms of the frequency derivative.

Results obtained with a sampling time of $T_{ctr} = 20$ ms and a filter time constant of $T_f = 100$ ms.

the filter used has a time constant of 100 ms. It is also observed that, compared to the simulation test, a larger time constant for the filter was required in the experimental test.

A second test is performed to evaluate the emulation of virtual inertia. The VSM is implemented with a second inverter which is controlled by DSP-2. Since only the virtual inertia function is evaluated, the reference for the reactive power is set to zero and the reference for the active power is given by (5.17) using the filtered derivative (5.19). The genset operates in isochronous mode and a step-like load increased is produced with the bank of resistors. Fig. 5.7 show the experimental waveforms where Fig. 5.7(a) shows the system frequency variation without the VSM and Fig. 5.7(b) shows the frequency variation with the inertial response of the VSM. It is observed that the inertial response of the VSM reduced the frequency nadir in approximately 35 % and increased the peak time (reduced the initial rate of change) in approximately 100 %.
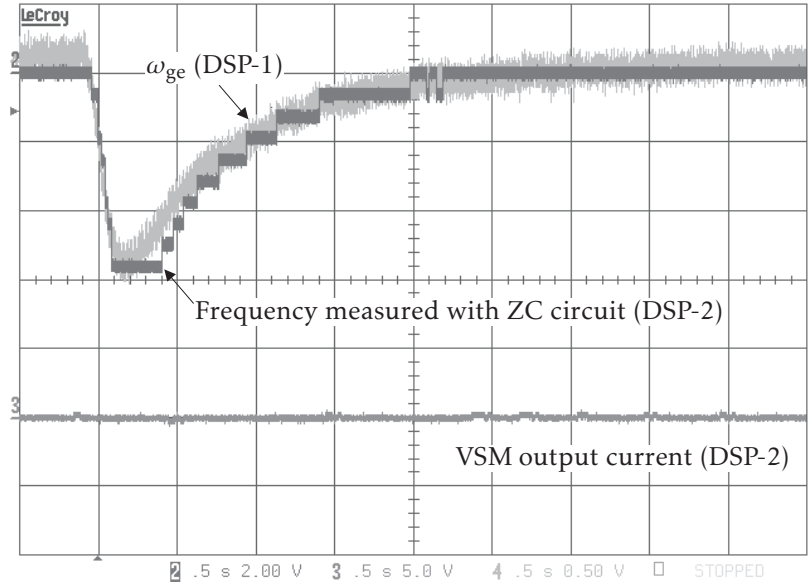
(a)
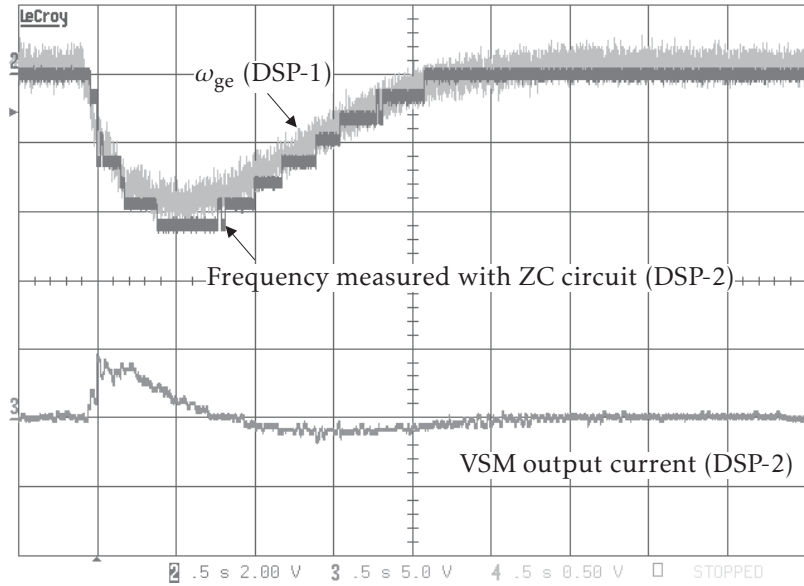
(b)

Figure 5.7: Experimental waveforms of the inertial response.

(a) Original response of the system without VSM. (b) Frequency deviation with inertial response added by VSM.

5.4 DAMPING POWER

The damping power is the power supplied by the virtual prime mover that helps to attenuate oscillations and then reduce the stabilization time for a predefined tolerance band. The damping power of the VSM is defined as:

$$p_{\text{VSM}} = k_{\text{vd}} k_{\text{r}}^2 f \left(f^* - f \right) \tag{5.20}$$

where k_{vd} is the damping coefficient and f^* is the stabilization frequency that the system is supposed to reach in steady-state. Any deviation from the reference frequency produces a power that attempts to bring back the grid frequency to the reference, attenuating the amplitude of the oscillations [50]. One of the main assumptions in the calculation of the damping power as defined in (5.20) is that the reference frequency (f^*) is known. In the case of a system that operates with isochronous primary frequency control, f^* should be the nominal frequency of the system (e.g. 60 Hz) and, therefore, it is known a priori. However, this might not be the case of a mini-grid that operates in droop mode, where the frequency of the grid changes with the load level.

To illustrate this problem, a simulation is performed with the system of Fig. 5.3 to compare the performance of the VSM (only damping function (5.20) with $k_{\text{vd}} = 10$) in two scenarios: when DG1 operates in isochronous mode at a nominal frequency of 60 Hz and when DG1 operates with 6 % frequency droop. In both cases the genset starts in 60 Hz with no load and the load is increased by 5 kW at $t = 5$ s. Also, the nominal frequency of 60 Hz is used in both cases as the

stabilization frequency to compute the damping power (5.20) (as discussed before, it is assumed that the actual stabilization frequency during droop operation is not available for the VSM because it is an internal variable of the genset governor). Fig. 5.8(a) shows the frequency waveforms and Fig. 5.8(b) shows the output active power of the ESS. It can be seen that in the case of isochronous operation the output power of the ESS goes to zero as the grid frequency returns to 60 Hz after the transient.

In the case of droop operation, due to the assumption $f^* = 60\,\text{Hz}$ a miscalculation of the damping term occurs, which produces an output power of 2.2 kW

(a)

(b)
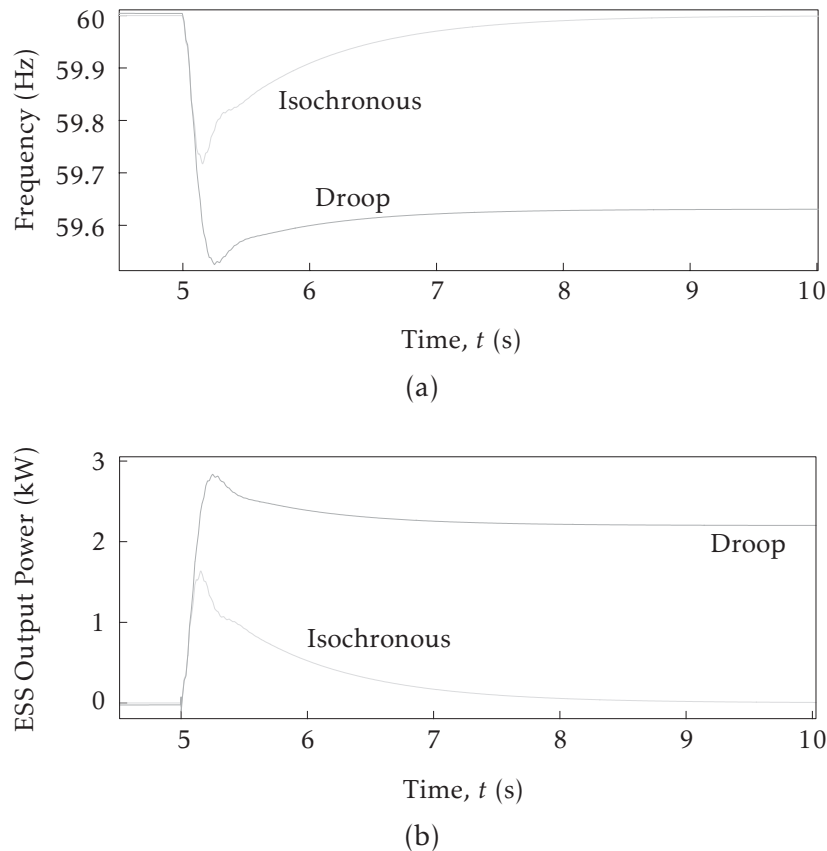
Figure 5.8: Simulation of the VSM without stabilization frequency estimator.
(a) Grid frequency. (b) ESS output active power.

for the ESS in steady-state. This continuous output power is considered an unde-
sired behavior of the VSM, whose purpose is to assist frequency control only dur-
ing the transient. Therefore, in order to inject damping power under frequency
droop mode, the reference frequency (f^*) in (5.20) should follow the stabilization
frequency of the grid instead of being a fixed value. In the next section, an estima-
tor of the stabilization frequency is proposed as a solution to provide the reference
frequency for the damping function of the VSM.

5.4.1 Open-Loop Estimator

The proposed estimator is defined as a proportional integral (PI) con-
troller with droop factor, based on the assumption (or prior knowledge) that
the genset governor has the same structure (as the speed governor presented in
Chapter 2). The block diagram of the estimator is depicted in Fig. 5.9, where $\tilde{f}^*$ is
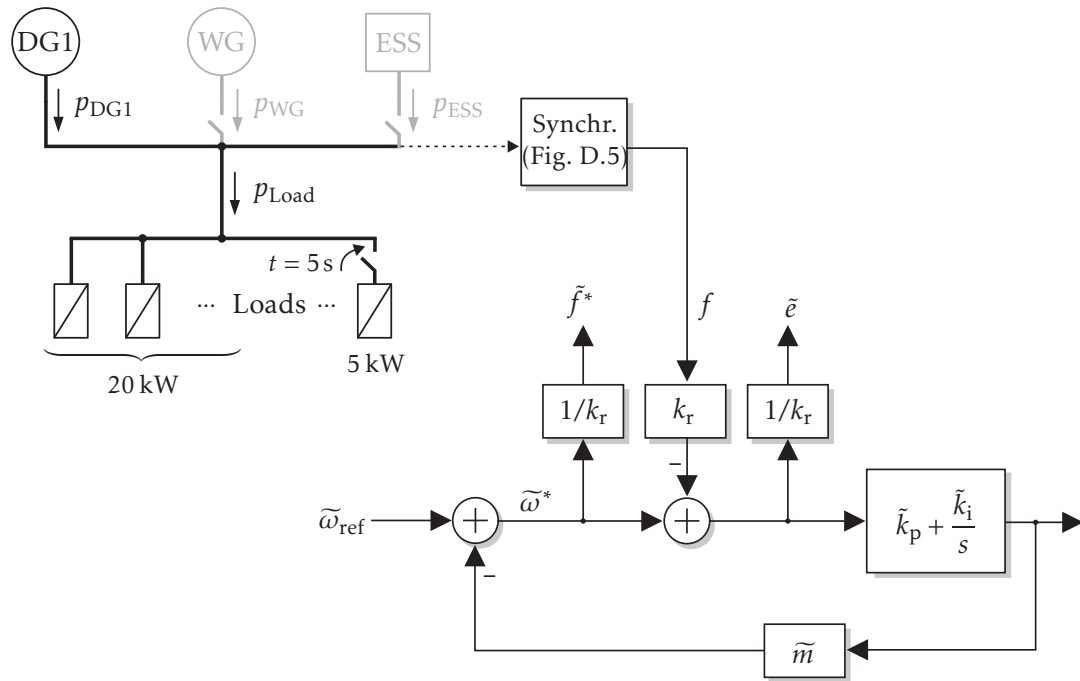
Figure 5.9: Open-loop estimator.

the estimated stabilization frequency, $\tilde{e}$ is the estimated control error, and $\widetilde{\omega}_{\text{ref}}$, $\tilde{k}_{\text{p}}$, $\tilde{k}_{\text{i}}$, $\widetilde{m}$, are parameters of the estimator. In order to keep the estimator simple, it has been defined as an open-loop estimator, which means that its performance will depends on how close its parameters are to the actual parameters of the governor. For this reason, a sensitivity analysis is conducted to evaluate the performance of the estimator for different values of its parameters.

5.4.2   Sensitivity Analysis

The sensitivity analysis is done by simulations and it entails disturbing the system (as shown in Fig. 5.9) with a step-like load increase and plotting the resulting estimated frequency control error ($\tilde{e}$) for different values of the estimator parameters. The possible range of variation for each parameter is defined as [0.5, 1.5] pu of its ideal value (the genset actual parameter). The genset operates in droop mode (6 %), it starts with a load of 20 kW and it is disturbed with a step-like load increase of 5 kW at $t = 5$ s. The VSM is not connected to the grid.

Fig. 5.10 shows the results of the sensitivity analysis. Fig. 5.10(a) shows the waveforms associated to the variation of the proportional gain ($\tilde{k}_{\text{p}}$) while the other parameters remain constant and equal to their ideal values. In the same way, Fig. 5.10(b) and Fig. 5.10(c) show the waveforms associated to the variation of the integral gain and the droop factor, respectively[†]. The frequency control error (e), which is an internal variable of the genset governor, is also shown in these

---

[†]The results for the variation of parameter $\widetilde{\omega}_{\text{ref}}$ are not shown because it was found that its value acted as an initial bias for $\tilde{e}$ which was rapidly eliminated by the integrator, therefore affecting only the start-up of the estimator.

figures.   In order to evaluate the impact of each parameter on the estimation,
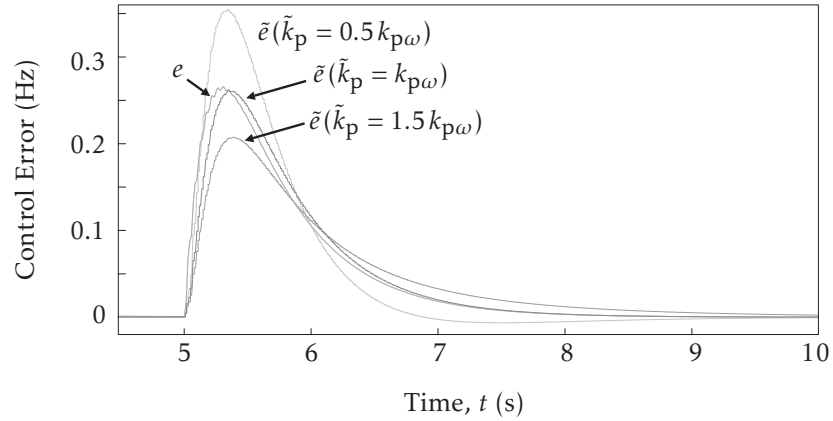
(a)
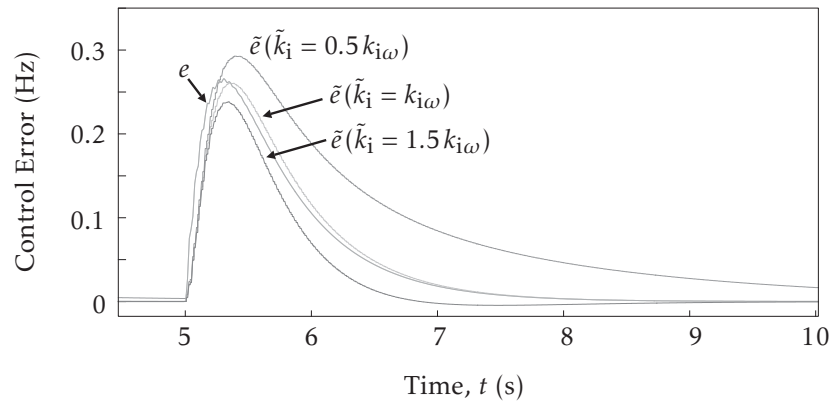
(b)
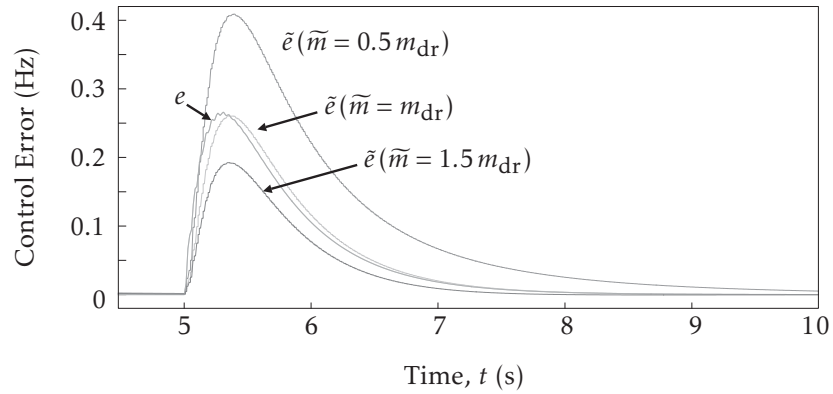
(c)

Figure 5.10: Sensitivity analysis of the estimator parameters on the estimated control error.

(a) Influence of the proportional gain ($\tilde{k}_\mathrm{p}$). (b) Influence of the integral gain ($\tilde{k}_\mathrm{i}$). (c) Influence of the droop factor ($\widetilde{m}$).

the mean absolute error is calculated taking the case when $\tilde{k}_\mathrm{p} = k_{\mathrm{p}\omega}$, $\tilde{k}_\mathrm{i} = k_{\mathrm{i}\omega}$ and $\widetilde{m} = m_\mathrm{dr}$ (which is the best performance that the estimator can achieve) as the reference curve. From the results presented in Table 5.1, it can be observed that the estimation errors are greater when the estimator parameters are below their ideal values (0.5 pu) with a maximum error of 0.103 Hz which corresponds to a 0.17 % of the nominal frequency (60 Hz). The parameter with the highest impact on increasing the estimation error is the droop factor ($\widetilde{m}$), whereas the parameter with the lowest impact on increasing the estimation error is the integral gain ($\tilde{k}_\mathrm{i}$).

After evaluating the variation of each parameter independently, a case where all the parameters presented deviations from their ideal values was considered. To do this, three coefficients were randomly generated[‡] within the range of interest $[0.5,\ 1.5]$ pu and then used to define the parameters of the estimator as: $\tilde{k}_\mathrm{p} = 0.8\,k_{\mathrm{p}\omega}$, $\tilde{k}_\mathrm{i} = 1.3\,k_{\mathrm{i}\omega}$ and $\widetilde{m} = 0.9\,m_\mathrm{dr}$. Fig. 5.11 shows the estimated control error which has a mean absolute error of 0.024 Hz, corresponding to a 0.04 % of the nominal frequency. The relatively low value of this error along with the ones

Table 5.1: Mean absolute errors[*] (Hz) in estimations of Fig. 5.10.

Parameter \ pu value	0.5	1.5
$\tilde{k}_\mathrm{p}$	0.058	0.035
$\tilde{k}_\mathrm{i}$	0.060	0.022
$\widetilde{m}$	0.103	0.035

[*]Calculated as $1/N \sum_{n=1}^{N} |x_n - x_n^\mathrm{ref}|$, where x_n^ref is the reference value and $N = 100$ is the number of points of the analysis.

[‡]Using the MATLAB command "$0.5 + \mathrm{rand}(3,1)$" the obtained coefficients were: 0.8, 1.3 and 0.9.
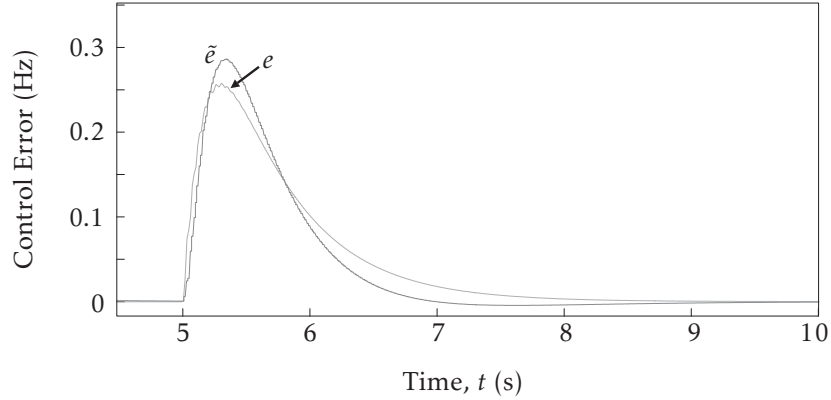
Figure 5.11: Estimated control error for random variation in parameters.

presented in Table 5.1 demonstrate a satisfactory performance of the estimator.

5.4.3   Experimental Results

The schematic of the experimental setup is depicted in Fig. D.9. The genset emulator presented in Chapter 4 is used to represent the diesel generator DG1 of Fig. 5.9 and the loads are represented by a bank of resistors. The VSM is implemented with a second inverter which is controlled by DSP-2. The estimator is also programmed in DSP-2 (see the discrete-time model (D.2) presented in Section D.3). Since only the damping function is evaluated, the reference for the reactive power is set to zero and the reference for the active power is given by (5.20).

In the first test, the genset operates with a droop factor of 6 % and the frequency estimator of the VSM is tuned with the same parameters of the genset. The response of the system to a step-like load increase is first obtained with the VSM disconnected from the grid. Then, the VSM is connected to the grid and the load increase is repeated. Fig. 5.12 shows the frequency of the system f and the
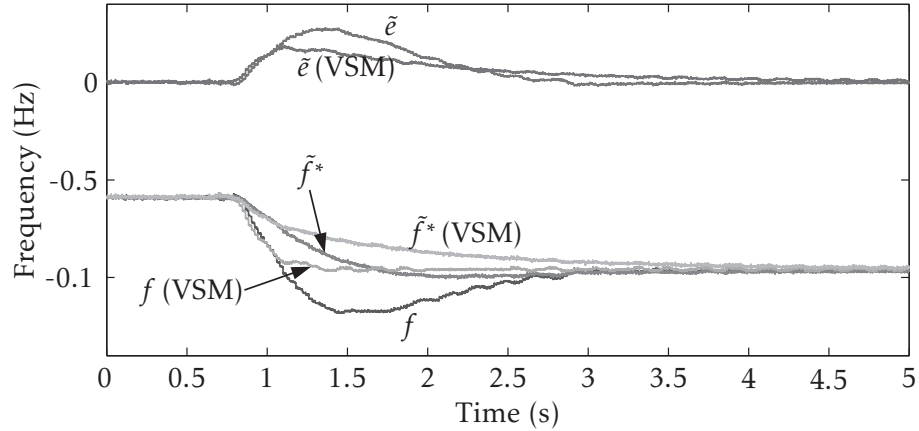
Figure 5.12: Load increase with genset operating with 6% frequency droop.

estimator signals $\tilde{e}$ and f^* for both cases.

A second test is performed to evaluate the performance of the estimator when the droop factor of the genset is reduced to 3 % while the parameters of the estimator remain unchanged (which was originally tuned considering a 6 % droop in the genset). As in the previous test, a step-like load increase is produced with the VSM connected and disconnected from the system. Fig. 5.13 shows the frequency of the system f and the estimator signals $\tilde{e}$ and f^* for both cases.
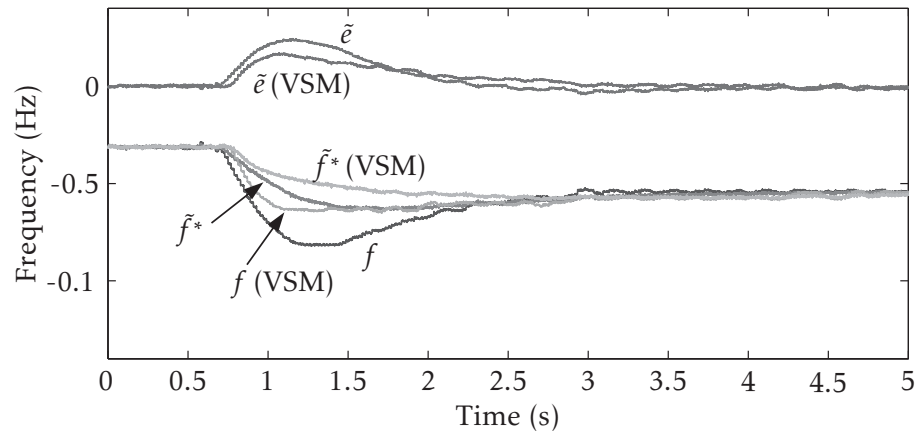
Figure 5.13: Load increase with genset operating with 3% frequency droop.

Finally, the droop factor of the genset is changed to 0 % while the param-
eters of the estimator remain unchanged in its original values. As in the previous
test, a step-like load increase is produced with the VSM connected and discon-
nected from the system. Fig. 5.14 shows the frequency of the system f and the
estimator signals $\tilde{e}$ and f^* for both cases.
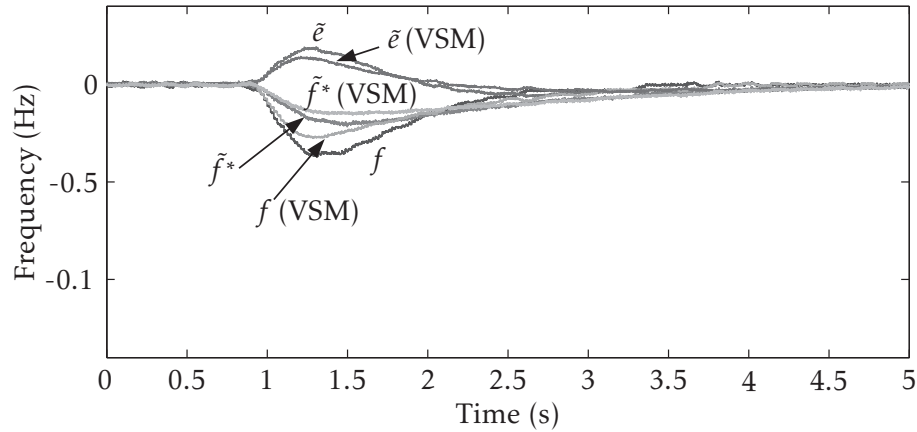
Figure 5.14: Load increase with genset operating in isochronous mode.

These experimental results support the simulation results obtained in the
sensitivity analysis, showing a satisfactory performance of the estimator when
the genset droop factor is reduced from 6 % to 3 % and even to 0 % (isochronous
mode). In all three cases (Fig. 5.12, Fig. 5.13 and Fig. 5.14) the estimated control
error ($\tilde{e}$) converged to zero in approximately 2 s and the VSM was able to effectively
reduce the frequency nadir in 34 %, on average.

5.5   DISCUSSION AND CONCLUSIONS

In this Chapter the concept of a VSM, its theoretical analysis and practical implementation was presented, showing that a VSM can support dynamic frequency control (enhance frequency stability) by adding virtual inertia and damping to the system.

First, a decoupled control strategy for the active and reactive powers of the grid side converter of the ESS was introduced. This control strategy allows independent control over the output powers, which is needed to implement the proposed VSM. The performance of this strategy was evaluated by simulations showing a satisfactory performance.

Then, the equations of the VSM were introduced. Its output power was defined as the addition of two components: the inertial response and the damping power. These two components were presented and evaluated independently. It was shown that the emulation of inertial response helps to attenuate the rate of change of frequency by injecting a power flow (from the ESS) which is proportional to the first derivative of the system frequency. For the calculation of the inertial response a filtered derivative was proposed in order to reduce oscillations due to noise in the measured frequency. A comparison between the filtered and the non-filtered derivative was made by simulations and experimentally. Also, simulations and experimental results of the effects of the inertial response on the system frequency were presented.

Finally, it was shown that the damping power helps to attenuate the am-

plitude of frequency oscillations during a transient. However, it was also shown that a typical formulation of damping power does not work properly when the system operates in droop mode because of the unknown stabilization frequency of the grid. As a solution, an estimator for the stabilization frequency that works in conjunction with the damping function of the VSM was proposed. Theoretical and experimental results showed a satisfactory performance of the proposed VSM with estimator in reducing the frequency nadir for different values of the droop factor of the grid-forming genset.

By performing this dynamic frequency control, the VSM might help to attenuate the frequency variations induced by intermittent (renewable) sources of energy and, therefore, increase its penetration. However, one of the limitations of the VSM is that its overall dynamic performance depends on how fast the interface converter can react and follow the output power reference, and also how fast the energy storage can deliver or absorb energy. Unfortunately, these and other aspects that affect the performance of the VSM are not fully addressed in this thesis and their investigation is suggested as a future work.

CHAPTER 6

SELF-TUNING VIRTUAL SYNCHRONOUS MACHINE

6.1 INTRODUCTION

To the best knowledge of the author, studies published so far on virtual synchronous generators have focused on techniques that consider constant parameters (CP-VSM) [40–47]. In this Chapter, however, a VSM whose parameters vary during operation is proposed. The idea of variable parameters was motivated by the fact that when frequency starts to deviate from steady-state, a larger inertia would present a stronger opposition to the speed change of generators, limiting the initial rate of change of frequency and its peak deviation. On the other hand, when frequency starts to return to steady-state, a larger inertia would no longer be required. Since the value of the damping coefficient also affects the frequency transient response (as shown in **Chapter 3**), its variation during operation is also investigated.

The proposed strategy is called a self-tuning VSM (ST-VSM) because it entails the continuous and autonomous variation of the VSM parameters (damping coefficient and the virtual inertia) by means of on-line optimizations that are constantly performed during the operation of the VSM [82]. In the following Sections the analysis of the performance of the ST-VSM is presented as three cases: first, considering only the variation of the virtual inertia, second, considering only the

variation of the damping coefficient, and third, considering the variation of both parameters together. The following remarks are common to all three cases:

i)   The case of a negative virtual inertia is not considered*.

ii)   The steady-state frequency estimator presented in Chapter 5 is used.

iii)   The goal of the on-line optimization is to attenuate the frequency devia-tions and minimize the power flow through the ESS.

iv)   The optimization is solved by direct search and the algorithm to solve the minimization problems was adapted from the one presented in [83] (refer to this reference for a detailed explanation of the steps involved in the solution).

v)   The limits for the range of variation of the parameters, which is the search vector or search space of the optimization problems, are defined using the operating regions presented in Chapter 3. This allows one to evaluate the potential effects of the ST-VSM on the transient response.

vi)   For implementation purposes, the search space has to be discretized in order to limit the search (iterations of the algorithms) to a finite number of elements. The points within the search space were defined using a linear scale (equally spaced), however any other type of scale can be used.

vii)   The cost function used in the optimization problems were defined as the addition of quadratic terms. Other functions such as the absolute value

---

*The virtual inertia can be made negative to reduce the total inertia of the system. For instance, this condition can be used to speed-up the system when the frequency is returning back to its reference value after a power disturbance. However, if the actual inertia (rotating machinery) of the power system is uncertain, a negative virtual inertia might produce zero or negative total inertia, which might lead the power system to instability.

can also be used. However the quadratic form is chosen because it results

in a faster controller [84].

viii)   The predictive models used to define some terms of the cost functions are

presented in Appendix E.

6.2   VARIATION OF VIRTUAL INERTIA

This algorithm solves in every sampling time the optimization problem

(6.2) searching for an optimal virtual inertia as long as the frequency deviates

from the stabilization value $\tilde{f}^*$, and makes the virtual inertia equal to zero while

the frequency is approaching $\tilde{f}^*$. The algorithm can be summarized as follows:

$$k_{\mathrm{vi}}(k+1) = \begin{cases} \text{solve (6.2)} & \text{if } |\tilde{e}(k)| \geq \epsilon \text{ and } \tilde{e}(k)\dfrac{\mathrm{d}f}{\mathrm{d}t}(k) \leq 0 \\ \\ 0 & \text{otherwise} \end{cases} \tag{6.1}$$

where , $\tilde{e}$ is the estimated control error given by the open-loop estimator defined

in Chapter 5, ϵ is a predefined tolerance band to discriminate the stabilization of

the frequency and the condition $\tilde{e}(k)\mathrm{d}f/\mathrm{d}t(k) \leq 0$ represents the situation when the

frequency is deviating from the stabilization value. The optimization problem to

be solved is formulated as follows:

$$\begin{aligned} \underset{k_{\mathrm{vi}}}{\text{minimize}} \quad & c = \gamma_1 \left(\frac{\mathrm{d}f}{\mathrm{d}t}(k+1)\right)^2 + \gamma_2 \left(k_{\mathrm{vi}}(k+1)\right)^2 \\ \text{subject to:} \quad & k_{\mathrm{vi}} \in \left[K_{\mathrm{vi}}^{\min}, K_{\mathrm{vi}}^{\max}\right] \\ & \gamma_{1,2} > 0 \end{aligned} \tag{6.2}$$

where $\mathrm{d}f/\mathrm{d}t(k+1)$ is the one sampling time ahead prediction of the rate of change of frequency (E.4), $\gamma_{1,2}$ are weight factors that determine the relative importance of each term in the cost function c, and $K_{\mathrm{vi}}^{\min}$ and $K_{\mathrm{vi}}^{\max}$ are the limits of the search space.

6.2.1 Performance Evaluation

A simulation is conducted to compare the performance of the inertial response (with no damping power in order to isolate the effects of the inertia) between the ST-VSM and the CP-VSM. Fig. 6.1 depicts the schematic of the simulated system. The test consists in a load increase of $5\,\mathrm{kW}$ at $t = 1\,\mathrm{s}$ (from an initial load of $20\,\mathrm{kW}$) while only one genset (DG1) is connected to the system and it operates in isochronous mode. The same test is conducted for the system without VSM, with the CP-VSM, and two cases of ST-VSM (with different values of the weight factor γ_2). Parameters used for the ST-VSM in the simulations are presented in Table E.1. Fig. 6.2 shows the search vector for the ST-VSM within the operating region of DG1. It can be seen that for the search vector $k_{\mathrm{vi}} \in [0, 2]$, the ST-VSM can

Figure 6.1: ST-VSM with variation of virtual inertia.

modify the peak frequency deviation in the range of $[0.42, 0.54]$ Hz and the peak time in the range of $[0.2, 0.35]$ s.

Fig. 6.3 shows the simulation results, where the curve labeled "No VSM"
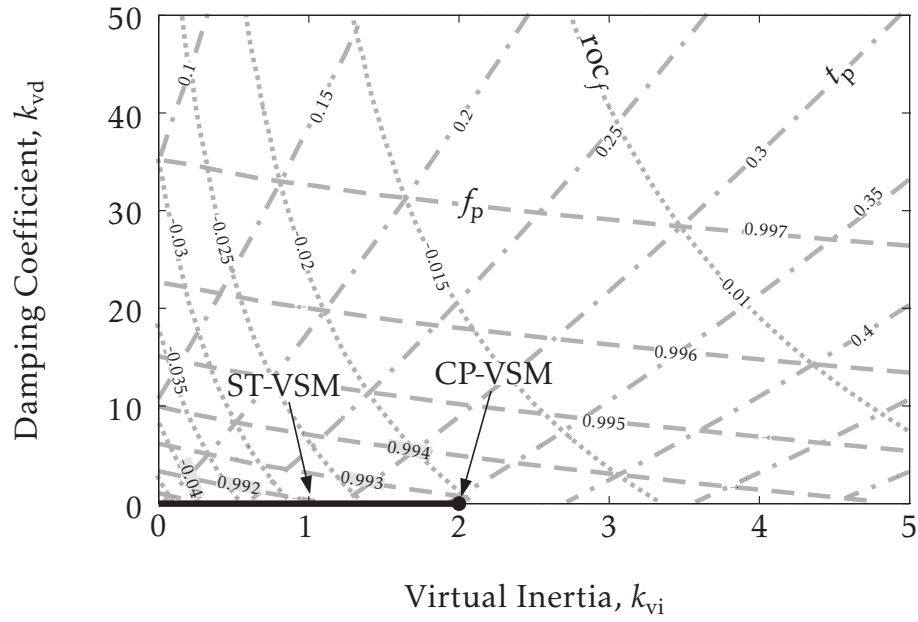
Figure 6.2: Search vector for the ST-VSM with variable inertia.
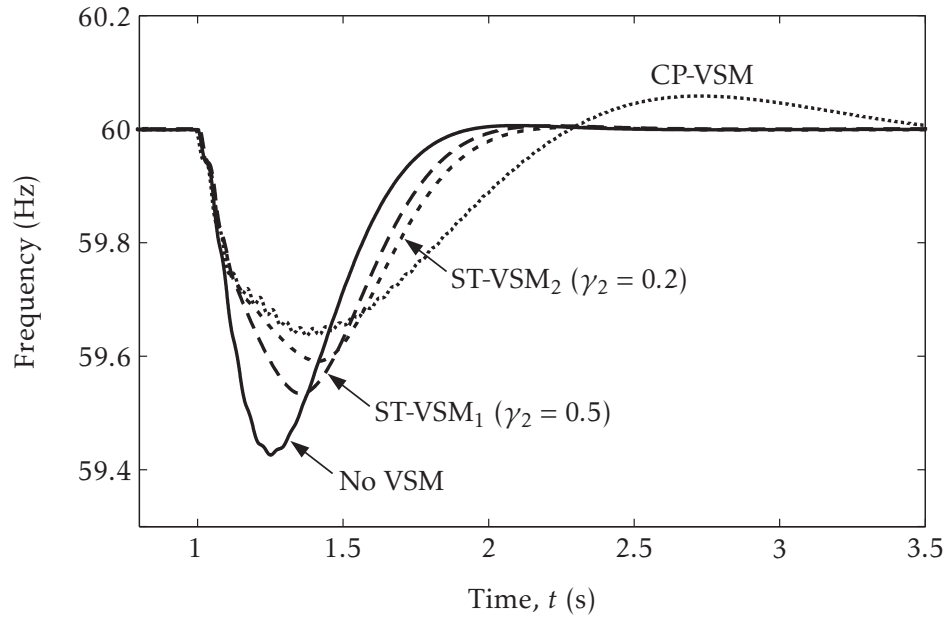
Figure 6.3: Effects of the inertial response of the CP-VSM and ST-VSM on the grid frequency.

is the original response of DG1, "CP-VSM" is the response of DG1 plus the VSM

with constant inertia, and "ST-VSM$_{1,2}$" are the responses of DG1 plus ST-VSM for

two different values of the weight factor γ_2. It is observed that the curves "ST-

VSM$_{1,2}$" present a frequency nadir that lies between the other two curves (see also

Δf_p in Table 6.1). This is because the maximum value of inertia for the ST-VSM

has been set to 2, which is the virtual inertia of the CP-VSM. If the virtual inertia

of the ST-VSM is allowed to vary beyond the value used by CP-VSM, a greater

reduction of the frequency nadir is expected to happen. Finally, it is observed that

as the weight factor γ_2 is decreased the frequency nadir also decreases, which can

be attributed to the fact that a reduction of γ_2 reinforces the minimization of the

df/dt in (6.2).

Table 6.1: Performance comparison between the inertial response of the CP-VSM and the ST-VSM.

VSM Type	Δf_p (Hz)	t_p (s)	Settling Time (s)	Delivered Energy (kJ)	Recovered Energy (kJ)
No VSM	0.56	0.24	0.76	0	0
CP-VSM	0.37	0.36	2.26	0.47	0.44
ST-VSM$_1$	0.45	0.33	0.91	0.27	0
ST-VSM$_2$	0.4	0.41	1	0.4	0

On the other hand, Fig. 6.4 shows the simulation results for the variation

of the virtual inertia and the d-axis current of the ESS. It is observed that, because

the ST-VSM makes its virtual inertia equal to 0 right after the nadir happens, as

shown in Fig. 6.4(c) and Fig. 6.4(e), the frequency stabilizes, on average, 2.4 times

faster than the CP-VSM (see the settling time in Table 6.1) and delivering up to

Figure 6.4: Comparison between the inertial response of the CP-VSM and ST-VSM.

Waveforms associated to the frequency variation of Fig. 6.3. (a)-(b): variation of the virtual inertia and the corresponding ESS output active current for the CP-VSM. (c)-(d): same waveforms for the ST-VSM$_1$. (e)-(f): same waveforms for the ST-VSM$_2$.

42 % less energy (in the case of ST-VSM$_1$). As a trade-off, the ST-VSM does not recover energy as the CP-VSM does by reversing the current as shown in Fig. 6.4(b) (see also delivered and recovered energy in Table 6.1). Nevertheless, the ST-VSM

has the potential to be programmed to assist frequency control as shown here and then recharge its energy storage at a later time once the system has stabilized. A solution of this type, might be able to accomplish both tasks without compromising the performance of the ST-VSM.

6.3   VARIATION OF DAMPING COEFFICIENT

In this case, the optimization algorithm searches for a damping coefficient that attenuates the frequency deviations and the power flow through the ESS at the same time. If such a damping coefficient is found, it is said to be optimal. The optimization problem is formulated as follows:

$$
\begin{aligned}
\underset{k_{\text{vd}}}{\text{minimize}} \quad & c = \gamma_1 \left(\tilde{f}^*(k+1) - f(k+1) \right)^2 + \gamma_2 \left(k_{\text{vd}}(k+1) \right)^2 \\
\text{subject to:} \quad & k_{\text{vd}} \in \left[K_{\text{vd}}^{\min}, K_{\text{vd}}^{\max} \right] \\
& \gamma_{1,2} > 0
\end{aligned}
\tag{6.3}
$$

where $f(k+1)$ is the one sampling time ahead prediction of the grid frequency (E.7), $\gamma_{1,2}$ are weight factors that determine the relative importance of each term in the cost function c, and $K_{\text{vd}}^{\min}$ and $K_{\text{vd}}^{\max}$ are the limits of the search space.

6.3.1   Performance Evaluation

A simulation is conducted to compare the performance of the damping function (with no inertial response in order to isolate the effects of the damping) between the ST-VSM and the CP-VSM. **Fig. 6.5** depicts the schematic of the simulated system. The test consists in a load increase of $5\,\text{kW}$ at $t = 1\,\text{s}$ (from an

initial load of 20 kW) while only one genset (DG1) is connected to the system and it operates in isochronous mode. The same test is conducted for the system without VSM, with the CP-VSM, and two cases of ST-VSM (with different values of the weight factor γ_2). Parameters used for the ST-VSM in the simulations are presented in Table E.2. Fig. 6.6 shows the search vector for the ST-VSM within the operating region of DG1. It can be seen that for the search vector $k_{vd} \in [0, 10]$, the
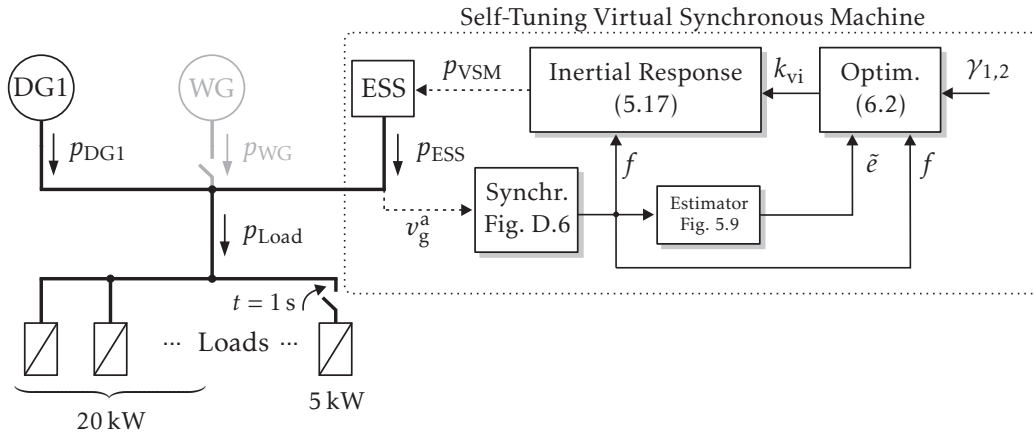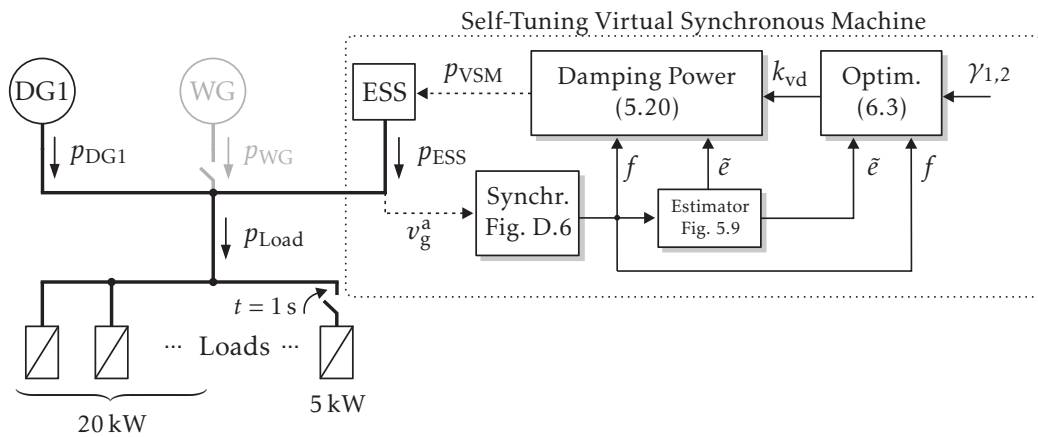

Figure 6.5: ST-VSM with variation of damping.
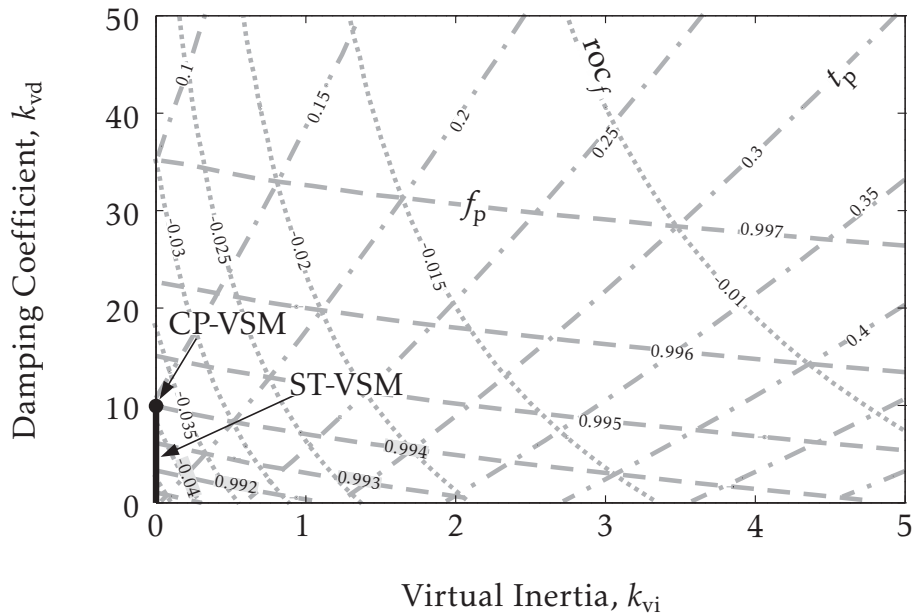
Figure 6.6: Search vector for the ST-VSM with variable damping.

ST-VSM can modify the peak frequency deviation in the range of $[0.36, 0.54]\,$Hz and the peak time in the range of $[0.15, 0.2]\,$s.

Fig. 6.7 shows the simulation results, where the curve labeled "No VSM" is the original response of DG1, "CP-VSM" is the response of DG1 plus the VSM with constant damping coefficient, and "ST-VSM$_{1,2}$" are the responses of DG1 plus ST-VSM for two different values of the weight factor γ_2. It is observed that the curves "ST-VSM$_{1,2}$" present a frequency nadir and settling time that lie between the other two curves (see Δf_p and also the settling time in Table 6.2). This is because the maximum value of damping coefficient for the ST-VSM has been set to 10, which is the damping coefficient of the CP-VSM. If the damping coefficient of the ST-VSM is allowed to vary beyond the value used by CP-VSM, a greater reduction of the frequency nadir is expected to happen. On the other hand, and due to the over-damping of the system, the settling time is expected to be greater than the
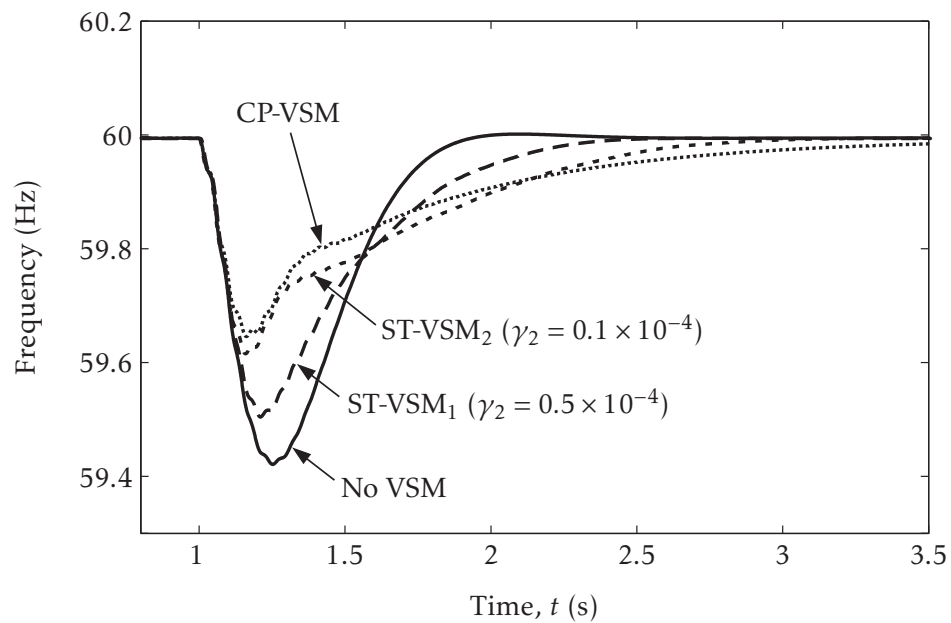
Figure 6.7: Effects of the damping power of the CP-VSM and ST-VSM on the grid frequency.

Table 6.2: Performance comparison between the damping function of the CP-VSM and the ST-VSM.

VSM Type	Δf_{p} (Hz)	t_{p} (s)	Settling Time (s)	Delivered Energy (kJ)	Recovered Energy (kJ)
No VSM	0.56	0.24	0.76	0	0
CP-VSM	0.35	0.17	1.85	1.71	0
ST-VSM$_1$	0.49	0.21	1.15	0.32	0
ST-VSM$_2$	0.38	0.17	1.46	0.96	0

one achieved by the CP-VSM. Finally, it is observed that as the weight factor γ_2 is decreased the frequency nadir also decreases, which can be attributed to the fact that a reduction of γ_2 reinforces the minimization of $\tilde{f}^*(k+1) - f(k+1)$ in (6.3).

On the other hand, Fig. 6.8 shows the simulation results for the variation of the damping coefficient and the d-axis current of the ESS. It is observed that ST-VSM$_2$ achieves almost the same reduction in the frequency nadir than CP-VSM, but using approximately 56 % of the delivered energy (see **Fig. 6.8(b)**, **Fig. 6.8(f)** and delivered energy in Table 6.2) and reducing the settling time in 21 % at the same time.
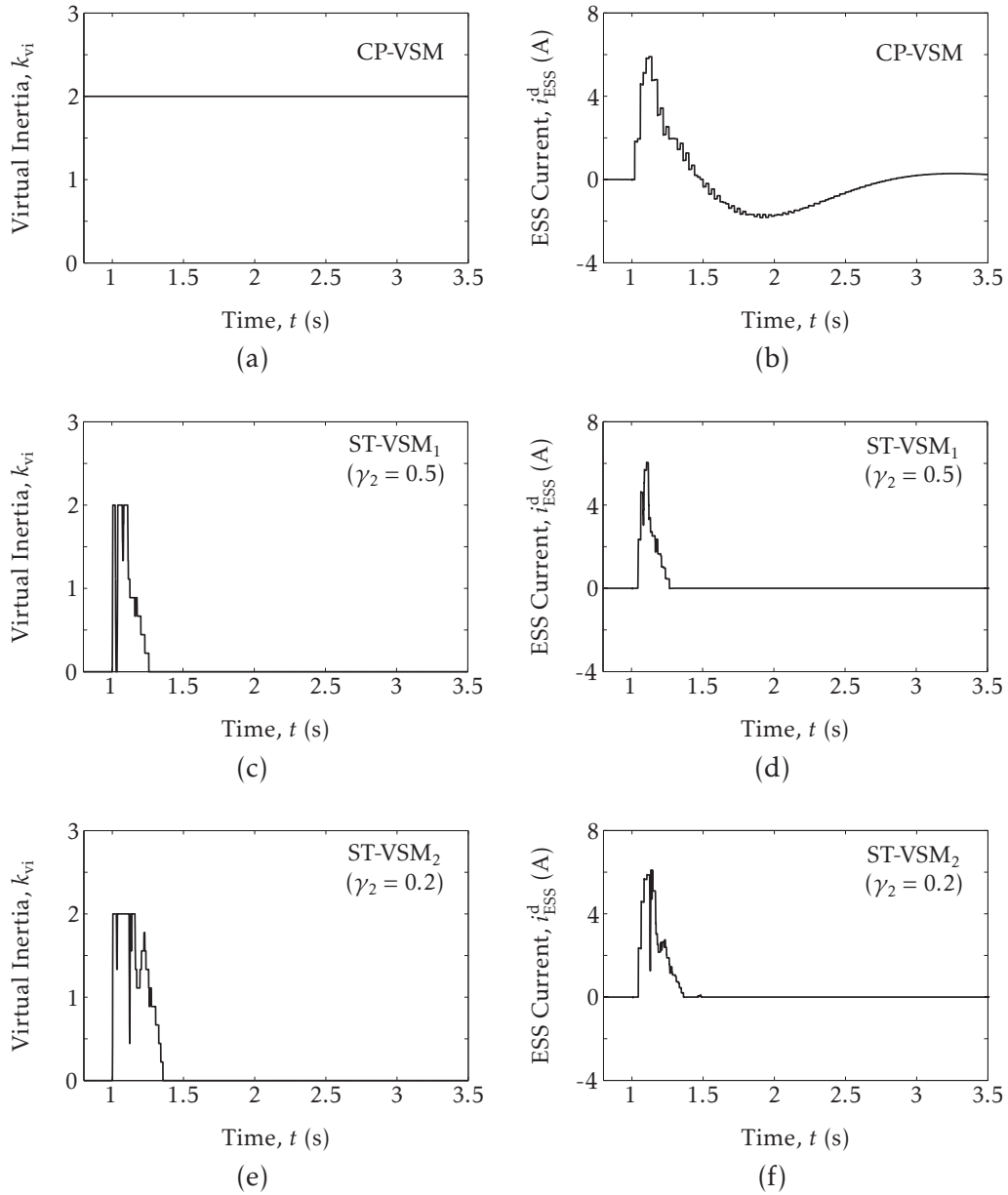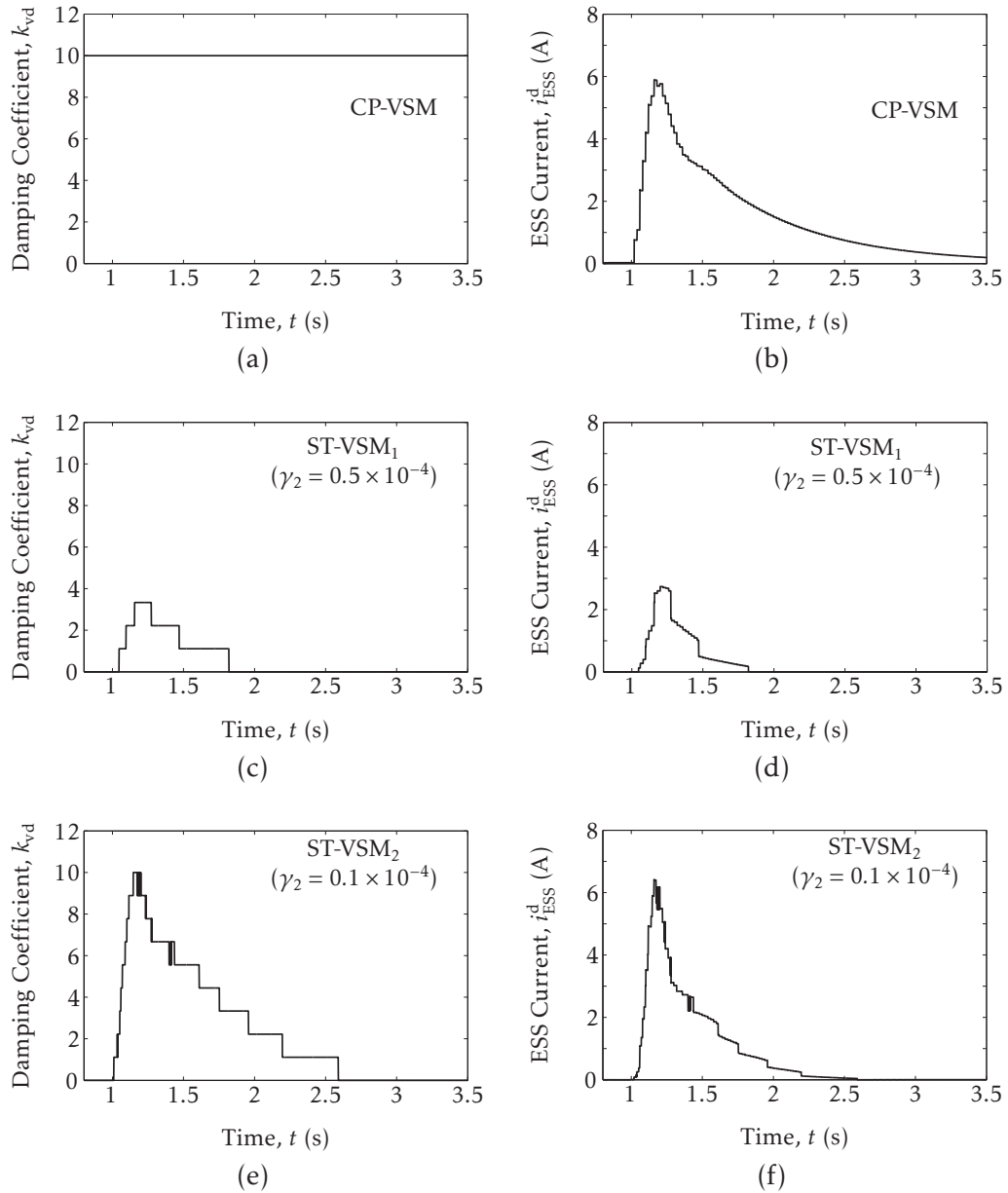
Figure 6.8: Comparison between the damping function of the CP-VSM and ST-VSM.

Waveforms associated to the frequency variation of Fig. 6.7. (a)-(b): variation of the damping coefficient and the corresponding ESS output active current for the CP-VSM. (c)-(d): same waveforms for the ST-VSM$_1$. (e)-(f): same waveforms for the ST-VSM$_2$.

6.4 VARIATION OF INERTIA AND DAMPING

To combine the effects of the previously defined inertial response and damping function, the output power of the ST-VSM is defined as:

$$p_{\text{VSM}} = -k_{\text{vi}}k_r^2 f \frac{\mathrm{d}f}{\mathrm{d}t} + k_{\text{vd}}k_r^2 f \left(\tilde{f}^* - f \right) \tag{6.4}$$

In this case, the solution algorithm solves the optimization problem (6.5) (which is a combination of the two previously defined optimization problems), searching for a damping coefficient and a virtual inertia as long as the frequency deviates from the stabilization value $\tilde{f}^*$.

$$\underset{(k_{\text{vi}}, k_{\text{vd}})}{\text{minimize}} \quad c = \gamma_1 \left(\frac{\mathrm{d}f}{\mathrm{d}t}(k+1) \right)^2 + \gamma_2 \left(k_{\text{vi}}(k+1) \right)^2$$

$$+ \gamma_3 \left(\tilde{f}^*(k+1) - f(k+1) \right)^2 + \gamma_4 \left(k_{\text{vd}}(k+1) \right)^2 \tag{6.5}$$

$$\text{subject to:} \quad (k_{\text{vi}}, k_{\text{vd}}) \in \left[K_{\text{vi}}^{\min}, K_{\text{vi}}^{\max} \right] \times \left[K_{\text{vd}}^{\min}, K_{\text{vd}}^{\max} \right]$$

$$\gamma_{1...4} > 0$$

Otherwise, it makes the virtual inertia equal to zero and solves the previously defined optimization problem (6.3), searching for a damping coefficient only. The algorithm can be summarized as follows:

$$(k_{\text{vi}}(k+1), k_{\text{vd}}(k+1)) = \begin{cases} \text{solve (6.5)} & \text{if } |\tilde{e}(k)| \geq \epsilon \text{ and } \tilde{e}(k) \dfrac{\mathrm{d}f}{\mathrm{d}t}(k) \leq 0 \\[2ex] \begin{array}{l} k_{\text{vi}}(k+1) = 0 \\ \text{solve (6.3)} \end{array} & \text{otherwise} \end{cases} \tag{6.6}$$

6.4.1 Performance Evaluation

Two simulation tests (which are described in the next sections) are conducted to compare the performance between the proposed ST-VSM and the CP-VSM. Fig. 6.9 depicts the schematic of the simulated system and the parameters used for the ST-VSM are presented in Table E.3. Fig. 6.10 shows the search area for the ST-VSM ($\mathcal{A}$) within the operating region of DG1. It can be seen that for the search area defined by $k_{vi} \in [0, 2]$ and $k_{vd} \in [0, 10]$, the ST-VSM can modify the peak
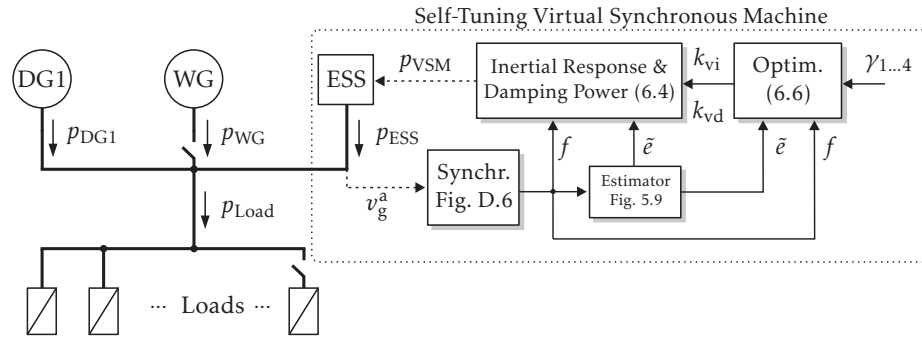
Figure 6.9: ST-VSM with variable inertia and damping.
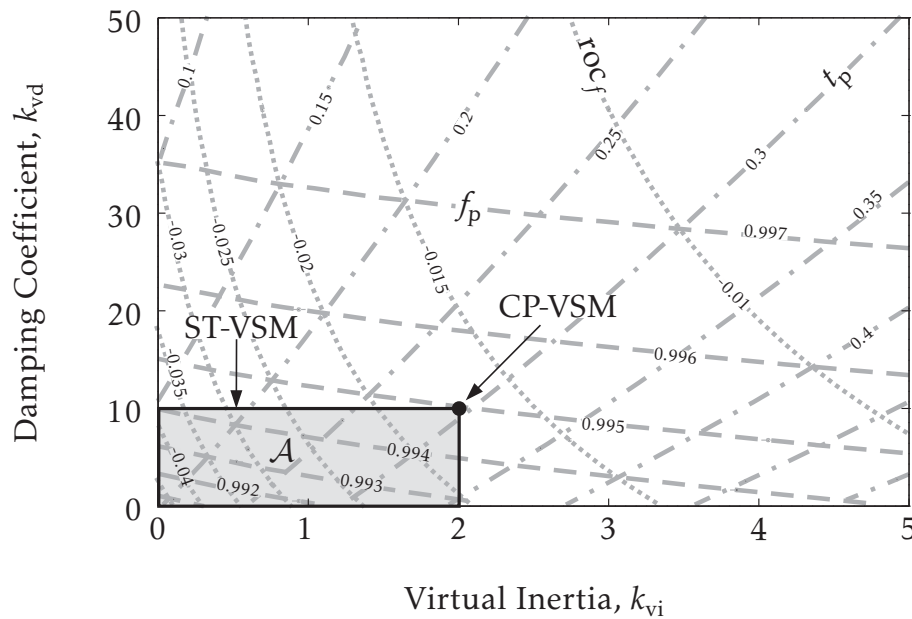
Figure 6.10: Search area for the ST-VSM with variable inertia and damping.

frequency deviation in the range of $[0.3, 0.54]$ Hz and the peak time in the range of $[0.15, 0.35]$ s.

A.   *Load Change*

This test consists of a load increase of 5 kW at $t = 1$ s (from an initial load of 20 kW) while only one genset (DG1) is connected to the system and it operates in isochronous mode. The same test is conducted for the system without VSM, with the CP-VSM, and with the ST-VSM. Fig. 6.11 and Fig. 6.12 show the simulation results, where the curves labeled "No VSM" are associated to the original response of DG1, "CP-VSM" to the response of DG1 plus the VSM with constant parameters, and "ST-VSM" to the response of DG1 plus the self-tuning VSM. From Fig. 6.11 it is observed that with the CP-VSM, the system presents the lowest frequency nadir but the settling time is increased (see also Δf_{p} and settling time in Table 6.3).
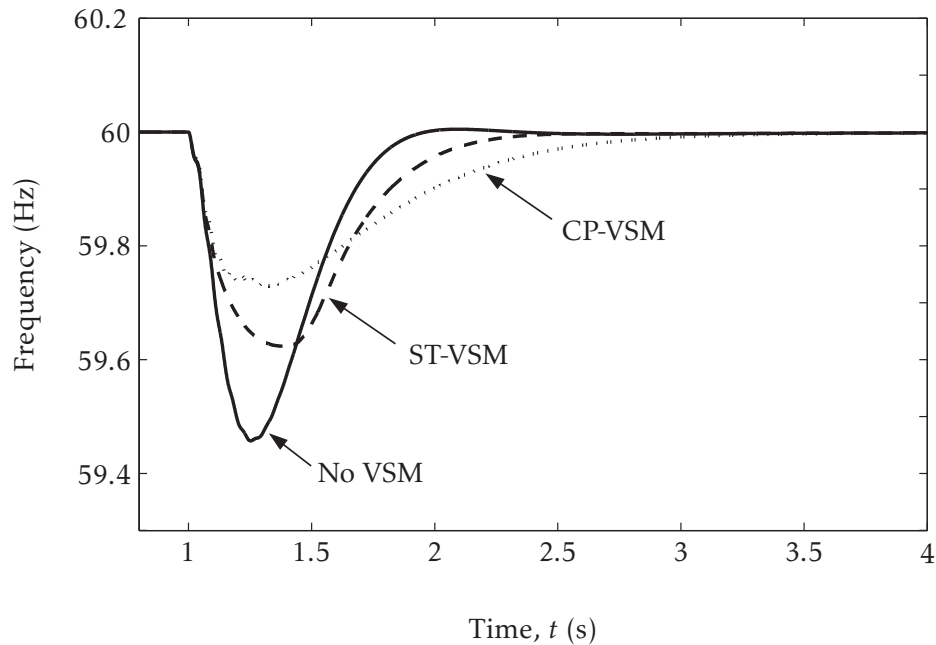
Figure 6.11: Effect of the CP-VSM and ST-VSM on the grid frequency under a load increase.
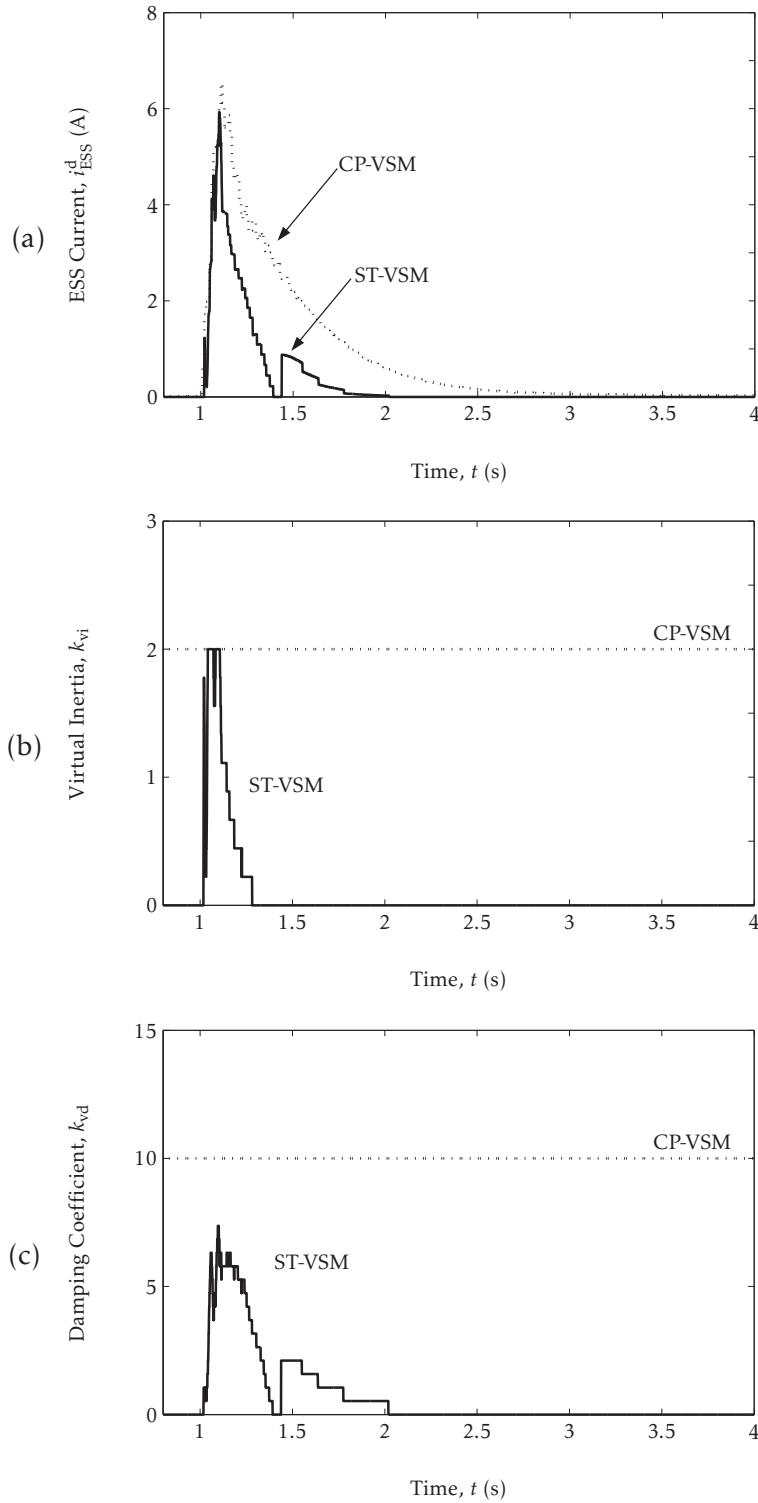
Figure 6.12: Comparison between CP-VSM and ST-VSM under a load increase.

Waveforms associated to Fig. 6.11. (a) ESS output current. (b) Variation of virtual inertia. (c) Variation of damping coefficient.

Table 6.3: Performance comparison between CP-VSM and ST-VSM under a load increase.

VSM Type	Δf_p (Hz)	t_p (s)	Settling Time (s)	Delivered Energy (kJ)	Recovered Energy (kJ)
No VSM	0.56	0.24	0.76	0	0
CP-VSM	0.27	0.3	1.52	1.1	0
ST-VSM	0.37	0.38	1.06	0.42	0

On the other hand, with the ST-VSM the system presents a reduced settling time but a higher frequency nadir, however, it uses only 38 % of the energy used by CP-VSM, as it can be seen from the current waveforms in Fig. 6.12(a) (see also delivered energy in Table 6.3).

B.   *Wind Power*

This test is to compare the performance of the CP-VSM and the ST-VSM under continuous load changes produced by the output power of a wind generator (WG). The model and parameters for the wind generator are presented in Appendix F. The wind generator generates power according to the wind profile of Fig. F.2(a) while only one genset (DG1) is connected to the system (operating in isochronous mode) and the load is kept constant at 20 kW. The same test is conducted for the system without VSM, with the CP-VSM, and with the ST-VSM. Fig. 6.13 and Fig. 6.14 show the simulation results, where the curves labeled "No VSM" are associated to the original response of DG1, "CP-VSM" to the response of DG1 plus the VSM with constant parameters, and "ST-VSM" to the response of DG1 plus the self-tuning VSM.
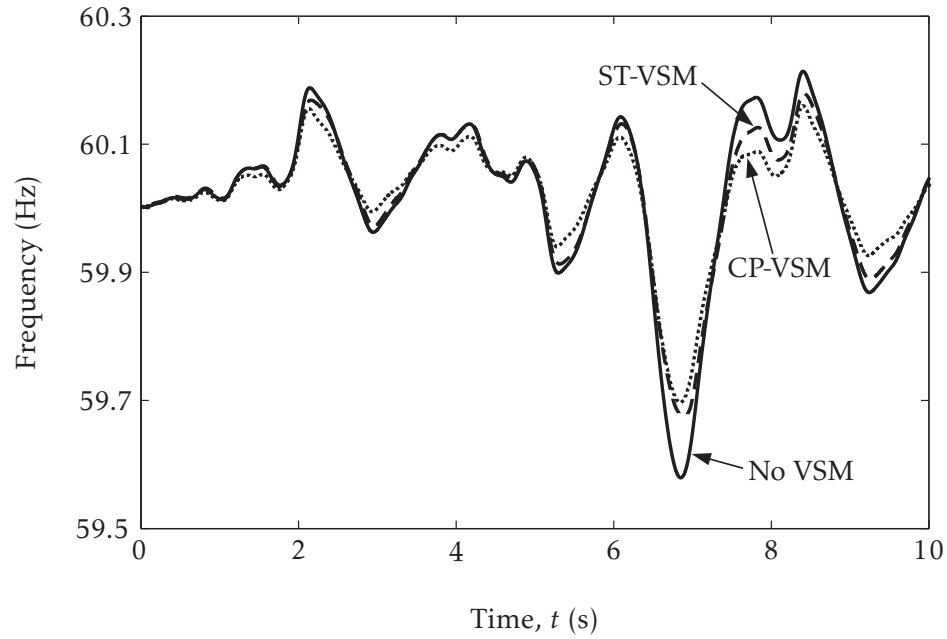
Figure 6.13: Effect of the CP-VSM and ST-VSM on the grid frequency under wind power.

From Fig. 6.13 it is observed that the CP-VSM achieved a greater reduction (31 %) of the maximum frequency deviation than the ST-VSM (24 %), however both frequency curves differ, on average, in only 0.016 Hz. Therefore, it can be said that the ST-VSM achieved a very similar performance than the CP-VSM, while minimizing the power flow through the ESS in 58 % (see the output current of the ESS in Fig. 6.14(a)). However, for this particular wind profile, the CP-VSM ends up charging the energy storage with 0.48 kJ and the ST-VSM ends up discharging the energy storage with 0.49 kJ. Table 6.4 summarizes the simulation results.
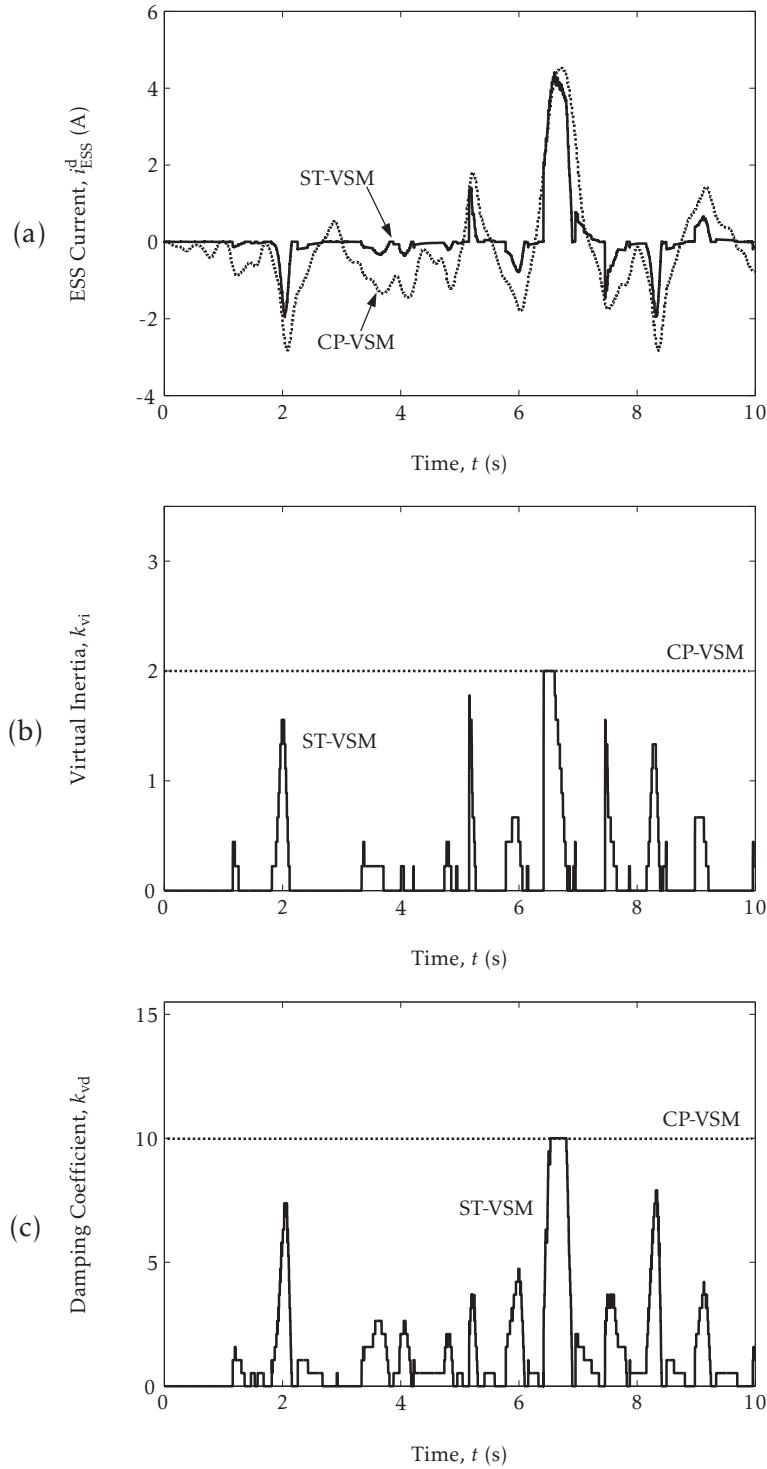
Figure 6.14: Comparison between CP-VSM and ST-VSM under wind power.

Waveforms associated to Fig. 6.13. (a) ESS output current. (b) Variation of virtual inertia. (c) Variation of damping coefficient.

Table 6.4: Performance comparison between CP-VSM and ST-VSM under wind power.

VSM Type	Maximum Δf_p (Hz)	MAE* (Hz)	Delivered Energy (kJ)	Recovered Energy (kJ)
No VSM	0.42	NA	0	0
CP-VSM	0.29		1.38	1.86
		0.016		
ST-VSM	0.32		0.87	0.38

*Mean absolute error calculated only between frequency waveforms "CP-VSM" and "ST-VSM" as $1/N \sum_{n=1}^{N} |x_n - y_n|$.

6.5 DISCUSSION AND CONCLUSIONS

In this Chapter the concept of a self-tuning VSM was explored. Based on the VSM presented in Chapter 5, optimizations algorithms were designed in order to find, through on-line calculations, optimal parameters (virtual inertia and damping coefficient) that minimize the frequency deviations (amplitude and rate of change) and the power flow through the ESS. The search spaces for the optimization algorithms were defined based on the concept of the operating regions (presented in Chapter 3), which allowed to know a priori the expected performance of the ST-VSM.

The performance of the inertial response and the damping power of the ST-VSM were evaluated independently for a step-like load change. Then, the performance of both functions (acting together) was evaluated for a step-like load change and for continuous load changes induced by a wind generator. For implementation purposes it is important to consider that, because of the direct search method used to solve the optimization problems, the calculation of the inertial re-

sponse involves N_{vi} iterations, the damping power N_{vd} iterations, and both functions $N_{vi} \cdot N_{vd}$ iterations. Therefore, provisions must be taken in order to assure enough processing power for the full deployment of the ST-VSM, which represents the case of the highest computational burden.

For the simulated cases it was found that, in general, the ST-VSM achieved a similar performance to that of the CP-VSM, but with a reduced power flow through the ESS. Moreover, the ST-VSM was found to be more efficient than the CP-VSM in reducing the frequency variations. However, it was also found that, depending on the type of load variation, the operation of the proposed ST-VSM may result in a greater discharge of the energy storage. This issue might be attributed to factors related to the optimization problems, such as: the type of cost functions, the value of the weight factors and the definition of search spaces. Since none of these factors were studied in this thesis, further work is required to characterize their impact on the performance of the ST-VSM.

CHAPTER 7

SUMMARY AND CONCLUSIONS

7.1 SUMMARY

In diesel-hybrid autonomous power systems, a reduced number of diesel generators supply the power to the load and control the frequency of the system in isolation from the utility grid. In these type of systems, frequency variations of consequence are more likely to occur than in large interconnected power grids, since they feature a relatively small generation capacity and rapid changes in power demand. If generators are not able to maintain frequency within prescribed operational limits during a transient, the assistance of other components is required in order to avoid major disruptions in the power system.

Studies show that virtual synchronous machines can be implemented in grid-connected inverters to support dynamic frequency control by emulating inertial response. However, it also has been shown that changing the inertia of a system without adjusting the governors of generators typically results in a more oscillatory transient response. Injecting damping power at the same time than emulating inertia, might help to attenuate the oscillations. This approach, and the capability of VSMs in changing its parameters during operation, have received little attention in the literature related to VSMs. In this thesis a VSM that changes its parameters during operation and its application to support dynamic frequency control in a diesel-hybrid autonomous power system was investigated. In particu-

lar, the following aspects were covered:

In Chapter 2, a mathematical model for the diesel generator was developed. The values for most of the parameters of the model were selected from commercially available components and the controllers were tuned in order to have a frequency and voltage response according to the standard ISO 8528-5:2005.

In Chapter 3, the effects of additional inertia and damping power in the system on the frequency transient response of the diesel generator were studied. As a result, it was possible to define graphical representations (called the operating regions) to relate the values of the additional inertia and damping power with key parameters of the genset transient response.

The implementation of an inverter-based genset emulator was presented in Chapter 4. The model developed in Chapter 2 was discretized and programmed in a DSP. The output voltages of the model were used as references to control the output voltages of the inverter, so it behaves as the genset. The static and transient response of the emulator were verified experimentally.

A virtual synchronous machine for dynamic frequency control was presented in Chapter 5 and practical considerations regarding the synchronization of the VSC with the grid, the frequency measurement and the implementation of the inertial response and the damping power were discussed. Also, an estimator for the stabilization frequency of the grid was designed in order to inject damping power when the grid operates in frequency droop mode. Simulation and experimental results were presented.

Finally, a self-tuning VSM was presented in **Chapter 6**. The proposed strategy continuously performs the on-line minimization of a cost function that provides optimal values for the virtual inertia and damping coefficient of the VSM. The cost functions were defined using a predictive model strategy and the search spaces of the optimization problems were defined using the concept of the operating regions defined in **Chapter 3**. The performance of the ST-VSM was evaluated by simulations for step-like load changes and wind power generation.

The softwares used for design and simulation were: MATLAB version 7.8.0.347 (R2009a) and PLECS version 3.2.7. Semikron converters (Semiteach) were used in the experimental setups. Digital implementations were based on the development board eZdsp-TMS320F3812 from Spectrum Digital and the expansion board F2812-DAQ from Link Research.

7.2 CONCLUSIONS

The general conclusion of this thesis is that a VSM that changes its parameters during operation can provide the necessary inertia and damping to support dynamic frequency control in a diesel-hybrid APS. In particular, the following conclusions are reached in this thesis:

i) The proposed ST-VSM reduces the power flow through the ESS and the amplitude and initial rate of change of the frequency variations. Moreover, the proposed ST-VSM was found to be more efficient than the CP-VSM in reducing the frequency variations.

ii) It was shown that an estimator for the stabilization frequency is an effec-

tive solution to perform the damping function of the VSM when the APS operates under droop control.

iii)   The proposed operating regions can be used to estimate the impact of the VSM on the transient frequency response and to design the search spaces for the optimization problems of the ST-VSM.

7.3   SUGGESTIONS FOR FUTURE WORK

As an extension of this study, the following topics are suggested:

i)   Extend the concept of the operating regions to include the effect of the droop factor in a single graphical representation.

ii)   Identify the most important factors that limit the performance of the proposed ST-VSM in practice.

iii)   Investigate the influence of the type of cost functions, the values of the weight factors and the definition of search spaces on specific aspects of the performance of the proposed ST-VSM.

iv)   Extend the proposed ST-VSM to include the state of charge of the energy storage in the control strategy.

v)   Extend the proposed ST-VSM to operate with hybrid energy storages.

REFERENCES

[1] J. Machowski, J. W. Bialek, and B. J. R., *Power system dynamics: stability and control*.   John Wiley & Sons, Ltd., 2008.

[2] H. Brevani, *Robust Power System Frequency Control*.   Springer Science+Business Media, LLC, 2009.

[3] *IEEE Std 1159-2009 (Revision of IEEE Std 1159-1995) Recommended Practice for Monitoring Electric Power Quality*, IEEE Std., 2009.

[4] H. Nacfaire, Ed., *Wind-diesel and wind autonomous energy systems*.   Elsevier Science, 1989.

[5] I. Boldea, *Synchronous Generators Handbook*, L. L. Grigsby, Ed.   CRC Press, 2006.

[6] Y. Z. Sun, Z. S. Zhang, G. J. Li, and J. Lin, "Review on frequency control of power systems with wind power penetration," in *Power System Technology (POWERCON), 2010 International Conference on*, Oct. 2010.

[7] R. Cosse, M. Alford, M. Hajiaghajani, and E. Hamilton, "Turbine/generator governor droop/isochronous fundamentals - a graphical approach," in *Petroleum and Chemical Industry Conference (PCIC), 2011 Record of Conference Papers Industry Applications Society 58th Annual IEEE*, Sep. 2011.

[8] P. Kundur, J. Paserba, V. Ajjarapu, G. Andersson, A. Bose, C. Canizares, N. Hatziargyriou, D. Hill, A. Stankovic, C. Taylor, T. Van Cutsem, and V. Vittal, "Definition and classification of power system stability IEEE/CIGRE joint task force on stability terms and definitions," *IEEE Transactions on Power Systems*, vol. 19, no. 3, pp. 1387–1401, Aug. 2004.

[9] C. Concordia, L. Fink, and G. Poullikkas, "Load shedding on an isolated system," *IEEE Transactions on Power Systems*, vol. 10, no. 3, pp. 1467–1472, Aug. 1995.

[10] *IEEE Std C37.117-2007 Guide for the Application of Protective Relays Used for Abnormal Frequency Load Shedding and Restoration*, IEEE Std., Sep. 2007.

[11] J. Milanovic and N. Soultanis, "The influence of controlled and fixed load composition on operation of autonomous wind-diesel system," in *IEEE Power Tech Proceedings*, vol. 4, Sep. 2001.

[12] C. Marinescu, C. Ion, I. Serban, L. Clotea, and D. Marinescu, "Controlling a stand-alone power system," in *Power Electronics*, *Electrical Drives*, *Automation and Motion*, *2006. SPEEDAM 2006. International Symposium on*, May 2006, pp. 525–530.

[13] Y. Y. Hong and S. F. Wei, "Multiobjective underfrequency load shedding in an autonomous system using hierarchical genetic algorithms," *IEEE Transactions on Power Delivery*, vol. 25, no. 3, pp. 1355–1362, Jul. 2010.

[14] Y. Y. Hong and P. H. Chen, "Genetic-based underfrequency load shedding in a stand-alone power system considering fuzzy loads," *IEEE Transactions on Power Delivery*, vol. 27, no. 1, pp. 87–95, Jan. 2012.

[15] F. Bianchi, R. Mantz, and H. D. Battista, Eds., *Wind Turbine Control Systems*. Springer-Verlag, 2007.

[16] A. Haruni, A. Gargoom, M. Haque, and M. Negnevitsky, "Voltage and frequency stabilisation of wind-diesel hybrid remote area power systems," in *Power Engineering Conference*, *2009. AUPEC 2009. Australasian Universities*, Sep. 2009.

[17] J. Morren, S. de Haan, and J. Ferreira, "Contribution of DG units to primary frequency control," in *Future Power Systems*, *2005 International Conference on*, Nov. 2005.

[18] S. Hurtado, G. Gostales, A. de Lara, N. Moreno, J. Carrasco, E. Galvan, J. Sanchez, and L. Franquelo, "A new power stabilization control system based on making use of mechanical inertia of a variable-speed wind-turbine for stand-alone wind-diesel applications," in *IEEE 2002 28th Annual Conference of the Industrial Electronics Society*, vol. 4, Nov. 2002, pp. 3326–3331.

[19] M. F. M. Arani and E. F. El-Saadany, "Implementing virtual inertia in DFIG-based wind power generation," *IEEE Transactions on Power Systems*, to be published.

REFERENCES

[20] A. Teninge, C. Jecu, D. Roye, S. Bacha, J. Duval, and R. Belhomme, "Contribution to frequency control through wind turbine inertial energy storage," *Renewable Power Generation, IET*, vol. 3, no. 3, pp. 358–370, Sep. 2009.

[21] *IEEE Std 1561-2007 Guide for Optimizing the Performance and Life of Lead-Acid Batteries in Remote Hybrid Power Systems*, IEEE Std., 8 2008.

[22] A. Allegre, A. Bouscayrol, and R. Trigui, "Influence of control strategies on battery/supercapacitor hybrid energy storage systems for traction applications," in *IEEE Vehicle Power and Propulsion Conference, VPPC 2009*, Sep. 2009, pp. 213–220.

[23] S. Lukic, S. Wirasingha, F. Rodriguez, J. Cao, and A. Emadi, "Power management of an ultracapacitor/battery hybrid energy storage system in an HEV," in *Vehicle Power and Propulsion Conference, 2006. VPPC '06. IEEE*, Sep. 2006.

[24] C. Abbey, K. Strunz, and G. Joós, "A knowledge-based approach for control of two-level energy storage for wind energy systems," *IEEE Transactions on Energy Conversion*, vol. 24, no. 2, pp. 539–547, Jun. 2009.

[25] H. Zhou, T. Bhattacharya, D. Tran, T. Siew, and A. Khambadkone, "Composite energy storage system involving battery and ultracapacitor with dynamic energy management in microgrid applications," *IEEE Transactions on Power Electronics*, vol. 26, no. 3, pp. 923–930, Mar. 2011.

[26] J. Zheng, T. Jow, and M. Ding, "Hybrid power sources for pulsed current applications," *IEEE Transactions on Aerospace and Electronic Systems*, vol. 37, no. 1, pp. 288–292, Jan. 2001.

[27] P. Thounthong, S. Rael, and B. Davat, "Analysis of supercapacitor as second source based on fuel cell power generation," *IEEE Transactions on Energy Conversion*, vol. 24, no. 1, pp. 247–255, Mar. 2009.

[28] L. Gao, R. Dougal, and S. Liu, "Power enhancement of an actively controlled battery/ultracapacitor hybrid," *IEEE Transactions on Power Electronics*, vol. 20, no. 1, pp. 236–243, Jan. 2005.

[29] Z. Guoju, T. Xisheng, and Q. Zhiping, "Research on battery supercapacitor hybrid storage and its application in microgrid," in *Power and Energy Engineering Conference (APPEEC), 2010 Asia-Pacific*, Mar. 2010.

REFERENCES

[30] H. Xie, L. Angquist, and H.-P. Nee, "Design study of a converter interface interconnecting energy storage with the dc link of a statcom," *Power Delivery, IEEE Transactions on*, vol. 26, no. 4, pp. 2676–2686, Oct. 2011.

[31] A. Leon, J. Solsona, and M. Valla, "Control strategy for hardware simplification of voltage source converter-based power applications," *Power Electronics, IET*, vol. 4, no. 1, pp. 39–50, Jan. 2011.

[32] C. Banos, M. Aten, P. Cartwright, and T. Green, "Benefits and control of STAT-COM with energy storage in wind power generation," in *AC and DC Power Transmission, 2006. ACDC 2006. The 8th IEE International Conference on*, Mar. 2006, pp. 230–235.

[33] J. R. Espinoza, "High performance on-line control of three-phase PWM current-source converters," Ph.D. dissertation, Electrical and Computer Engineering, Concordia University, 1996.

[34] S. Inoue and H. Akagi, "A bi-directional dc/dc converter for an energy storage system," in *Applied Power Electronics Conference, APEC 2007 - Twenty Second Annual IEEE*, Mar. 2007, pp. 761–767.

[35] S. Jayasinghe, D. Vilathgamuwa, and U. Madawala, "Direct integration of battery energy storage systems in distributed power generation," *IEEE Transactions on Energy Conversion*, vol. 26, no. 2, pp. 677–685, Jun. 2011.

[36] W. Li, G. Joós, and C. Abbey, "Wind power impact on system frequency deviation and an ESS based power filtering algorithm solution," in *Power Systems Conference and Exposition, 2006. PSCE '06. 2006 IEEE PES*, Oct. 2006, pp. 2077–2084.

[37] K. De Brabandere, B. Bolsens, J. Van den Keybus, A. Woyte, J. Driesen, and R. Belmans, "A voltage and frequency droop control method for parallel inverters," *IEEE Transactions on Power Electronics*, vol. 22, no. 4, pp. 1107–1115, Jul. 2007.

[38] P. C. Loh and F. Blaabjerg, "Autonomous control of distributed storages in microgrids," in *Power Electronics and ECCE Asia (ICPE ECCE), 2011 IEEE 8th International Conference on*, Jun. 2011, pp. 536–542.

REFERENCES

[39] T. Goya, E. Omine, Y. Kinjyo, T. Senjyu, A. Yona, N. Urasaki, and T. Funabashi, "Frequency control in isolated island by using parallel operated battery systems applying h_∞ control theory based on droop characteristics," *Renewable Power Generation, IET*, vol. 5, no. 2, pp. 160–166, Mar. 2011.

[40] J. Kehler, "Considerations for load as a virtual generator for grid security," in *Power Engineering Society General Meeting, 2003, IEEE*, vol. 4, Jul. 2003, pp. 2289–2292.

[41] H. P. Beck and R. Hesse, "Virtual synchronous machine," in *Electrical Power Quality and Utilisation, 2007. EPQU 2007. 9th International Conference on*, Oct. 2007.

[42] J. Driesen and K. Visscher, "Virtual synchronous generators," in *Power and Energy Society General Meeting - Conversion and Delivery of Electrical Energy in the 21st Century, 2008 IEEE*, Jul. 2008.

[43] S. De Haan, R. Van Wesenbeeck, and K. Visscher. (2008, Oct.) VSG control algorithms: present ideas. Project VSYNC.

[44] K. Visscher and S. De Haan, "Virtual synchronous machines (VSGs) for frequency stabilisation in future grids with a significant share of decentralized generation," in *SmartGrids for Distribution, 2008. IET-CIRED. CIRED Seminar*, Jun. 2008.

[45] Q. C. Zhong and G. Weiss, "Static synchronous generators for distributed generation and renewable energy," in *Power Systems Conference and Exposition, 2009. PSCE'09. IEEE/PES*, Mar. 2009.

[46] M. Van Wesenbeeck, S. de Haan, P. Varela, and K. Visscher, "Grid tied converter with virtual kinetic storage," in *PowerTech, 2009 IEEE Bucharest*, Jul. 2009.

[47] Q. C. Zhong and G. Weiss, "Synchronverters: Inverters that mimic synchronous generators," *IEEE Transactions on Industrial Electronics*, vol. 58, no. 4, pp. 1259–1267, Apr. 2011.

[48] J. Morren, S. de Haan, W. Kling, and J. Ferreira, "Wind turbines emulating inertia and supporting primary frequency control," *IEEE Transactions on Power Systems*, vol. 21, no. 1, pp. 433–434, Feb. 2006.

REFERENCES

[49] G. Delille, B. Francois, and G. Malarange, "Dynamic frequency control support by energy storage to reduce the impact of wind and solar generation on isolated power system's inertia," *Sustainable Energy, IEEE Transactions on*, vol. 3, no. 4, pp. 931–939, Oct. 2012.

[50] X. Yingcheng and T. Nengling, "Review of contribution to frequency control through variable speed wind turbine," *Renewable Energy*, vol. 36, no. 6, pp. 1671–1677, 2011.

[51] M. Torres and L. A. C. Lopes, "Virtual synchronous generator control in autonomous wind-diesel power systems," in *Electrical Power Energy Conference (EPEC), 2009 IEEE Montreal*, Oct. 2009.

[52] M. Torres and L. A. C. Lopes, "Frequency control improvement in an autonomous power system: An application of virtual synchronous machines," in *Power Electronics and ECCE Asia (ICPE ECCE), 2011 IEEE 8th International Conference on*, Jun. 2011, pp. 2188–2195.

[53] M. Torres and L. A. C. Lopes, "Inverter-based virtual diesel generator for laboratory-scale applications," in *IECON 2010 - 36th Annual Conference on IEEE Industrial Electronics Society*, Nov. 2010, pp. 532–537.

[54] M. Torres and L. A. C. Lopes, "Inverter-based diesel generator emulator for the study of frequency variations in a laboratory-scale autonomous power system," *Energy and Power Engineering*, vol. 5, no. 3, pp. 274–283, 2013.

[55] M. Torres and L. A. C. Lopes, "A virtual synchronous machine to support dynamic frequency control in a mini-grid that operates in frequency droop mode," *Energy and Power Engineering*, vol. 5, no. 3, pp. 259–265, 2013.

[56] M. Torres and L. A. C. Lopes, "An optimal virtual inertia controller to support frequency regulation in autonomous diesel power systems with high penetration of renewables," *Renewable Energy and Power Quality Journal*, 2011.

[57] M. Torres and L. A. C. Lopes, "Virtual synchronous generator: A control strategy to improve dynamic frequency control in autonomous power systems," *Energy and Power Engineering*, vol. 5, no. 2A, pp. 32–38, 2013.

[58] A. J. Wood and B. F. Wollenberg, *Power Generation, Operation and Control.* John Wiley and Sons, Inc., 1996.

[59] S. Roy, O. Malik, and G. Hope, "A low order computer model for adaptive speed control of diesel driven power-plants," in *Industry Applications Society Annual Meeting, 1991., Conference Record of the 1991 IEEE*, Sep. 1991, pp. 1636–1642.

[60] S. Roy, O. Malik, and G. Hope, "A least-squares based model-fitting identification technique for diesel prime-movers with unknown dead-time," *IEEE Transactions on Energy Conversion*, vol. 6, no. 2, pp. 251–256, Jun. 1991.

[61] S. Roy, O. Malik, and G. Hope, "An adaptive control scheme for speed control of diesel driven power-plants," *IEEE Transactions on Energy Conversion*, vol. 6, no. 4, pp. 605–611, Dec. 1991.

[62] G. Scott, V. Wilreker, and R. Shaltens, "Wind turbine generator interaction with diesel generators on an isolated power system," *IEEE Transactions on Power Apparatus and Systems*, vol. PAS-103, no. 5, pp. 933–937, May 1984.

[63] *Technical specification: The genset engine 912 series.*, Deutz AG, Dec. 1998.

[64] S. Krishnamurthy, T. Jahns, and R. Lasseter, "The operation of diesel gensets in a CERTS microgrid," in *Power and Energy Society General Meeting - Conversion and Delivery of Electrical Energy in the 21st Century, 2008 IEEE*, Jul. 2008, pp. 1–8.

[65] *Technical specification: synchornous generator for diesel/gas engine industrial application series.*, 8AMG5862124, ABB Generators Ltd., Sep. 2011.

[66] *RB and PM Hi-Tec Industrial Couplings.*, Renold plc, Apr. 2010.

[67] *IEEE Std 1110-2002 Guide for Synchronous Generator Modeling Practices and Applications in Power System Stability Analyses*, IEEE Std., Nov. 2003.

[68] *IEEE Std 421.5-2005 (Revision of IEEE Std 421.5-1992) Recommended Practice for Excitation System Models for Power System Stability Studies*, IEEE Std., 2006.

[69] R. Krishnan, *Electric Motor Drives: Modeling, Analysis, and Control.* Prentice-Hall, 2001.

REFERENCES

[70] K. J. Åström and T. Hägglund, *Advanced PID Control*. Research Triangle Park, NC 27709: ISA - The Instrumentation, Systems, and Automation Society, 2005.

[71] *SDG500 Series Smart Digital Governor*, Governors America Corp., Mar. 2010.

[72] *176 Series Integral Electrical Actuator.*, Governors America Corp., Jun. 2005.

[73] *ISO 8528-5:2005 Reciprocating internal combustion engine driven alternating current generating sets – Part 5: Generating sets*, ISO Std., Jan. 2009.

[74] H. Slater, D. Atkinson, and A. Jack, "Real-time emulation for power equipment development. II. The virtual machine," *IEE Electric Power Applications*, vol. 145, no. 3, pp. 153–158, May 1998.

[75] A. Jack, D. Atkinson, and H. Slater, "Real-time emulation for power equipment development. I. Real-time simulation," *IEE Electric Power Applications*, vol. 145, no. 2, pp. 92–97, Mar. 1998.

[76] M. Armstrong, D. Atkinson, A. Jack, and S. Turner, "Power system emulation using a real time, 145 kW, virtual power system," in *Power Electronics and Applications, 2005 European Conference on*, 2005.

[77] M. Oettmeier, R. Bartelt, C. Heising, V. Staudt, A. Steimel, S. Tietmeyer, B. Bock, and C. Doerlemann, "Machine emulator: Power-electronics based test equipment for testing high-power drive converters," in *Optimization of Electrical and Electronic Equipment (OPTIM), 2010 12th International Conference on*, May 2010, pp. 582–588.

[78] M. H. Rashid, Ed., *Power Electronics Handbook*. San Diego-California, USA: Academic Press, 2007.

[79] T. S. Lee, "Input-output linearization and zero-dynamics control of three-phase ac/dc voltage-source converters," *IEEE Transactions on Power Electronics*, vol. 18, no. 1, pp. 11–22, Jan. 2003.

[80] R. Doherty, A. Mullane, G. Nolan, D. Burke, A. Bryson, and M. O'Malley, "An assessment of the impact of wind generation on system frequency control," *IEEE Transactions on Power Systems*, vol. 25, no. 1, pp. 452–460, Feb. 2010.

REFERENCES

[81] R. Isermann, *Digital control systems*, 2nd ed.   New York: Springer-Verlag, 1989.

[82] V. Bobál, J. Böhm, J. Fessl, and J. Macháček, *Digital self-tuning controllers*. Springer-Verlag, London, 2005.

[83] J. Rodriguez, S. Bernet, B. Wu, J. Pontt, and S. Kouro, "Multilevel voltage-source-converter topologies for industrial medium-voltage drives," *IEEE Transactions on Industrial Electronics*, vol. 54, no. 6, pp. 2930 –2945, Dec. 2007.

[84] S. Kouro, P. Cortes, R. Vargas, U. Ammann, and J. Rodriguez, "Model predictive control—a simple and powerful method to control power converters," *IEEE Transactions on Industrial Electronics*, vol. 56, no. 6, pp. 1826–1838, Jun. 2009.

[85] *Automatic Voltage Regulator EA63-5 User Manual.*, 8AMG5855292, ABB Generators Ltd., ago 2010.

[86] M. Perez, J. Espinoza, L. Moran, M. Torres, and E. Araya, "A robust phase-locked loop algorithm to synchronize static-power converters with polluted ac systems," *IEEE Transactions on Industrial Electronics*, vol. 55, no. 5, pp. 2185–2192, May 2008.

[87] P. Anderson and A. Bose, "Stability simulation of wind turbine systems," *IEEE Transactions on Power Apparatus and Systems*, vol. PAS-102, no. 12, pp. 3791 –3795, Dec. 1983.

[88] Renewable energy cheaper than coal. Wind data files.

[89] T. Ackermann, Ed., *Wind Power in Power Systems*.   John Wiley & Sons, Ltd, Mar. 2005.

[90] Wind turbine E-3120 50kW, Endurance Wind Power.

APPENDIX A

DIESEL GENERATOR MODEL

A.1   DIESEL ENGINE AND FUEL INJECTION SYSTEM

Table A.1: Diesel engine parameters.

Description	Symbol	Value	Unit
Continuous output power[*]	P_{cp}	33	kW
Synchronous speed[*]	N_s	1500	r/min
Maximum torque[*]	τ_{max}	230	N·m
Moment of inertia[*,†]	J_{en}	1.18	kg·m^2
Frictional losses	k_{fen}	0.12	kg·m^2/s
Fuel injection time constant[‡]	t_e	35	ms
Engine delay[§]	t_d	22	ms

[*]Data from diesel engine datasheet [63].
[†]Considering flywheel (1.02 kg·m^2) and engine (0.16 kg·m^2).
[‡]Data from actuator datasheet [72].
[§]Data from a 10 kW diesel engine used in [64].

Linear model with no delay:

$$\frac{d\tau_m}{dt} = -\frac{1}{t_e}\tau_m + \frac{k_e}{t_e}u_\omega \tag{A.1}$$

A.2 COUPLING SHAFT

State-space representation:

$$\frac{d\mathbf{x}_{sh}}{dt} = \mathbf{A}_{sh}\mathbf{x}_{sh} + \mathbf{B}_{sh}\mathbf{u}_{sh} \tag{A.2a}$$

$$\mathbf{y}_{sh} = \mathbf{C}_{sh}\mathbf{x}_{sh} \tag{A.2b}$$

State vector, input vector and output vector:

$$\mathbf{x}_{sh} = \begin{bmatrix} \omega_{en} & \omega_{ge} & \tau_{ss} \end{bmatrix}^T \qquad \mathbf{u}_{sh} = \begin{bmatrix} \tau_m & \tau_e \end{bmatrix}^T \qquad \mathbf{y}_{sh} = \begin{bmatrix} \omega_{en} & \omega_{ge} \end{bmatrix}^T$$

System matrices:

$$\mathbf{A}_{sh} = \begin{bmatrix} -\frac{k_{fens}}{J_{en}} & \frac{k_{fs}}{J_{en}} & -\frac{1}{J_{en}} \\ \frac{k_{fs}}{J_{ge}} & -\frac{k_{fges}}{J_{ge}} & \frac{1}{J_{ge}} \\ k_{ss} & -k_{ss} & 0 \end{bmatrix} \quad \mathbf{B}_{sh} = \begin{bmatrix} \frac{1}{J_{en}} & 0 \\ 0 & \frac{1}{J_{ge}} \\ 0 & 0 \end{bmatrix} \quad \mathbf{C}_{sh} = \begin{bmatrix} 1 & 0 & 0 \\ 0 & 1 & 0 \end{bmatrix}$$

Transfer matrix:

$$\mathbf{H}_{sh}(s) = \mathbf{C}_{sh}(s\mathbf{I}_3 - \mathbf{A}_{sh})^{-1}\mathbf{B}_{sh} = \begin{bmatrix} h_{sh11}(s) & h_{sh12}(s) \\ h_{sh21}(s) & h_{sh22}(s) \end{bmatrix} \tag{A.3}$$

Transfer function of interest for analysis of the transient response:

$$h_{\text{sh11}}(s) = \frac{\omega_{\text{en}}(s)}{\tau_{\text{m}}(s)} = \cdots \tag{A.4}$$

$$\cdots \frac{J_{\text{ge}}s^2 + k_{\text{fges}}s + k_{\text{ss}}}{J_{\text{ge}}J_{\text{en}}s^3 + (J_{\text{ge}}k_{\text{fens}} + J_{\text{en}}k_{\text{fges}})s^2 + (k_{\text{ss}}(J_{\text{ge}} + J_{\text{en}}) + k_{\text{fens}}k_{\text{fges}} - k_{\text{fs}}^2)s + k_{\text{ss}}(k_{\text{fen}} + k_{\text{fge}})}$$

Fig. A.1 shows the position of poles and zeros of h_{sh11} in the complex plane when varying shaft parameters k_{ss} and k_{fs}. From the left plot of Fig. A.1 it is observed that as the damping of the shaft is increased—for a constant stiffness—the damping ratio of the complex poles is increased, however, their natural oscillation frequency remain constant. The latter will result in the attenuation of the resonance peak, but the resonance frequency will remain the same. On the other hand, in the right plot of Fig. A.1 it is observed that as the stiffness of the shaft is increased—for a constant damping—the complex poles and zeros are moved away in the direction of the imaginary axis, which causes the shifting of the local resonance to a higher frequency.

Table A.2: Parameters of mechanical shaft.

Description	Symbol	Value*	Unit
Torsional stiffness coefficient	k_{ss}	6×10^3	N·m
Torsional damping coefficient	k_{fs}	4.78	kg·m^2/s

*Data from flexible coupling, size 0.12, rubber grade SM60, nominal torque 250 N·m [66].
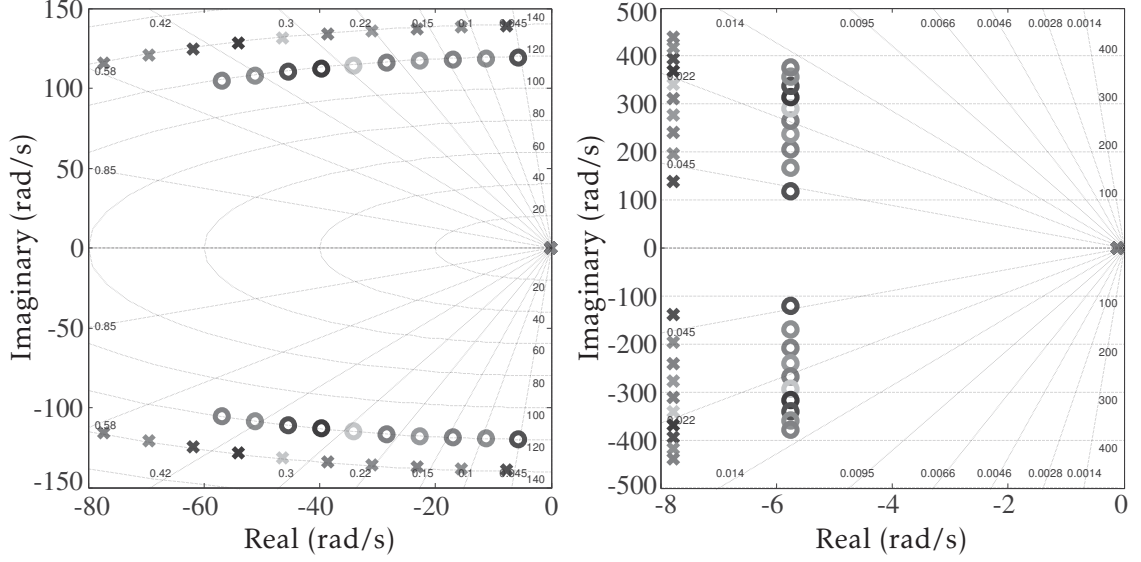
Figure A.1: Pole-Zero map of transfer function h_{sh11}.

A.3   SYNCHRONOUS GENERATOR

Relation between fluxes and currents:

$$\psi_s^d = \left(L_{sl}^d + L_m^d \right) i_s^d + L_m^d i_f + L_m^d i_k^d \tag{A.5a}$$

$$\psi_s^q = \left(L_{sl}^q + L_m^q \right) i_s^q + L_m^q i_k^q \tag{A.5b}$$

$$\psi_f = L_m^d i_s^d + \left(L_{fl} + L_m^d \right) i_f + L_m^d i_k^d \tag{A.5c}$$

$$\psi_k^d = L_m^d i_s^d + L_m^d i_f + \left(L_{kl}^d + L_m^d \right) i_k^d \tag{A.5d}$$

$$\psi_k^q = L_m^q i_s^q + \left(L_{kl}^q + L_m^q \right) i_k^q \tag{A.5e}$$

State-space linear representation of model (2.4):

$$\frac{d\mathbf{i}_{sg}}{dt} = \mathbf{A}_{sg}\mathbf{i}_{sg} + \mathbf{B}_{sg}\mathbf{u}_{sg} \tag{A.6a}$$

$$\mathbf{y}_{sg} = \mathbf{C}_{sg}\mathbf{i}_{sg} + \mathbf{D}_{sg}\mathbf{u}_{sg} \tag{A.6b}$$

State vector, input vector and output vector:

$$\mathbf{i}_{sg} = \begin{bmatrix} i_s^d & i_s^q & i_f & i_k^d & i_k^q \end{bmatrix}^T \qquad \mathbf{u}_{sg} = \begin{bmatrix} \omega_{ge} & v_f & R_l \end{bmatrix}^T \qquad \mathbf{y}_{sg} = \begin{bmatrix} \tau_e & v_t \end{bmatrix}^T$$

Linear system matrices:

$$\mathbf{A}_{sg} = \mathbf{L}_{sg}^{-1}\left(\mathbf{W}_{sg}\mathbf{L}_{sg} + \mathbf{R}_{sg}\right) \qquad \mathbf{B}_{sg} = \mathbf{L}_{sg}^{-1}\mathbf{N}_{sg}$$

$$\mathbf{C}_{sg} = \begin{bmatrix} \frac{3}{2}n_{pp}\left(\left(L_{sl}^d + L_m^d - L_{sl}^q - L_m^q\right)i_{so}^q - L_m^q i_{ko}^q\right) & \sqrt{\frac{3}{2}}R_{lo}i_{so}^d \Big/ \sqrt{i_{so}^{d\,2} + i_{so}^{q\,2}} \\ \frac{3}{2}n_{pp}\left(\left(L_{sl}^d + L_m^d - L_{sl}^q - L_m^q\right)i_{so}^d + L_m^d\left(i_{fo} + i_{ko}^d\right)\right) & \sqrt{\frac{3}{2}}R_{lo}i_{so}^q \Big/ \sqrt{i_{so}^{d\,2} + i_{so}^{q\,2}} \\ \frac{3}{2}n_{pp}L_m^d i_{so}^q & 0 \\ \frac{3}{2}n_{pp}L_m^d i_{so}^q & 0 \\ -\frac{3}{2}n_{pp}L_m^q i_{so}^d & 0 \end{bmatrix}^T$$

$$\mathbf{D}_{sg} = \begin{bmatrix} 0 & 0 & 0 \\ 0 & 0 & \sqrt{\frac{3}{2}}\sqrt{i_{so}^{d\,2} + i_{so}^{q\,2}} \end{bmatrix}$$

$$\mathbf{L}_{sg} = \begin{bmatrix} L_{sl}^d + L_m^d & 0 & L_m^d & L_m^d & 0 \\ 0 & L_{sl}^q + L_m^q & 0 & 0 & L_m^q \\ L_m^d & 0 & L_{fl} + L_m^d & L_m^d & 0 \\ L_m^d & 0 & L_m^d & L_{kl}^d + L_m^d & 0 \\ 0 & L_m^q & 0 & 0 & L_{kl}^q + L_m^q \end{bmatrix}$$

$$\mathbf{R}_{sg} = \begin{bmatrix} -(R_s + R_{lo}) & 0 & 0 & 0 & 0 \\ 0 & -(R_s + R_{lo}) & 0 & 0 & 0 \\ 0 & 0 & -R_f & 0 & 0 \\ 0 & 0 & 0 & -R_k^d & 0 \\ 0 & 0 & 0 & 0 & -R_k^q \end{bmatrix}$$

$$\mathbf{W}_{sg} = \begin{bmatrix} 0 & n_{pp}\omega_{geo} & 0 & 0 & 0 \\ -n_{pp}\omega_{geo} & 0 & 0 & 0 & 0 \\ 0 & 0 & 0 & 0 & 0 \\ 0 & 0 & 0 & 0 & 0 \\ 0 & 0 & 0 & 0 & 0 \end{bmatrix} \quad \mathbf{N}_{sg} = \begin{bmatrix} n_{pp}\psi_{so}^q & 0 & -i_{so}^d \\ -n_{pp}\psi_{so}^d & 0 & -i_{so}^q \\ 0 & 1 & 0 \\ 0 & 0 & 0 \\ 0 & 0 & 0 \end{bmatrix}$$

Table A.3: Synchronous generator parameters.

Description	Symbol	Value*	Unit
Continuous output power	S_r	38	kVA
Rated power factor	DPF_r	0.8	NA
Terminal voltage	V_t	400	V
Synchronous speed	N_s	1500	r/min
Number of poles	n_p	4	NA
Moment of inertia	J_{ge}	0.42	kg·m^2
Frictional losses	k_{fge}	0.06	kg·m^2/s

*Data from synchronous generator datasheet [65].

A.4 Automatic Voltage Regulator

Table A.4: Parameters of genset AVR.

Description	Symbol	Value	Unit
Proportional gain	k_{pv}	0.012	NA
Integral gain	k_{iv}	0.012	1/s
Rectifier gain*	k_{rec}	170	NA
Rectifier time constant†	t_{rec}	5	ms

*Data from AVR datasheet [85].
†Assuming a 50 Hz single-phase thyristor rectifier [69].

Linear model without saturation ($u_v = y_v$):

$$\frac{dz_v}{dt} = k_{iv}(v_{tref} - v_t) \tag{A.7a}$$

$$y_v = z_v + k_{pv}(v_{tref} - v_t) \tag{A.7b}$$

$$\frac{dv_f}{dt} = -\frac{1}{t_{rec}}v_f + \frac{k_{rec}}{t_{rec}}y_v \tag{A.7c}$$

A.5   Speed Governor

Table A.5: Parameters of genset speed governor.

Description	Symbol	Value	Unit
Proportional gain	$k_{p\omega}$	0.10	NA
Integral gain	$k_{i\omega}$	0.15	1/s

Linear model without saturation ($u_\omega = y_\omega$):

$$\frac{\mathrm{d}z_\omega}{\mathrm{d}t} = \frac{k_{i\omega}}{1 + k_{p\omega}k_{dr}}\left(\omega_{en\,ref} - \omega_{en} - k_{dr}z_\omega\right) \tag{A.8a}$$

$$y_\omega = \frac{1}{1 + k_{p\omega}k_{dr}}\left(z_\omega + k_{p\omega}\left(\omega_{en\,ref} - \omega_{en}\right)\right) \tag{A.8b}$$

APPENDIX B

DIESEL GENERATOR EMULATOR

B.1 GENSET LINEAR MODEL

State-space matrices:

$$
\mathbf{b}_{\mathrm{g}} =
\begin{bmatrix}
\mathbf{B}_{\mathrm{sg}}(\cdot, 3) \\
0 \\
0 \\
0 \\
0 \\
0 \\
0 \\
-k_{iv}\mathbf{D}_{\mathrm{sg}}(2, 3)
\end{bmatrix}
$$

$$
\mathbf{C}_{\mathrm{g}} =
\begin{bmatrix}
R_{\mathrm{lo}} & 0 & 0 & 0 & 0 & 0 & 0 & 0 & 0 & 0 & 0 & 0 \\
0 & R_{\mathrm{lo}} & 0 & 0 & 0 & 0 & 0 & 0 & 0 & 0 & 0 & 0 \\
0 & 0 & 0 & 0 & 0 & 0 & 1 & 0 & 0 & 0 & 0 & 0
\end{bmatrix}
$$

$$
\mathbf{d}_{\mathrm{g}} =
\begin{bmatrix}
i_{\mathrm{so}}^{\mathrm{d}} \\
i_{\mathrm{so}}^{\mathrm{q}} \\
0
\end{bmatrix}
$$

$$\mathbf{A}_g = \begin{bmatrix}
\cdot & \cdot & \cdot & \cdot & \cdot & 0 & \cdot & 0 & 0 & 0 & \cdot & 0 \\[4pt]
\cdot & \cdot & \cdot & \cdot & \cdot & 0 & \cdot & 0 & 0 & 0 & \cdot & 0 \\[4pt]
\cdot & \cdot & \mathbf{A}_{sg} & \cdot & \cdot & 0 & \mathbf{B}_{sg}(\cdot,1) & 0 & 0 & 0 & \mathbf{B}_{sg}(\cdot,2) & 0 \\[4pt]
\cdot & \cdot & \cdot & \cdot & \cdot & 0 & \cdot & 0 & 0 & 0 & \cdot & 0 \\[4pt]
\cdot & \cdot & \cdot & \cdot & \cdot & 0 & \cdot & 0 & 0 & 0 & \cdot & 0 \\[4pt]
0 & 0 & 0 & 0 & 0 & \cdot & \cdot & \cdot & \dfrac{1}{J_{en}} & 0 & 0 & 0 \\[10pt]
\cdot & \cdot & \dfrac{\mathbf{C}_{sg}(1,\cdot)}{J_{ge}} & \cdot & \cdot & \cdot & \mathbf{A}_{sh} & \cdot & 0 & 0 & 0 & 0 \\[10pt]
0 & 0 & 0 & 0 & 0 & \cdot & \cdot & \cdot & 0 & 0 & 0 & 0 \\[6pt]
0 & 0 & 0 & 0 & 0 & \dfrac{-k_e k_{p\omega}}{t_e(1+k_{p\omega}k_{dr})} & 0 & 0 & \dfrac{-1}{t_e} & \dfrac{k_e}{t_e(1+k_{p\omega}k_{dr})} & 0 & 0 \\[12pt]
0 & 0 & 0 & 0 & 0 & \dfrac{-k_{i\omega}}{1+k_{p\omega}k_{dr}} & 0 & 0 & 0 & \dfrac{-k_{i\omega}k_{dr}}{1+k_{p\omega}k_{dr}} & 0 & 0 \\[12pt]
\dfrac{-k_{rec}k_{p\omega}\mathbf{C}_{sg}(2,1)}{t_{rec}} & \dfrac{-k_{rec}k_{p\omega}\mathbf{C}_{sg}(2,2)}{t_{rec}} & 0 & 0 & 0 & 0 & 0 & 0 & 0 & 0 & \dfrac{-1}{t_{rec}} & \dfrac{-k_{rec}}{t_{rec}} \\[12pt]
-k_{iv}\mathbf{C}_{sg}(2,1) & -k_{iv}\mathbf{C}_{sg}(2,2) & 0 & 0 & 0 & 0 & 0 & 0 & 0 & 0 & 0 & 0
\end{bmatrix}$$

B.2 SETUP PARAMETERS

B.2.1 Power Circuit

The inductor is designed to limit the harmonic content of the output current for a specific operating condition. Fig. B.1 depicts the per phase equivalent circuit of the inverter output for harmonic variables. The harmonic frequencies are defined as $f_h = h f_{cn} f_i$, where h is an integer indicating the harmonic number, f_{cn} is the SPWM normalized carrier and f_i is the nominal output frequency of the inverter in Hertz. A good quality 50 Hz voltage across the capacitor is assumed, therefore the capacitor is represented as a short-circuit at the high harmonic frequencies. At a specific harmonic frequency h the inverter output voltage is v_h, which produces a current i_h.
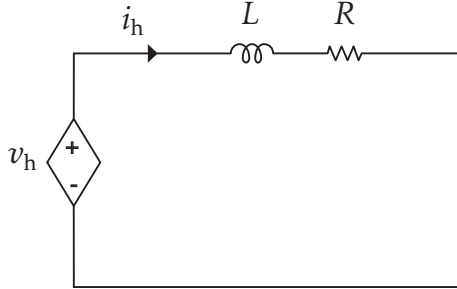
Figure B.1: Per phase equivalent circuit of the inverter output.

Fig. B.2 shows the spectrum of the output phase voltage, considering a dc bus voltage of 300 V, a commutation frequency of 5.25 kHz, and the modulation indexes as $m^d = \frac{1}{4}\sqrt{\frac{3}{2}}$ and $m^q = 0$. These values give the desired fundamental output voltage of 50 V rms.

Neglecting the resistance of the filter, the inductance is designed to limit the sum of the harmonic currents i_1, i_2 and i_3 to a 5 % of the nominal current, i_{nom}.
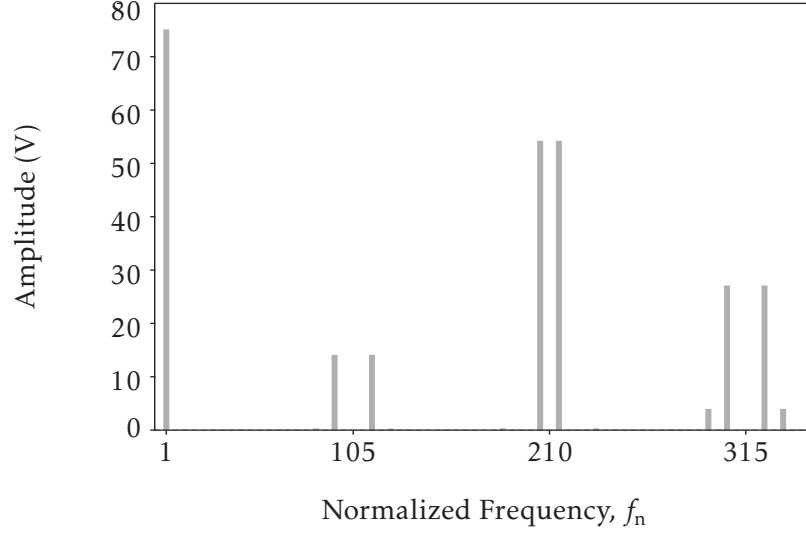
Figure B.2: Spectrum of the output phase voltage.

The expression is:

$$L \geq \frac{1}{0.05\, i_{\text{nom}}\, 2\,\pi\, f_{\text{cn}}\, f_{\text{i}}} \sqrt{\sum_{h=1}^{3} \left(\frac{v_{\text{h}}}{h}\right)^2} = \frac{10/\pi}{i_{\text{nom}}\, f_{\text{cn}}\, f_{\text{i}}} \sqrt{v_1{}^2 + \left(\frac{v_2}{2}\right)^2 + \left(\frac{v_3}{3}\right)^2} \quad \text{(B.1)}$$

Finally, for a minimum current of 0.5 A, the inductor has to be greater than 29.7 mH. An inductor of 32 mH will be used because it was the closest value available in the laboratory. A capacitor of 50 μF was used, because it was also available in the lab and it gave a good quality output voltage. The resulting resonance frequency of the filter (125.8 Hz) is sufficiently higher than the nominal output frequency of the inverter.

Table B.1: Parameters of the power circuit.

Description	Symbol	Value	Unit
ac mains nominal phase voltage	v_{gp}	120	V
ac mains nominal frequency	f_g	60	Hz
dc bus maximum voltage	v_{dc}	700	V
dc bus capacitance	C_{dc}	1100	µF
ac filter inductance	L	32	mH
ac filter resistance	R	0.2	Ω
ac filter capacitance	C	50	µF
Maximum output phase voltage rms	NA	120	V
Maximum output phase current rms	NA	5	A

Table B.2: Combinations of the resistor bank.

Step	Equivalent resistance per phase (Ω) R_{eq}	Resistors per phase (Ω) $R_1 = 250$	$R_2 = 62.5$	$R_3 = 62.5$	$R_4 = 125$
1	50	1*	0†	1	0
2	41.7	0	0	1	1
3	35.7	1	0	1	1
4	31.3	0	1	1	0
5	27.8	1	1	1	0
6	25	0	1	1	1
7	22.7	1	1	1	1

*Resistor connected.
†Resistor not connected.

B.2.2 Control System

Table B.3: Parameters of the control system.

Subsystem	Description	Symbol	Value	Unit
DSP	Analog inputs range	NA	[0,3]	V
	Control timer period	T_c	100	µs
	PWM carrier frequency	f_c	5.25	kHz
Current controller	Damping ratio	ζ	0.8	NA
	Natural frequency	ω_n	411	rad/s
	Integral gain	$k_{1i}^{d(q)}$	168750	1/s
	Proportional gain	$k_{2i}^{d(q)}$	656	NA
Voltage controller	Damping ratio	ζ	0.8	NA
	Natural frequency	ω_n	80	rad/s
	Integral gain	$k_{1v}^{d(q)}$	6400	1/s
	Proportional gain	$k_{2v}^{d(q)}$	128	NA

$$k_1 = \omega_n^2 \tag{B.2}$$

$$k_2 = 2\zeta\omega_n \tag{B.3}$$

B.3 PERFORMANCE EVALUATION

Table B.4: Errors* (%) in droop curves.

Step \ Droop	Scope readings			Channel 1		
	0 %	3 %	5 %	0 %	3 %	5 %
1	0.120	0.080	0.081	0.018	0.121	0.209
2	0.100	0.040	0.202	0.037	0.079	0.098
3	0.180	0.060	0.244	0.006	0.010	0.037
4	0.200	0.040	0.081	0.050	0.075	0.066
5	0.060	0.101	0.224	0.004	0.074	0.092
6	0.120	0.081	0.204	0.045	0.110	0.184
7	0.060	0.121	0.204	0.001	0.145	0.270

*Error calculated as $100|x - x_m|/x$, where x is the reference value and x_m the measured value.

Table B.5: Errors* (%) in the frequency nadir.

	Droop factor		
	0 %	3 %	5 %
Channel 1	0.206	0.208	0.209
Scope readings	0.103	0.104	0.209

*Error calculated as $100|x - x_m|/x$, where x is the reference value and x_m the measured value.

APPENDIX C

ROTATING REFERENCE FRAME TRANSFORMATION

The power invariant transformation is used in this thesis. With this transformation, power quantities calculated in the dq and abc reference frames are the same. The abc/dq transformation matrix is defined as:

$$\mathbf{T}_{\text{abc/dq}} = \sqrt{\frac{2}{3}} \begin{bmatrix} \sin(\omega t) & \sin(\omega t - 2\pi/3) & \sin(\omega t - 4\pi/3) \\ \cos(\omega t) & \cos(\omega t - 2\pi/3) & \cos(\omega t - 4\pi/3) \end{bmatrix} \tag{C.1}$$

where the inverse transformation dq/abc is defined as $\mathbf{T}_{\text{dq/abc}} = \mathbf{T}_{\text{abc/dq}}^{\text{T}}$.

Using the power invariant transformation, a three-phase balanced vector defined in the real axes as:

$$\mathbf{x}^{\text{abc}} = \begin{bmatrix} x^{\text{a}} \\ x^{\text{b}} \\ x^{\text{c}} \end{bmatrix} = \begin{bmatrix} a\sin(\omega t) \\ a\sin(\omega t - 2\pi/3) \\ a\sin(\omega t - 4\pi/3) \end{bmatrix} \quad , \text{with} \quad \|\mathbf{x}^{\text{abc}}\| = \sqrt{\frac{3}{2}}\,a \tag{C.2}$$

is represented in the dq rotating axes as:

$$\mathbf{x}^{\text{dq}} = \mathbf{T}_{\text{abc/dq}}\mathbf{x}^{\text{abc}} = \begin{bmatrix} x^{\text{d}} \\ x^{\text{q}} \end{bmatrix} = \sqrt{\frac{3}{2}} \begin{bmatrix} a \\ 0 \end{bmatrix} \quad , \text{with} \quad \|\mathbf{x}^{\text{dq}}\| = \sqrt{\frac{3}{2}}\,a \tag{C.3}$$

Appendix D

Virtual Synchronous Machine

D.1   Control of the Grid Side Converter

D.1.1   System Parameters

Table D.1: VSC controllers parameters.

Controller	Description	Symbol	Value	Unit
d-axis current	Integral gain	$k_{\mathrm{i}i}^{\mathrm{d}}$	202500	1/s
	Proportional gain	$k_{\mathrm{p}i}^{\mathrm{d}}$	2864	NA
q-axis current	Damping ratio	ζ	0.707	NA
	Natural frequency	ω_{n}	1000	rad/s
	Integral gain	$k_{\mathrm{i}i}^{\mathrm{q}}$	1×10^{6}	1/s
	Proportional gain	$k_{\mathrm{p}i}^{\mathrm{q}}$	1414	NA

Table D.2: VSC power circuit parameters.

Description	Symbol	Value	Unit
Grid line voltage rms	n/a	460	V
Grid frequency	f	60	Hz
dc voltage	v_{dc}	1000	V
PWM carrier frequency	n/a	5.22	kHz
Line inductor resistance	R	0.2	Ω
Line inductor inductance	L	32	mH
dc Capacitor	C	1100	μF

D.1.2   Performance Verification

Fig. D.1 shows the simulation results for a step change in the q-axis current reference. In Fig. D.1(a) can be seen that during the first grid cycle, when the reference $i_{\text{ESS ref}}^{\text{q}} = 5\,\text{A}$, the VSC is injecting reactive power to the grid ("capacitive behavior") with the ac current $i_{\text{ESS}}^{\text{a}}$ leading the grid voltage v_{g}^{a} by 90°. Conversely, during the second grid cycle, when the reference $i_{\text{ESS ref}}^{\text{q}} = -5\,\text{A}$, the VSC is absorbing reactive power from the grid ("inductive behavior") with the ac current $i_{\text{ESS}}^{\text{a}}$ lagging the grid voltage v_{g}^{a} by 90°. It is also observed that the controller achieves a good performance with the PWM model of the converter and that the reactive current is effectively regulated without disturbing the active current control loop.

Fig. D.2, Fig. D.3 and Fig. D.4 show the results for a step, ramp and quadratic change in the active current reference, respectively. In Fig. D.2(a) can be seen that during the first grid cycle, when the reference $i_{\text{ESS ref}}^{\text{d}} = 5\,\text{A}$, the VSC is injecting active power to the grid with the ac current $i_{\text{ESS}}^{\text{a}}$ in phase with the grid voltage v_{g}^{a} (phase difference of 0°). Conversely, during the second grid cycle, when the reference $i_{\text{ESS ref}}^{\text{d}} = -5\,\text{A}$, the VSC is absorbing active power from the grid with the ac current $i_{\text{ESS}}^{\text{a}}$ in counter-phase with the grid voltage v_{g}^{a} (phase difference of 180°). In Fig. D.3(a) and Fig. D.4(a), the current $i_{\text{ESS}}^{\text{a}}$ is always in phase with the grid voltage, and its amplitude is controlled by the rate of change in the reference $i_{\text{ESS ref}}^{\text{d}}$. It is observed that the controller achieves a good performance with the PWM model of the converter and that the active current follows the ramp and quadratic references without disturbing the reactive current control loop.

Figure D.1: q-axis current control for a step reference.

(a) dq model. (b) PWM model. (c) Detailed view comparing dq and PWM model.

Figure D.2: d-axis current control for a step reference.

(a) dq model. (b) PWM model. (c) Detailed view comparing dq and PWM model.

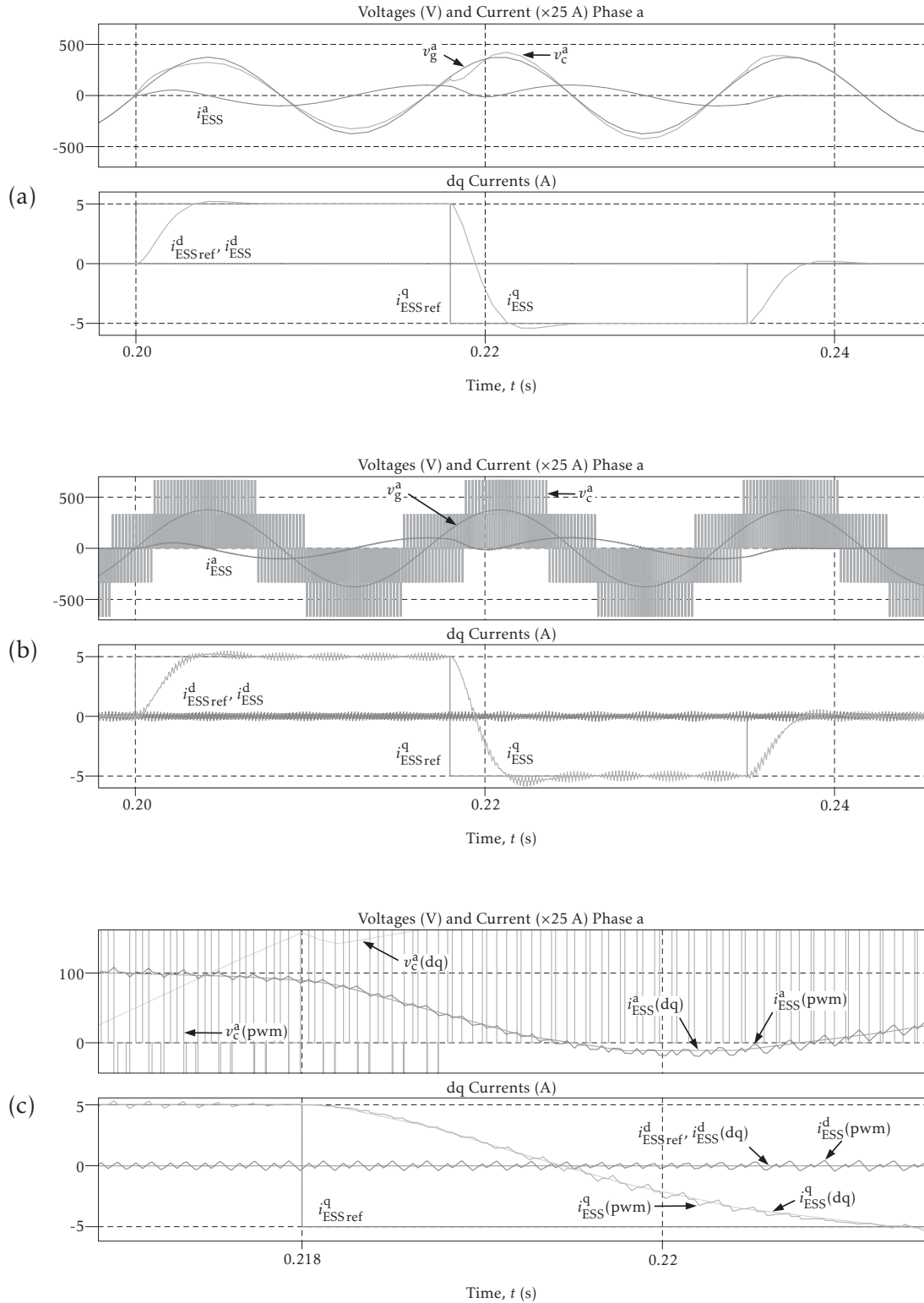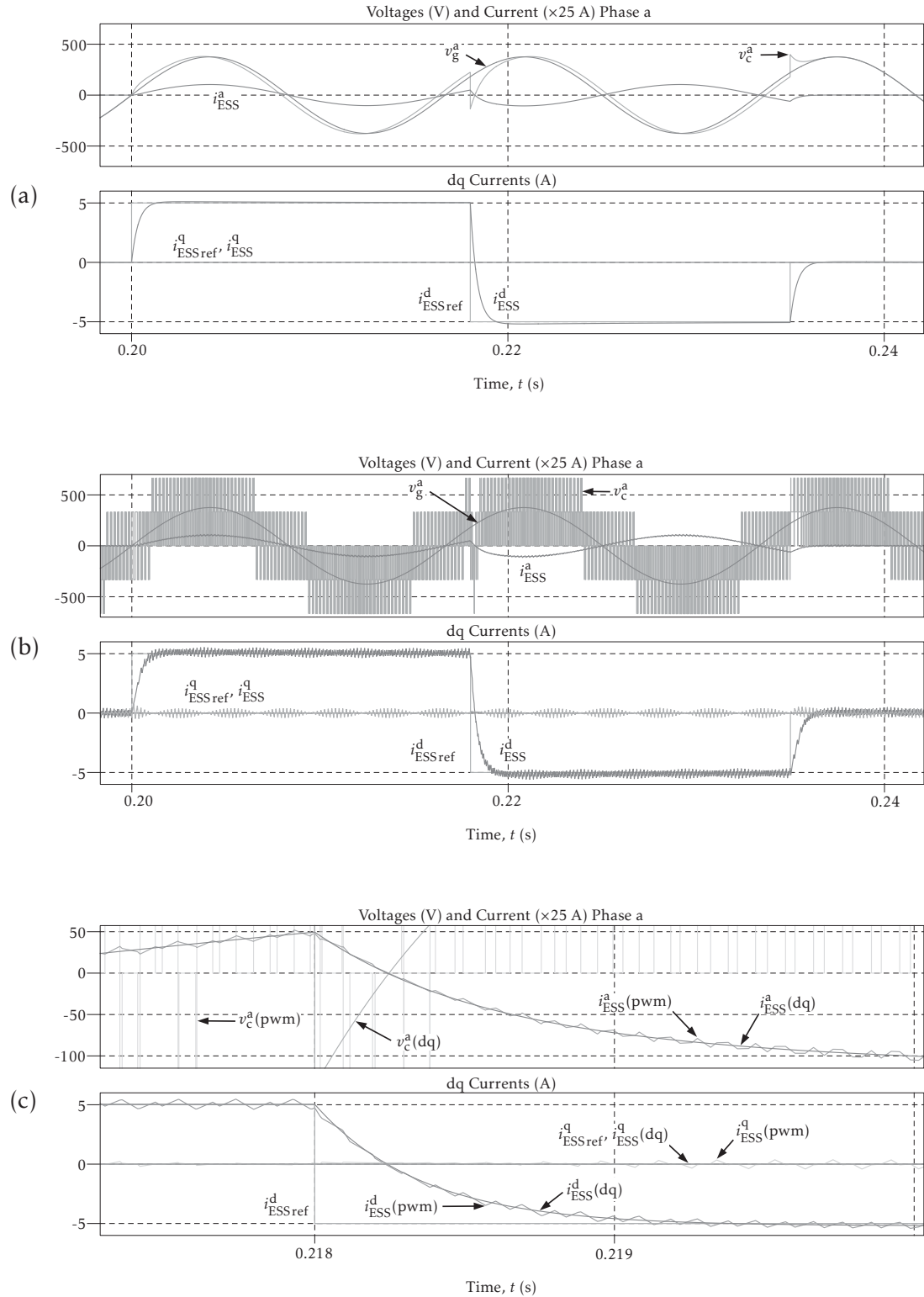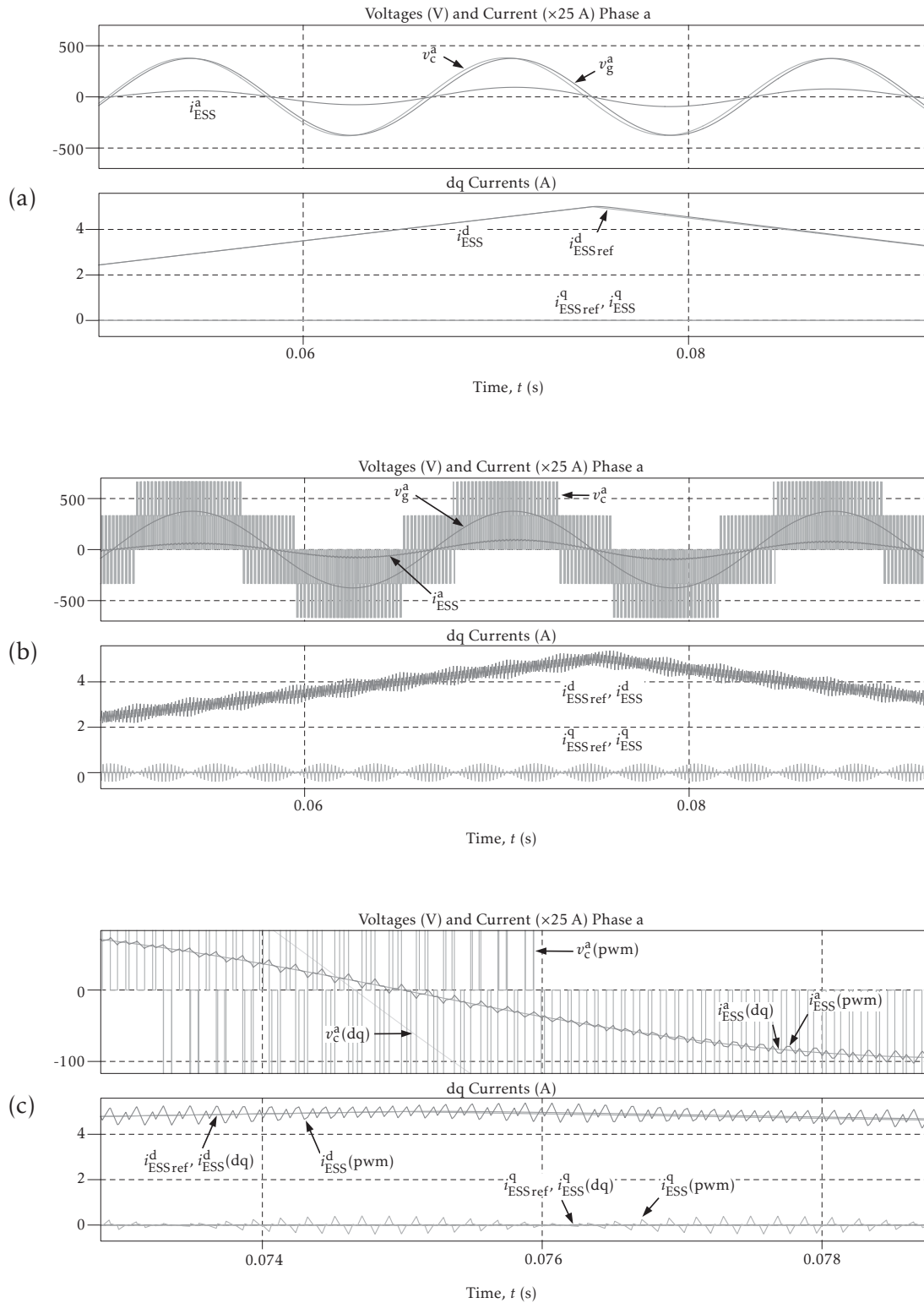**Figure D.3: d-axis current control for a ramp reference.**

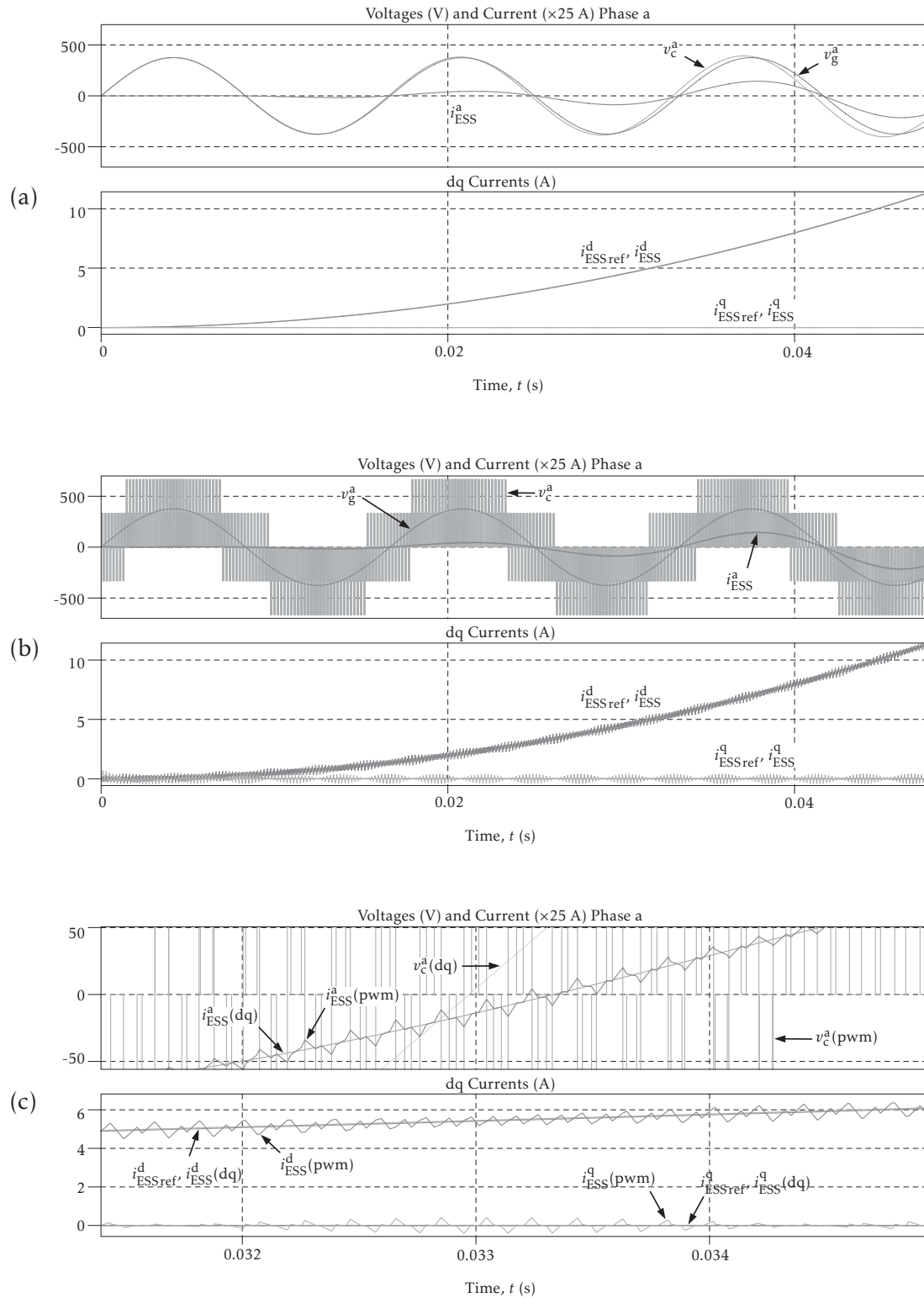(a) dq model. (b) PWM model. (c) Detailed view comparing dq and PWM model.

Figure D.4: d-axis current control for a quadratic reference.

(a) dq model. (b) PWM model. (c) Detailed view comparing dq and PWM model.

D.2 SYNCHRONIZATION OF THE VSC AND FREQUENCY MEASUREMENT

The synchronization strategy entails measuring the grid frequency and putting the transformations used for the control of the VSC ($\mathbf{T}_{abc/dq}$ and $\mathbf{T}_{dq/abc}$) in phase with the grid voltages. At the same time, the measured grid frequency is also used in the VSM control routine. Fig. D.5 shows a schematic of the synchronization system implemented in the experimental setup, which consists of an analog circuit that measures one of the grid phase voltages and generates a train of pulses whose pulse width is proportional to the positive half cycle of the sinusoidal voltage, and an interruption routine in the DSP that counts the number of sampling times between two consecutive raising edges of the train of pulses. Because the counting of sampling times is proportional to the period of the grid voltage, it is used to generate the frequency signal. At the same time, since every rising edge of the train of pulses represents the beginning of a new grid voltage cycle, they are used to keep the transformations in synchronism. These kind of digital-based synchronization strategies present characteristics such as delay due to signal processing and a limited frequency resolution due to sampling [86] that might affect the control strategy if they are not properly designed. In the following sections these two characteristics are evaluated for the proposed synchronization strategy.
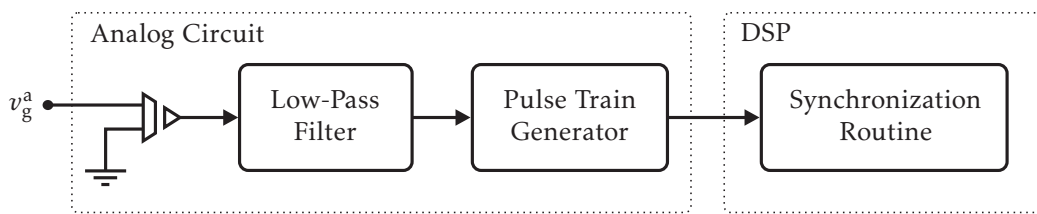
Figure D.5: Block diagram of the synchronization system.

D.2.1 Delay

There are two main sources of delay in this strategy which are depicted in Fig. D.6 (It must be mentioned that the time axis of this figure is not in scale and the time intervals have been exaggerated for the purpose of illustration). The first one, T_{d1}, is the one associated to the low-pass filtering of the measured grid voltage. The filtering is needed because a noisy measurement might generate spurious pulses near the actual zero crossing of the voltage, as shown in Fig. D.7, thus affecting the synchronization. Time delay T_{d1} affects both functions of the synchronization routine: the phase synchronization and the frequency calculation. However, since the value of T_{d1} is known (it corresponds to the time constant of the low-pass filter, $t_{lpf} = 150\,\mu s$) it can be compensated—by software—for the case of phase synchronization. The second delay shown in Fig. D.6, T_{d2}, is associated to the processing time during the interruption routine and thus it only affects the frequency calculation. This delay can be assumed (worst case scenario) as one period
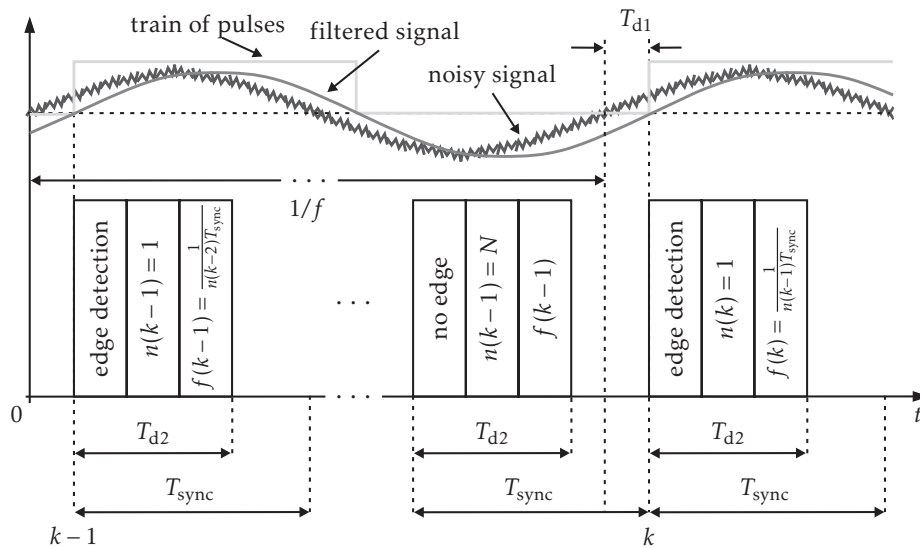
Figure D.6: Timing diagram of the synchronization routine.
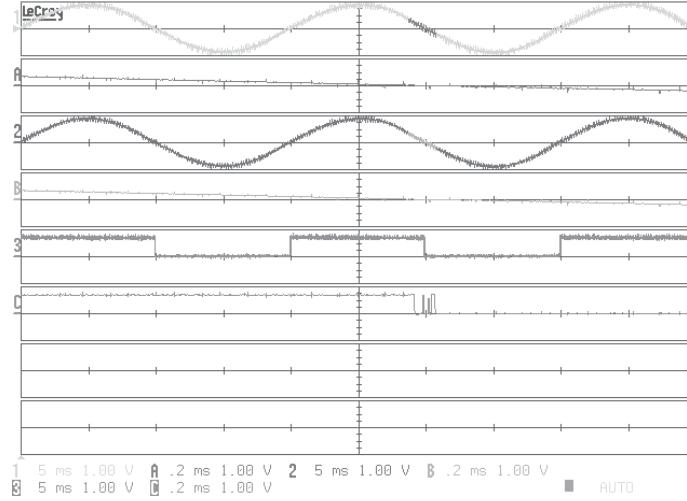
(a)
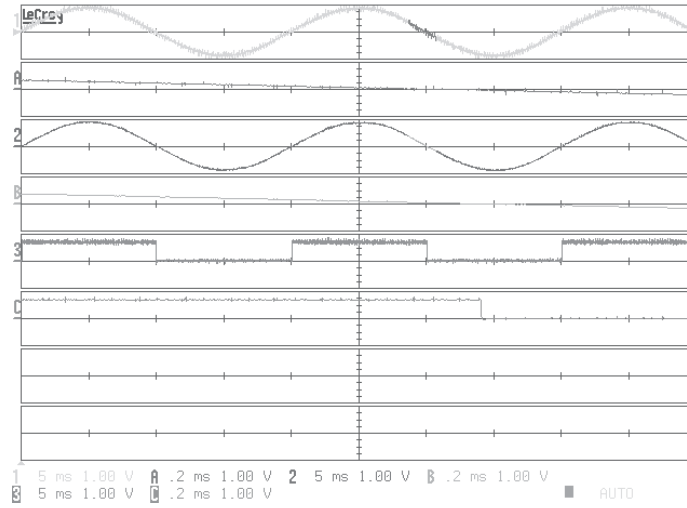
(b)

Figure D.7: Generation of the synchronization signal.

Cancelation of spurious pulse on the synchronization signal with low-pass filtering.
Ch1/A: measured grid voltage/zoom, Ch3/C: synchronization pulse/zoom. (a) Ch2/B: no
filtering/zoom. (b) Ch2/B: low-pass filtering/zoom.

of the interruption routine, T_{sync}. Therefore, the new value of the calculated grid

frequency will have a delay of $t_{\text{lpf}} + T_{\text{sync}} = 160\,\mu\text{s}$, which is almost negligible in

comparison to the fastest dynamic of the equivalent system, which is in the order

of a tenth of a second (see Fig. 3.3(b)).

D.2.2 Resolution

The resolution of the synchronization algorithm can be defined as the minimum possible increment in the calculated frequency due to a change in the period of the measured signal. Therefore, considering that the timer of the interruption routine has a fixed period, T_{sync}, then the resolution is determined only by the value of the counter, N, as follows:

$$\Delta_{\text{res}} = \frac{\pm 1}{N(N \mp 1)T_{\text{sync}}} \approx \frac{\pm 1}{N^2 T_{\text{sync}}} \quad \text{(Hz)} \tag{D.1}$$

Fig. D.8 shows the graphic of (D.1) for $T_{\text{sync}} = 10\,\mu s$. It is observed that when measuring frequencies around $50\,\text{Hz}$ ($N = 2000$) the operational resolution is close to $0.025\,\text{Hz}$. It is also observed that, since the period of the timer is fixed, the resolution increases as the measured frequency decreases.
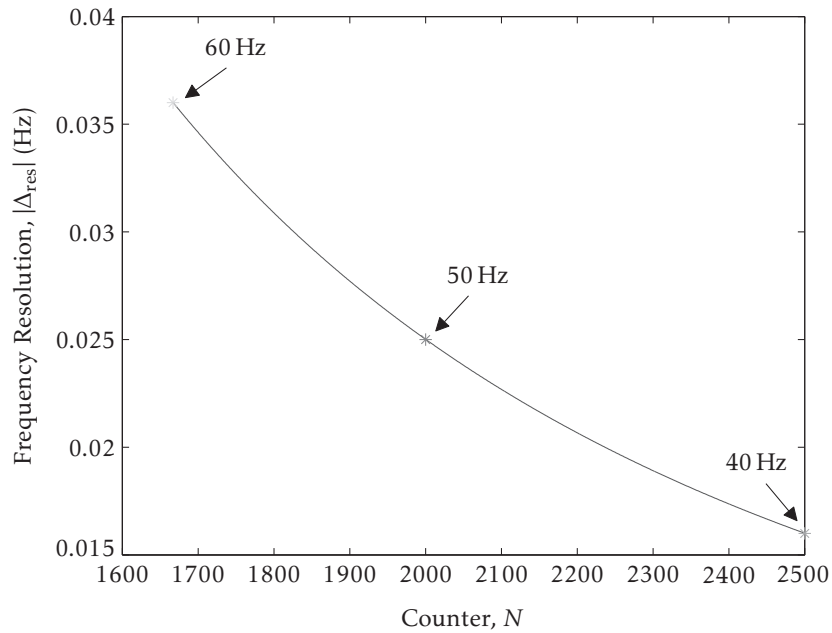
Figure D.8: Frequency resolution for $T_{\text{sync}} = 10\,\mu s$.

D.3   Experimental Setup

Discrete-time equations of the stabilization frequency estimator:

$$z_e(k+1) = (1-a_1)z_e(k) - a_2 f(k) + a_3 \tag{D.2}$$

$$\tilde{e} = \frac{-a_1 z_e(k) - a_2 f(k) + a_3}{T_{ctr}\tilde{k}_i k_r} \tag{D.3}$$

where z_e is the integrator state and a_1, a_2, a_3 are constant parameters defined as:

$$a_1 = \frac{T_{ctr}\tilde{k}_i \widetilde{m}}{1 + \widetilde{m}\tilde{k}_p} \tag{D.4}$$

$$a_2 = \frac{T_{ctr}\tilde{k}_i k_r}{1 + \widetilde{m}\tilde{k}_p} \tag{D.5}$$

$$a_3 = \frac{T_{ctr}\tilde{k}_i \widetilde{\omega}_{ref}}{1 + \widetilde{m}\tilde{k}_p} \tag{D.6}$$
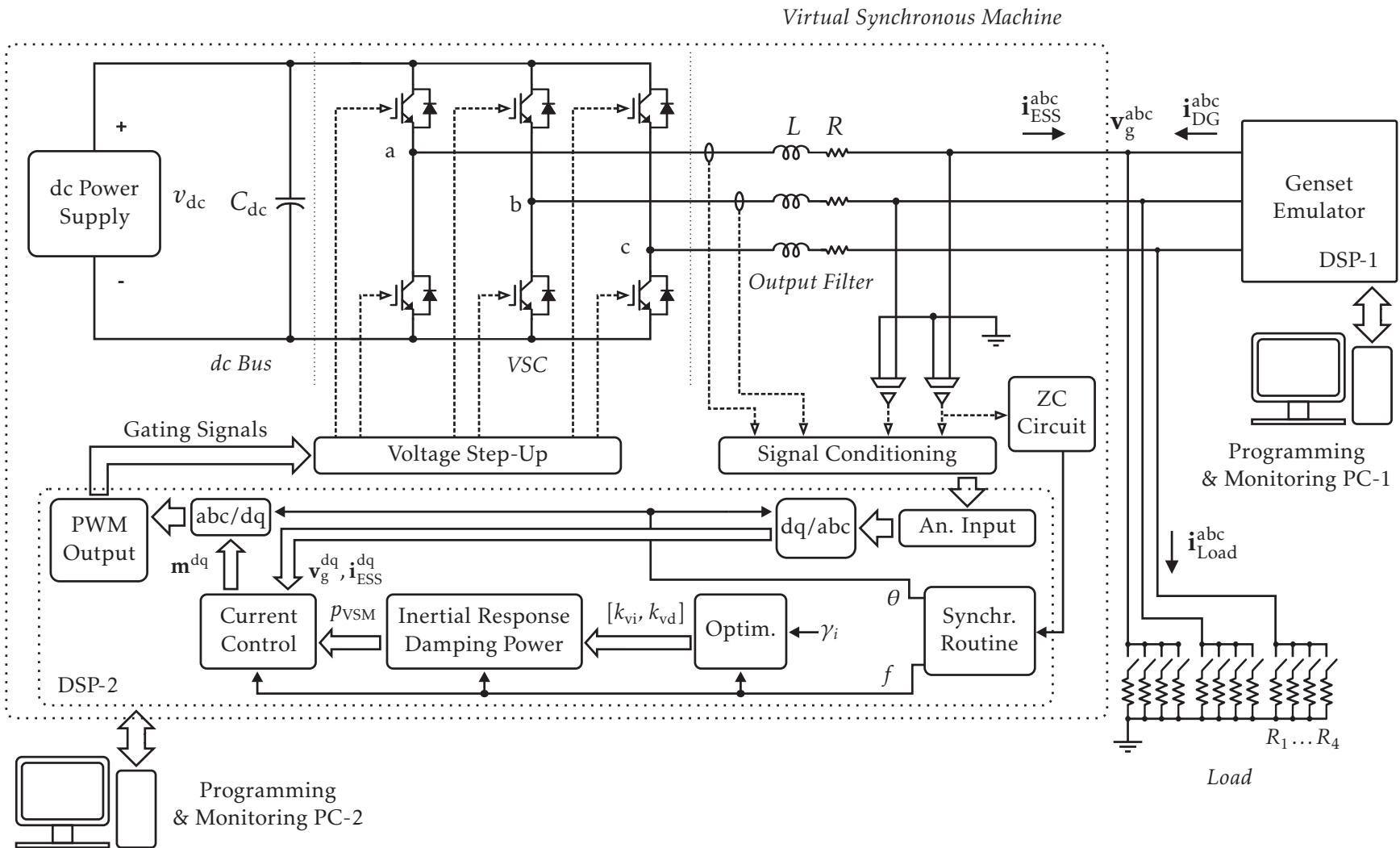
Figure D.9: Schematic of the VSM.

Appendix E

Self-Tuning Virtual Synchronous Machine

E.1 Derivation of Predictive Models

E.1.1 Model for Optimal Inertia

The model for prediction is obtained from (5.16), which is divided by k_r and then the derivative of the frequency is replaced by the first order difference equation (5.18), giving the following expression:

$$\left(J_{eq} + k_{vi}(k)\right)\frac{f(k) - f(k-1)}{T_p} = -k_{feq}f(k) + \beta(k) \tag{E.1}$$

where the new variable $\beta(k)$ represents the accelerating torque divided by k_r.

It is known in advance that the prediction models use $\beta(k+1)$, which in turn is the future value of a variable that is not being measured. Therefore $\beta(k+1)$ has to be estimated. First, $\beta(k)$ is obtained from (E.1), then assuming that $\beta(k)$ does not significantly change between two consecutive sampling times, $\beta(k+1)$ can be estimated as:

$$\tilde{\beta}(k+1) \approx \beta(k) = \left(\frac{J_{eq} + k_{vi}(k)}{T_p} + k_{feq}\right)f(k) - \frac{J_{eq} + k_{vi}(k)}{T_p}f(k-1) \tag{E.2}$$

Now, writing (E.1) for $k = k+1$ and replacing $\beta(k+1)$ by its estimated value

(E.2), the following prediction for the frequency is obtained:

$$f(k+1) = \frac{\left(J_{eq} + k_{vi}(k+1)\right)f(k) + T_p \tilde{\beta}(k+1)}{J_{eq} + k_{vi}(k+1) + T_p k_{feq}} \tag{E.3}$$

In the same way, the prediction for the rate of change of frequency is obtained as:

$$\frac{df}{dt}(k+1) = \frac{-k_{feq}f(k+1) + \tilde{\beta}(k+1)}{J_{eq} + k_{vi}(k+1)} \tag{E.4}$$

E.1.2 Model for Optimal Damping

It is assumed that the output power of the ESS, p_{ESS}, is equal to the damping power reference (5.20). Replacing the latter into (5.15), then replacing the derivative of the frequency by the first order difference equation (5.18), and dividing by k_r, the model for prediction is obtained as:

$$J_{eq}\frac{f(k) - f(k-1)}{T_p} = -k_{feq}f(k) + k_{vd}(k)\left(\tilde{f}^*(k) - f(k)\right) + \beta(k) \tag{E.5}$$

where the new variable $\beta(k)$ represents the accelerating torque divided by k_r.

It is known in advance that the prediction models use $\beta(k+1)$, which in turn is the future value of a variable that is not being measured. Therefore $\beta(k+1)$ has to be estimated. First, $\beta(k)$ is obtained from (E.5), then assuming that $\beta(k)$ does not significantly change between two consecutive sampling times, $\beta(k+1)$ can be

estimated as:

$$\tilde{\beta}(k+1) \approx \beta(k) = \left(\frac{J_{eq}}{T_p} + k_{feq} + k_{vd}(k) \right) f(k) - \frac{J_{eq}}{T_p} f(k-1) - k_{vd}(k) \tilde{f}^*(k) \qquad (\text{E.6})$$

Now, writing (E.5) for $k = k+1$ and replacing $\beta(k+1)$ by its estimated value (E.6), the following prediction for the frequency is obtained:

$$f(k+1) = \frac{J_{eq} f(k) + T_p k_{vd}(k+1) \tilde{f}^*(k) + T_p \tilde{\beta}(k+1)}{J_{eq} + T_p \left(k_{feq} + k_{vd}(k+1) \right)} \qquad (\text{E.7})$$

E.1.3 Model for Optimal Inertia and Damping

It is assumed that the output power of the ESS, p_{ESS}, is equal to the reference (6.4). Replacing the latter into (5.15), then replacing the derivative of the frequency by the first order difference equation (5.18), and dividing by k_r, the model for prediction is obtained as:

$$\left(J_{eq} + k_{vi}(k) \right) \frac{f(k) - f(k-1)}{T_p} = - \left(k_{feq} + k_{vd}(k) \right) f(k) + k_{vd}(k) \tilde{f}^*(k) + \beta(k) \qquad (\text{E.8})$$

where the new variable $\beta(k)$ represents the accelerating torque divided by k_r.

It is known in advance that the prediction models use $\beta(k + 1)$, which in turn is the future value of a variable that is not being measured. Therefore $\beta(k+1)$ has to be estimated. First, $\beta(k)$ is obtained from (E.8), then assuming that $\beta(k)$ does not significantly change between two consecutive sampling times, $\beta(k + 1)$ can be

estimated as:

$$\tilde{\beta}(k+1) \approx \beta(k) = \cdots$$

$$\cdots = \left(\frac{J_{eq} + k_{vi}(k)}{T_p} + k_{feq} + k_{vd}(k) \right) f(k) - \frac{J_{eq} + k_{vi}(k)}{T_p} f(k-1) - k_{vd}(k)\tilde{f}^*(k) \qquad (E.9)$$

Now, writing (E.8) for $k = k+1$ and replacing $\beta(k+1)$ by its estimated value (E.9), the following prediction for the frequency is obtained:

$$f(k+1) = \frac{\left(J_{eq} + k_{vi}(k+1)\right) f(k) + T_p k_{vd}(k+1)\tilde{f}^*(k) + T_p \tilde{\beta}(k+1)}{J_{eq} + k_{vi}(k+1) + T_p \left(k_{feq} + k_{vd}(k+1)\right)} \qquad (E.10)$$

In the same way, the prediction for the rate of change of frequency is obtained as:

$$\frac{df}{dt}(k+1) = \frac{-\left(k_{feq} + k_{vd}(k+1)\right) f(k+1) + k_{vd}(k+1)\tilde{f}^*(k) + \tilde{\beta}(k+1)}{J_{eq} + k_{vi}(k+1)} \qquad (E.11)$$

E.2 PERFORMANCE EVALUATION OF THE ST-VSM

Table E.1: Simulation parameters for the ST-VSM with variation of virtual inertia.

Description	Symbol	Value
Prediction sampling time	T_p	1 ms
Control sampling time	T_{ctr}	10 ms
Filtered derivative time constant	T_f	50 ms
Tolerance band (0.05 %)	ϵ	0.03 Hz
CP-VSM virtual inertia	k_{vi}	2
CP/ST-VSM damping coefficient	k_{vd}	0
ST-VSM minimum virtual inertia	K_{vi}^{min}	0
ST-VSM maximum virtual inertia	K_{vi}^{max}	2
ST-VSM search vector discretization	N_{vi}	10
Weight factors ST-VSM$_1$	γ_1	1
	γ_2	0.5
Weight factors ST-VSM$_2$	γ_1	1
	γ_2	0.2

Table E.2: Simulation parameters for the ST-VSM with variation of damping coefficient.

Description	Symbol	Value
Prediction sampling time	T_p	1 ms
Control sampling time	T_ctr	10 ms
Tolerance band (0.05 %)	ϵ	0.03 Hz
CP-VSM damping coefficient	k_vd	10
CP/ST-VSM virtual inertia	k_vi	0
ST-VSM minimum damping coefficient	$K_\mathrm{vd}^\mathrm{min}$	0
ST-VSM maximum damping coefficient	$K_\mathrm{vd}^\mathrm{max}$	10
ST-VSM search vector discretization	N_vd	20
Weight factors ST-VSM$_1$	γ_1	1
	γ_2	0.5×10^{-4}
Weight factors ST-VSM$_2$	γ_1	1
	γ_2	0.1×10^{-4}

Table E.3: Simulation parameters for the ST-VSM with variation of inertia and damping.

Description	Symbol	Value
Prediction sampling time	T_p	1 ms
Control sampling time	T_ctr	10 ms
Filtered derivative time constant	T_f	50 ms
Tolerance band (0.05 %)	ϵ	0.03 Hz
CP-VSM virtual inertia	k_vi	2
CP-VSM damping coefficient	k_vd	10
ST-VSM$_1$ search area	$\mathcal{A}$	$[0, 2] \times [0, 10]$
ST-VSM search area discretization	$N_\mathrm{vi} \times N_\mathrm{vd}$	10×20
Weight factors ST-VSM$_{1,2}$ for (6.3)	γ_1	1
	γ_2	0.5×10^{-4}
Weight factors ST-VSM$_{1,2}$ for (6.5)	γ_1	1
	γ_2	0.5
	γ_3	1
	γ_4	0.02

APPENDIX F

WIND GENERATOR MODEL

F.1 INTRODUCTION

The WG used in this work is a fixed-speed fixed-pitch (FSFP) configuration, which is connected to the grid through an induction generator. Main advantages of this configuration are its simple control and reliability in comparison to topologies including power converters. However, a FSFP WG does not allow active control of the energy capture and due to the stiff connection to the ac grid all of the mechanical disturbances are transmitted to the electrical system [15]. A block diagram of the model is shown in Fig. F.1.

F.2 WIND SPEED

The wind speed model (F.1) was obtained from [87], and it can "properly simulate the spatial effect of wind behavior, including gusting, rapid ramp changes, and background noise". The model consists in four components:

$$v_\mathrm{w} = v_\mathrm{wb} + v_\mathrm{wr} + v_\mathrm{wg} + v_\mathrm{wt} \tag{F.1}$$
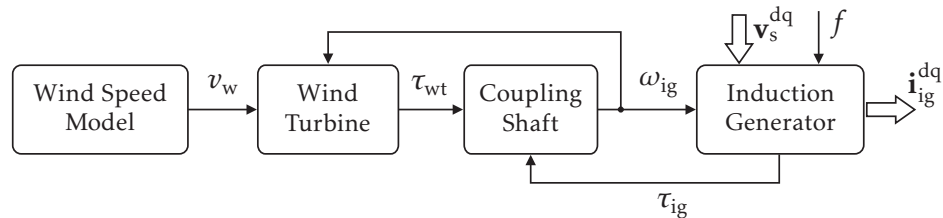
Figure F.1: Wind generator model.

where, v_{wb} is the base wind component, v_{wr} the ramp component, v_{wg} the gust component, and v_{wt} the turbulence component.

F.2.1   Ramp Component

$$v_{\mathrm{wr}}(t) = \begin{cases} \dfrac{V_{\mathrm{wr}}}{t_{\mathrm{r2}} - t_{\mathrm{r1}}} & , t_{\mathrm{r1}} \leq t \leq t_{\mathrm{r2}} \\[2ex] 0 & , \text{otherwise} \end{cases} \tag{F.2}$$

F.2.2   Gust Component

$$v_{\mathrm{wg}}(t) = \begin{cases} \dfrac{V_{\mathrm{wg}}}{2}(1 - \cos\varphi) & , t_{\mathrm{g1}} \leq t \leq t_{\mathrm{g2}} \\[2ex] 0 & , \text{otherwise} \end{cases} \tag{F.3}$$

where $\varphi = 2\pi(t - t_{\mathrm{g1}})/(t_{\mathrm{g2}} - t_{\mathrm{g1}})$.

F.2.3   Turbulence Component

The turbulence component is defined in terms of its power spectral density (PSD):

$$v_{\mathrm{wt}} = 2 \sum_{k=1}^{N} (S(\omega(k))\delta\omega)^{1/2} \cos(\omega(k)t + \phi(k)) \tag{F.4}$$

Table F.1: Parameters of the wind speed model.

Parameter description	Symbol	Value	Unit
Base wind speed	v_{wb}	4	m/s
Ramp amplitude	V_{wr}	1	m/s
Ramp start time	t_{r1}	0	s
Ramp end time	t_{r2}	3	s
Gust amplitude	V_{wg}	-2	m/s
Gust start time	t_{g1}	6	s
Gust end time	t_{g2}	7	s
PSD number of components	N	20	NA
PSD frequency step	$\delta\omega$	2	rad/s
Landscape roughness coefficient	z_0	0.0005	NA
Turbulence length scale	F	600	m

where $\omega(k) = (k - 0.5)\delta\omega$ and $\phi(k) = \text{rand}(0, 2\pi)$ are the frequency and phase of the kth cosinusoidal component, and $S(\omega(k))$ is the spectral density function defined as:

$$S(\omega(k)) = \frac{2z_0 F^2 |\omega(k)|}{\pi^2 \left(1 + \left(\frac{F\omega(k)}{\pi v_{wb}}\right)^2\right)^{4/3}} \tag{F.5}$$

F.3 WIND TURBINE

The model of the wind turbine consists of two elements: a first order system (F.6), which represents the low-pass filtering effect of the blades [89], and
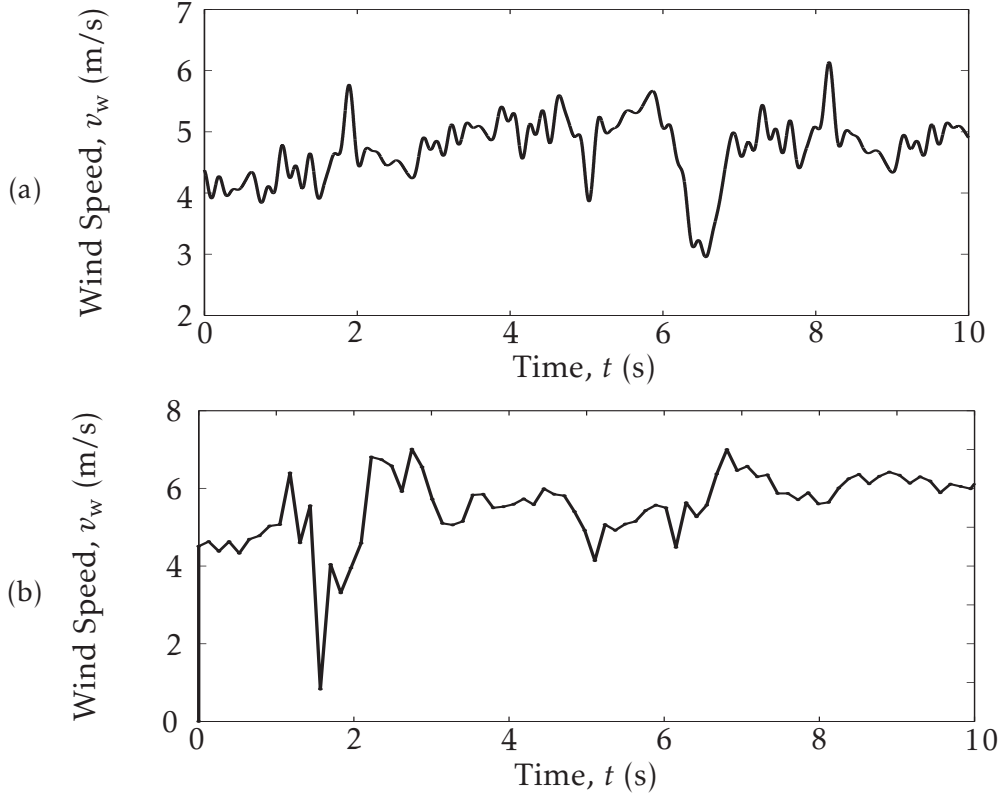
Figure F.2: Wind speed profile.

(a) Simulated wind speed profile with model (F.1) and parameters of Table F.1.
(b) Wind measurements obtained from [88].

the output power equation of the wind turbine (F.7).

$$t_{wt} \frac{dv_{wf}}{dt} = -v_{wf} + v_w \qquad (F.6)$$

$$p_{wt} = \frac{1}{2}\eta_{wt}\rho\pi R_{wt}^2 c_p(\lambda)v_{wf}^3 \qquad (F.7)$$

where, t_{wt} is a time constant related to the size of the wind turbine, v_{wf} is the filtered wind speed, ρ is the air density, R_{wt} is the radius of the turbine rotor, η_{wt} is the overall efficiency of the wind turbine, and $c_p(\lambda)$ is the performance coefficient
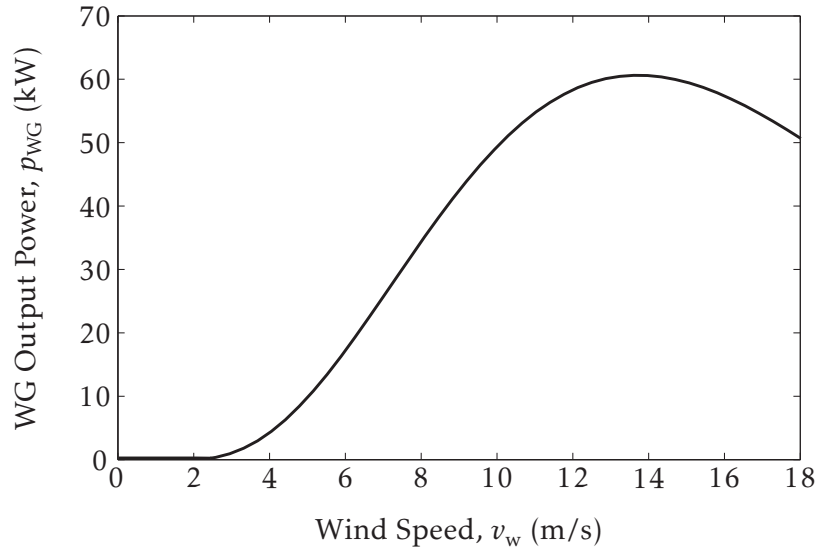
Figure F.3: Power curve of a FSFP wind turbine.

of the turbine given by:

$$c_{\mathrm{p}}(\lambda) = c_1\left(c_2\left(\frac{1}{\lambda} - c_5\right) - c_3\right)e^{-c_4\left(\frac{1}{\lambda} - c_5\right)} \tag{F.8}$$

with λ being the tip speed ratio defined as:

$$\lambda = \frac{R_{\mathrm{wt}}\omega_{\mathrm{wt}}}{v_{\mathrm{wf}}} \tag{F.9}$$

where ω_{wt} is the rotational speed of the WT. Parameters $c_{1..5}$ are defined to fit the

characteristic curve of the turbine of interest (Table F.3).

F.4   COUPLING SHAFT

The coupling shaft is represented by two rotational masses coupled by a

flexible shaft and with a gearbox to match the low rotational speed of the wind

turbine with the high speed of the induction generator. The equations are:

$$J'_{wt}\frac{d\omega'_{wt}}{dt} = -k_{fwts}\omega'_{wt} + k_{fs}\omega_{ig} - \tau_{swg} + \tau'_{wt} \tag{F.10a}$$

$$J_{ig}\frac{d\omega_{ig}}{dt} = k_{fs}\omega'_{wt} - k_{figs}\omega_{ig} + \tau_{swg} - \tau_{ig} \tag{F.10b}$$

$$\frac{d\tau_{swg}}{dt} = k_{ss}\omega'_{wt} - k_{ss}\omega_{ig} \tag{F.10c}$$

where the state variables are ω'_{wt} the rotational speed of the wind turbine, ω_{ig} rotational speed of the induction generator, and τ_{swg} the torque transmitted through the shaft. The inputs are τ'_{wt} the mechanical torque supplied by the wind turbine, and τ_{ig} the electromagnetic torque due to electric load. The parameters are J'_{wt} and k'_{fwt}, the moment of inertia and the frictional losses coefficient of the wind turbine, J_{ig} and k_{fig}, the moment of inertia and the frictional losses coefficient of the induction generator, k_{fs} and k_{ss} the damping and torsional stiffness coefficients of the shaft, with $k_{fwts} = k'_{fwt} + k_{fs}$ and $k_{figs} = k_{fig} + k_{fs}$.

In the above descriptions and model (F.10), the superscript "′" indicates that the variables and parameters of the wind turbine (low-speed side) are referred to the high-speed side of the mechanical shaft as follows:

$$\omega'_{wt} = \omega_{wt}N_{gb} \qquad \tau'_{wt} = \frac{\tau_{wt}}{N_{gb}} \qquad J'_{wt} = \frac{J_{wt}}{N^2_{gb}} \qquad k'_{fwt} = \frac{k_{fwt}}{N^2_{gb}}$$

where N_{gb} is the speed conversion factor of the gear box.

Table F.2: Parameters of mechanical shaft.

Description	Symbol	Value	Unit
Torsional stiffness	k_{ss}	6×10^3	N·m
Specific damping	k_{fs}	4.78	kg·m^2/s

F.5 INDUCTION GENERATOR

Non-linear model of the induction generator:

$$\frac{\mathrm{d}\psi_{\text{is}}^{\text{d}}}{\mathrm{d}t} = -R_{\text{is}}i_{\text{is}}^{\text{d}} + n_{\text{pp}}\omega_{\text{ge}}\psi_{\text{is}}^{\text{q}} + v_{\text{s}}^{\text{d}} \tag{F.11}$$

$$\frac{\mathrm{d}\psi_{\text{is}}^{\text{q}}}{\mathrm{d}t} = -R_{\text{is}}i_{\text{is}}^{\text{q}} - n_{\text{pp}}\omega_{\text{ge}}\psi_{\text{is}}^{\text{d}} + v_{\text{s}}^{\text{q}} \tag{F.12}$$

$$\frac{\mathrm{d}\psi_{\text{ir}}^{\text{d}}}{\mathrm{d}t} = -R_{\text{ir}}i_{\text{ir}}^{\text{d}} + \left(n_{\text{pp}}\omega_{\text{ge}} - n_{\text{ipp}}\omega_{\text{ig}}\right)\psi_{\text{ir}}^{\text{q}} \tag{F.13}$$

$$\frac{\mathrm{d}\psi_{\text{ir}}^{\text{q}}}{\mathrm{d}t} = -R_{\text{ir}}i_{\text{ir}}^{\text{q}} - \left(n_{\text{pp}}\omega_{\text{ge}} - n_{\text{ipp}}\omega_{\text{ig}}\right)\psi_{\text{ir}}^{\text{d}} \tag{F.14}$$

$$\tau_{\text{ig}} = k_{\tau\text{ig}}\left(i_{\text{ir}}^{\text{d}}i_{\text{is}}^{\text{q}} - i_{\text{ir}}^{\text{q}}i_{\text{is}}^{\text{d}}\right) \tag{F.15}$$

with $k_{\tau\text{ig}} = \dfrac{3}{2}n_{\text{ipp}}L_{\text{im}}$.

Relation between fluxes and currents:

$$\psi_{\text{is}}^{\text{d}} = \left(L_{\text{isl}} + L_{\text{im}}\right)i_{\text{is}}^{\text{d}} + L_{\text{im}}i_{\text{ir}}^{\text{d}} \tag{F.16}$$

$$\psi_{\text{is}}^{\text{q}} = \left(L_{\text{isl}} + L_{\text{im}}\right)i_{\text{is}}^{\text{q}} + L_{\text{im}}i_{\text{ir}}^{\text{q}} \tag{F.17}$$

$$\psi_{\text{ir}}^{\text{d}} = L_{\text{im}}i_{\text{is}}^{\text{d}} + \left(L_{\text{irl}} + L_{\text{im}}\right)i_{\text{ir}}^{\text{d}} \tag{F.18}$$

$$\psi_{ir}^{q} = L_{im} i_{is}^{q} + \left(L_{irl} + L_{im} \right) i_{ir}^{q} \tag{F.19}$$

State-space linear representation:

$$\frac{\mathrm{d}\mathbf{i}_{ig}}{\mathrm{d}t} = \mathbf{A}_{ig}\mathbf{i}_{ig} + \mathbf{B}_{ig}\mathbf{u}_{ig} \tag{F.20a}$$

$$\mathbf{y}_{ig} = \mathbf{C}_{ig}\mathbf{i}_{ig} \tag{F.20b}$$

State vector in terms of flux and current variables:

$$\boldsymbol{\psi}_{ig} = \begin{bmatrix} \psi_{is}^{d} & \psi_{is}^{q} & \psi_{ir}^{d} & \psi_{ir}^{q} \end{bmatrix}^{T} \qquad \mathbf{i}_{ig} = \begin{bmatrix} i_{is}^{d} & i_{is}^{q} & i_{ir}^{d} & i_{ir}^{q} \end{bmatrix}^{T}$$

Input vector and output vector:

$$\mathbf{u}_{ig} = \begin{bmatrix} v_{is}^{d} & v_{is}^{q} & \omega_{ge} & \omega_{ig} \end{bmatrix}^{T} \qquad \mathbf{y}_{ig} = \begin{bmatrix} i_{is}^{d} & i_{is}^{q} & \tau_{ig} \end{bmatrix}^{T}$$

Linear system matrices:

$$\mathbf{A}_{ig} = \mathbf{L}_{ig}^{-1}\left(\mathbf{W}_{ig}\mathbf{L}_{ig} + \mathbf{R}_{ig} \right) \qquad \mathbf{B}_{ig} = \mathbf{L}_{ig}^{-1}\mathbf{N}_{ig}$$

$$\mathbf{L}_{ig} = \begin{bmatrix} L_{isl} + L_{im} & 0 & L_{im} & 0 \\ 0 & L_{isl} + L_{im} & 0 & L_{im} \\ L_{im} & 0 & L_{irl} + L_{im} & 0 \\ 0 & L_{im} & 0 & L_{irl} + L_{im} \end{bmatrix}$$

$$\mathbf{W}_{ig} = \begin{bmatrix} 0 & n_{pp}\omega_{geo} & 0 & 0 \\ -n_{pp}\omega_{geo} & 0 & 0 & 0 \\ 0 & 0 & 0 & n_{pp}\omega_{geo} - n_{ipp}\omega_{igo} \\ 0 & 0 & -n_{pp}\omega_{geo} + n_{ipp}\omega_{igo} & 0 \end{bmatrix}$$

$$\mathbf{R}_{ig} = \begin{bmatrix} -R_{is} & 0 & 0 & 0 \\ 0 & -R_{is} & 0 & 0 \\ 0 & 0 & -R_{ir} & 0 \\ 0 & 0 & 0 & -R_{ir} \end{bmatrix} \qquad \mathbf{N}_{ig} = \begin{bmatrix} 1 & 0 & n_{pp}\psi_{iso}^{q} & 0 \\ 0 & 1 & 0 & -n_{pp}\psi_{iso}^{d} \\ 0 & 0 & n_{pp}\psi_{iro}^{q} & -n_{ipp}\psi_{iro}^{q} \\ 0 & 0 & -n_{pp}\psi_{iro}^{d} & n_{ipp}\psi_{iro}^{d} \end{bmatrix}$$

$$\mathbf{C}_{ig} = \begin{bmatrix} 1 & 0 & 0 & 0 \\ 0 & 1 & 0 & 0 \\ -k_{\tau ig}i_{iro}^{q} & k_{\tau ig}i_{iro}^{d} & k_{\tau ig}i_{iso}^{q} & -k_{\tau ig}i_{iso}^{d} \end{bmatrix}$$

Table F.3: Wind generator parameters.

Parameter* description	Symbol	Value	Unit
Nominal power[†]	$P_{wt\,nom}$	50	kW
Cut-in wind speed	NA	3.5	m/s
Power regulation	NA	Stall control	NA
Rotor radius	R_{wt}	9.6	m
Turbine nominal speed	Ω_{wt}	106	r/min
Gearbox ratio	N_{gb}	43	NA
Turbine moment of inertia[‡]	J'_{wt}	5.4	kg m^2
Turbine rotational losses[‡]	k'_{fwt}	0.12	kg m^2/s
IG nominal speed	Ω_{ig}	1800	r/min
IG moment of inertia	J_{ig}	0.42	kg m^2
IG rotational losses	k_{fig}	0.06	kg m^2/s
IG number of pole pairs	n_{ipp}	2	NA
IG nominal terminal voltage	NA	480	V
Wind turbine filter time constant	t_{wt}	0.1	s
	c_1	2.3	NA
	c_2	50	NA
Performance coefficient parameters	c_3	6.94	NA
	c_4	13	NA
	c_5	-0.08	NA

*Parameters obtained from wind generator Endurance E-3120 50kW [90].
[†]Reference wind speed of 9.5 m/s.
[‡]Referred to the high speed side of the shaft.